

Study of Fullerenes on Au (111) Surfaces Using STM

by

Mahroo Rokni Fard

A thesis submitted to The University of Birmingham
for the degree of Doctor of Philosophy

School of Physics and Astronomy

University of Birmingham

September 2017

UNIVERSITY OF
BIRMINGHAM

University of Birmingham Research Archive

e-theses repository

This unpublished thesis/dissertation is copyright of the author and/or third parties. The intellectual property rights of the author or third parties in respect of this work are as defined by The Copyright Designs and Patents Act 1988 or as modified by any successor legislation.

Any use made of information contained in this thesis/dissertation must be in accordance with that legislation and must be properly acknowledged. Further distribution or reproduction in any format is prohibited without the permission of the copyright holder.

Abstract

In this thesis results obtained from the analysis of $(C_{60})_m-(Au)_n$ magic number clusters and sputtering of the Au (111) surface are presented. Experimental work was performed using a variable temperature scanning tunnelling microscope (VT-STM).

Formation of C_{60} - Au magic clusters was previously reported. Here a more in depth study of the clusters as well as conditions required to control those on Au (111) surface are explained. Results obtained show the successful production of samples with more than 50 % coverage of $(C_{60})_7-(Au)_{19}$ clusters at 280 K. Another parameter examined was the replacement of C_{60} molecules with rugby ball shaped C_{70} . Due to preference of molecules to land with their long axis perpendicular to the surface, $(C_{70})_m-(Au)_n$ magic number clusters were found.

After size distribution, the position of clusters on the surface was investigated. It is already known that annealing the structures up to 350 K results in movement of clusters to pinched elbows, where the fcc area is larger. Results presented here show the successfully movement of all Au islands from pinched to bulged elbows by annealing the sample to 180 K. This can help in positioning clusters on required elbow sites. Repeating deposition and annealing steps increases the size of Au islands on bulged elbows while islands on pinched elbow sites remain small after final deposition. This can also be helpful in controlling the size distribution of clusters on each elbow type.

Finally, topographical changes after sputtering Au (111) surface, with and without C_{60} islands have been studied. This was done using an Ar ion beam in the energy range of 700 eV to 1200 eV. The area of vacancy islands formed on a clean Au surface showed linear dependence on the energy with the sputtering yield of about 4 Au atoms per ion, in agreement with previous published values. On a sample covered with C_{60} islands, after sputtering it with 1000 eV ion beam, a wide range of molecular fragments were obtained. Subsequent annealing of this sample resulted in the recovery of Au terraces, while no major changes in the arrangement of C_{60} molecules was observed. This is an indication of the stronger binding between broken cages or with the Au surface.

To My Parents and My Younger sister

Acknowledgements

Doing PhD was a great and challenging experience for me. During this time I have received a lot of help and encouragement. I would like to take this opportunity to thank those who helped me in many ways.

First and foremost, I would like to express my special appreciation and thanks to my supervisor Dr. Quanmin Guo for his infinite patience, support and encouragement whom I have learned a lot from. Without his guidance and constant feedback I would not have finished this work.

I also like to thank Dr Yangchun Xie, who taught me how to operate the STM and do experiments, and Dr Shane Murphy, Megan Grose, Patrick Harrison and Dawn Wells for reading my thesis. Also many thanks to Rihan Wu for her valuable suggestions regarding matlab coding and all NPRL members for their friendship.

My final words go to my beloved family; I would like to thank them because of their endless love and support from hundred- thousand miles away for me. My parents, Hamidreza Rokni Fard and Sima Oliaei, believed and encouraged me during this time and my sister Mahrokh Rokni Fard who cheered me up. Words cannot express how grateful I am to them.

List of Publications

Y. C. Xie, **M. Rokni Fard**, D. Kaya, D. Bao, R. E. Palmer, S. Du, and Q. Guo. Site-Specific Assembly of Fullerene Nanorings Guided by Two-Dimensional Gold Clusters. The Journal of Physical Chemistry C, 120(20):10975-10981, 2016.

J. Gao, J. Gao, C. Yan, **M. Rokni Fard**, D. Kaya, G. Zhu, and Q. Guo. Growth of Two-Dimensional C_{60} Nanoclusters within a Propylthiolate Matrix. The Journal of Physical Chemistry C, 120(44):25481-25488, 2016.

M. Rokni Fard, and Q. Guo. Site-selective growth of nanoscale Au islands on Au (111). In preparation.

M. Rokni Fard, and Q. Guo. Manipulation of $(C_{60})_m$ - $(Au)_n$ magic clusters. In preparation.

Contents

Abstract	i
Acknowledgements	iv
List of Publications	v
Abbreviations	ix
1 Introduction	1
2 Literature Review	6
2.1 Molecular Self-Assembly	6
2.2 The Au (111) Surface	13
2.2.1 Steps on Au (111) Surface	20
2.3 Metal on Au (111)	24
2.4 Fullerene	28
2.4.1 C_{60} Molecule	28
2.4.2 C_{70} Molecule	32
2.4.3 Fullerene on Metal Surfaces	34
2.4.3.1 C_{60} on Au (111)	34
2.4.3.2 C_{60} on Cu (111)	40
2.4.3.3 C_{60} on Ag (111)	42
2.4.3.4 C_{70} on metal surfaces	44
2.5 Formation of C_{60} - Au Clusters	47
2.5.1 Producing Magic Clusters	47
2.5.2 Magic Clusters at Room Temperature	49
2.6 Sputtering	53
2.6.1 Sputtering Yield	55
3 Experimental Procedure	58
3.1 Scanning Tunnelling Microscope	58

3.2	Ultra High Vacuum	62
3.2.1	Variable Temperature STM	64
3.3	Tip Etching	67
3.4	C_{60}/C_{70} and Au Deposition	69
3.5	Sample Preparation	71
4	Size-Control of Magic Clusters	73
4.1	Introduction	73
4.2	Au Coverage Dependence of Cluster Size	74
4.3	Temperature Dependence of Cluster Size	78
4.4	Fullerene Dependence of Cluster Size	83
4.4.1	Formation of Clusters with C_{60} Molecules	83
4.4.2	Formation of Clusters with C_{70} Molecules	86
4.4.3	Joined Clusters	88
4.4.4	Ring Structures	92
4.5	Co-Deposition of Au and Fullerene Molecules	96
4.6	Summary	98
5	Manipulating Magic Clusters	100
5.1	Introduction	100
5.2	Controlling the Position of Clusters	100
5.2.1	Position of Clusters at Room Temperature	100
5.2.2	Effect of Temperature on Au Islands	102
5.2.3	Formation of Clusters on Bulged Elbow	107
5.3	Addition of Au Atoms to Stable Structures at LT	109
5.4	Addition of C_{60} Molecules to Stable Structures at LT	116
5.5	Summary	118
6	Sputtering of C_{60}/Au surface	120
6.1	Introduction	120
6.2	Sputtering of Au Surface	120
6.2.1	Sputtering Yield Calculation	125
6.3	Sputtering of C_{60} on Au	127
6.3.1	Annealing Sample	130
6.3.2	Structure of Fullerene Islands	133
6.4	Summary	135
7	Conclusion	137
A	Matlab Code For The Error on Islands Area	142
B	Matlab Code For Sputtering Yield	145

Abbreviations

DFT	D ensity - F unctional T heory
DL	D iscommensuration L ine
FCC	F ace - C entered C ubic
FWHM	F ull W idth at H alf M aximum
HCP	H exagonal C lose P ack
HOPG	H ighly O riented P yrolytic G raphite
HREELS	H igh R esolution E lectron E nergy L oss S pectroscopy
HRHAD	H igh R esolution H elium A tom D iffraction
LDOS	L ocal D ensity O f S tates
LEED	L ow E nergy E lectron D iffraction
LEIS	L ow E nergy I on S cattering
LT	L ow T emperature
NN	N earest N eighbor (distance)
NMR	N uclear M agnetic R esonance
PPM	P ull- P ush M otion (drive)
RL	R econstruction L ine
RT	R oom T emperature
SC	S imple C ubic (structure)
STM	S canning T unneling M icroscopy
STS	S canning T unneling S pectroscopy
TEAS	T hermal E nergy A tom S cattering

TEM	T ransmission E lectron M icroscopy
TP	T urbo P ump
TSP	T itanium S ublimation P ump
vdW	v an- d er- W aals
XPS	X -ray P hotoemission S pectroscopy

Chapter 1

Introduction

Thanks to the improvement and development of scientific tools with atomic-precision, there is more demand and focus on designing nano-scale systems. However, moving individual atoms and molecules can be challenging and it is not ideal for mass productions. One of the promising methods for manufacturing of such structures is self-assembly. Self-assembly can be defined as the ability to arrange molecules or atoms into a spatial configuration without any external intervention [1–3]. This method was first recognised about half a century ago with the main aim of achieving certain dimensions and forms at nano scales. Since then our understanding about forces involved in the control of assembled structures has advanced a lot. We are now able to use this technique and create different structures from one-dimensional wires [4] up to more complex systems such as porous networks that can host other molecules [5]. In order to control the position of self-assembled structures, templates are commonly used. This can be a pre-patterned surface (using methods like sputtering [6]) or a natural surface with a periodic pattern.

Sputtering of surfaces at different angles has shown interesting changes in their

morphology. A wide range of patterns from periodic ripple structures under normal angles, up to hexagonally ordered structures at normal incident angles were reported. This control over surface structure has made sputtering a well-known technique in creating templates [7–9]. Part of result chapters looks into the effect of sputtering on the Au (111) surface which is known to be a natural template.

Au is the only fcc metal with a (111) surface reconstruction, this means that the position of atoms on the surface is different from the bulk structure. The long range zigzag pattern observed on this surface has a unit cell of $22 \times \sqrt{3}$ formed of alternating fcc and hcp areas. These sites are separated by atoms in transition regions, known as the discommensuration lines (DLs) [10, 11]. One of the techniques used to image this surface is scanning tunnelling microscopy (STM).

STM is one of the well-known methods used for precise studies of surfaces under different conditions. This includes ultra-high vacuum (UHV) for clean environments up to solid liquid interfaces [12]. Images obtained from Au (111) with this technique, confirmed the coexistence of fcc and hcp areas as well as the reconstruction pattern [10, 13]. Since then, many studies focused on the self-assembly and interaction of different atoms/molecules on this surface. Results obtained have shown that the surface structure can change depending on the electro negativity of the adsorbent. If the atoms or molecules deposited are more electropositive than Au, charge flows from the adsorbent to the surface. This results in further compression in surface atoms [14]. For more electronegative atoms/molecules, charge is transferred from surface to the adsorbent that helps in relieving surface stress and lifting of the reconstruction pattern. An example of such an electronegative molecule is C_{60} [15].

C_{60} is a three dimensional molecule that has gained a lot of attention over the past few decades. Due to the interesting properties of this molecule, it has been used as a building block for many nanostructured systems [16–19]. In order to create a new device, a good understanding of the interference between the molecule and surface

is essential. The interaction and assembly of fullerene molecules, and especially C_{60} molecules, on different surfaces including Au (111) have been extensively studied [20–23]. Results have demonstrated that, due to high mobility of molecules on the Au surfaces at room temperature, islands start to grow from step edges. For nucleation on the terraces, temperature should suppress the molecular diffusion. One of the structures reported from deposition of Au atoms and C_{60} molecules at low temperatures is the $(C_{60})_m-(Au)_n$ clusters reported by our group. In this case the C_{60} and Au bonding is by electron transfer from the Au surface while molecule-molecule interaction is through van der Waals (vdW) forces. Since structures observed have a preferential C_{60}/Au ratio, they are also known as magic clusters [24].

One of the major aims and objectives of my work was to understand the interaction and structure of clusters formed in more details. To do so, different growth conditions were examined. Information obtained can help us to have more control on the ranges and positions of clusters formed. Another aim of this work was to provide a better insight into how fullerene monolayers and Au surfaces change after sputtering with low energy ions; as well as the effect of temperature on their recovery process. Such experiments can also provide a more in depth view of fullerene molecules interaction with each other as well as the Au surfaces. The layout of this thesis is as follows.

In chapter 2, a detailed review of literature involved in this work is provided. Initially self-assembly and possible forces that can be employed in production of various systems are described. C_{60} -Au clusters were then analysed with the Au (111) surface as a template. A detailed description of (111) layer of gold as well as its reconstruction pattern is provided. This involves looking at theoretical as well as experimental works performed on this surface using different techniques. Following Au (111), an introduction to the two commonly used fullerene molecules, C_{60} and C_{70} , is included. The physical and electronic structures of these two

molecules, as well as steps involved in growth of fullerene thin films and magic clusters, are clarified. The effect of sputtering C_{60} -Au surfaces was also investigated. In the final section of chapter 2, sputtering and calculations used to estimate the sputtering yields are shown.

Chapter 3 introduces the techniques used to produce and study samples during my PhD. It starts by describing STM, in particular the variable temperature (VT)-STM, and then moves on to explaining the steps required to produce Au samples. Samples were prepared by deposition of thick Au films on a highly oriented pyrolytic graphite (HOPG) surface and then cleaned in the STM chamber under vacuum conditions.

Chapters 4, 5 and 6 are experimental results. In chapter 4, the size distribution of clusters under different conditions has been examined. These conditions include variation in the Au and C_{60} coverage, as well as the scanning temperature. Finally the effects of co-depositing molecules and atoms at different temperatures, rather than using the original method of step by step deposition at low temperature, were studied.

Chapter 5 mainly focuses on the manipulation of clusters. It starts by looking at the position of structures at room temperature with respect to the reconstruction lines. Following this, attempts to control their position are presented. This includes having a majority of clusters on pinched or bulged elbows. Finally, effect of further deposition of Au and C_{60} molecules at low temperature on stable structures was investigated. It was found that, such depositions can influence the range of structures observed at room temperature.

Results presented in chapter 6 focus on the effects of sputtering the Au surface as well as an Au surface that has been partially covered by C_{60} molecules, with a low energy Ar ions. Scans of the surfaces after sputtering as well as calculation

of sputtering yield, are provided. At the end, the temperature of the sample was increased to see how it affects the Au surface and broken fullerene cages.

Finally, chapter 7 summarises all the main findings and describes possible future work that can be done in this area.

Chapter 2

Literature Review

2.1 Molecular Self-Assembly

In modern materials science, being able to provide the best and smartest solution to variety of applications in heterogeneous environments is one of the basic requirements. Ideally, functional materials should be able to address specific tasks and provide an explicit functionality. An example of this can be molecular recognition in bio-sensors. One of the main challenges in creating devices in molecular scales is positioning them precisely. Manipulating individual molecules can be time consuming, and therefore not ideal for mass production. In this case, molecular self-assembly can be a reasonable approach in creating wide range of complex structures from clusters and one-dimensional wire to more complex structures such as porous networks [12].

G. M. Whiteside et al. [3] have defined molecular self-assembly as spontaneous movement of molecules to form a well-defined, stable structure with non-covalent bindings on the surface. Stable structures formed are dependent on intermolecular bindings as well as molecules-substrates interactions. Another important factor is temperature that can influence the structure by controlling diffusivity of molecules

on the surface. It is known that by increasing the sample's temperature, kinetic energy (E_{kin}) of molecules increases too. Once enough E_{kin} is obtained, molecules can overcome the surface diffusion barrier (E_d) and move. This energy must not be higher than the binding energy (E_b) of molecules to the surface in order to avoid desorption [12].

As it was mentioned, intermolecular interaction energy (E_{inter}) is an important factor in formation of stable structures. This energy should be weak enough for the molecules to move and identify their equilibrium position, but strong enough to hold stable structures. This is possible if the E_{inter} is just slightly higher than E_{kin} . Then, these conditions for energies can be summarised as $E_b > E_{inter} \geq E_{kin} > E_d$ [12].

Different types of intermolecular interactions have been identified. Some of the most common ones with their energy ranges, binding distances and characters are shown in table 2.1.

Although in the description, self-assembled structures have been defined as systems with non-covalent bindings where molecules are able to move and reach the equilibrium state; but under certain conditions, covalent bindings can also be employed. An example of this is when substrate atoms, involved in the bonding, move with deposited molecules. This is especially common on metal surfaces [26]. One of the well-studied systems of organic molecules on metal substrates, that follow this mechanism, is self-assembly of alkanethiols on Au (111) surface where a strong covalent bond is formed between sulphur and gold atoms [27]. Movement of gold-thiolate molecules produce self-assembled structures on the surface.

By considering an appropriate molecule with its bonding type, it is possible to tune the shape and symmetry of the structures formed. Bonding with selectivity and directional properties are commonly used to control the molecular aggregation and produce simple symmetric structures [28]. Hydrogen bonding is one of the

Interaction type	Energy range	Distance	Description
van-der-Waals interaction	$\approx 0.02 - 0.1$ eV	< 1 nm	Dipole interaction between positive nucleus and outer neighbouring electrons
Hydrogen bonding	$\approx 0.05 - 0.7$ eV	$\approx 1.5 - 3.5$ Å	Dipole attraction between Hydrogen and electronegative atoms
Metallic bonding	$\approx 0.5 - 2$ eV	$\approx 1.5 - 2.5$ Å	Binding formed between charged nuclei and electron sea of metals
Ionic bonding	$\approx 0.05 - 2.5$ eV	Long range	Coulomb attraction between negative and positive ions
Covalent bonding	≈ 1 eV	short range	Electron sharing between molecules to saturate the valence band

TABLE 2.1: Basic interactions used to engineer different structures on metal surfaces. Energy range and distance data obtained from [25].

interesting examples with properties that can be used to produce a wide range of structures. Figure 2.1 shows examples of structures formed.

In figure 2.1A and B, carboxyphenyl substituted porphyrins was deposited on the Au (111) surface. In this case, a 5,10,15,20- tetrakis- (3,5- di- t - butylphenyl) porphyrin, for simplicity called H2TBPP, was used. This molecule is formed of four di-t-butylphenyl (tBP) and a phyrin core base. A simplified model of it is presented at the centre of figure 2.1. For the example presented here one

(figure 2.1A) and two (figure 2.1B) tBP have been replaced with carboxyphenyl group. The hydrogen bonding between carboxyl groups can help in controlling the supermolecular structure formed on the surface. At low coverages, both molecules form different types of clusters at elbow sites. The reconstruction pattern of the Au surface (which will be explained later in this chapter) helped to prevent the aggregation of molecules due to the van-der-Waals (vdW) interactions [29].

Apart from individual clusters, it is also possible to form compact islands. By depositing 1,4-benzenedicarboxylic acid (terephthalic acid, TPA) on Au (111) surface, compact well-ordered islands form with the main intermolecular interaction being head-to-tail hydrogen bondings [30]. This is shown in figure 2.1C. Finally, hydrogen bonding can be used to produce a porous network too. N. Lin et al. [31] have reported that by deposition of tritopic trimesic-acid [1,3,5-benzenetricarboxylic acid (TMA)] molecules on Ag (111) at 120 K and slowly annealing the sample up to room temperature, it is possible to form a porous network. In this case three-fold symmetry of molecules has been employed to form a honeycomb structure, as shown in figure 2.1D.

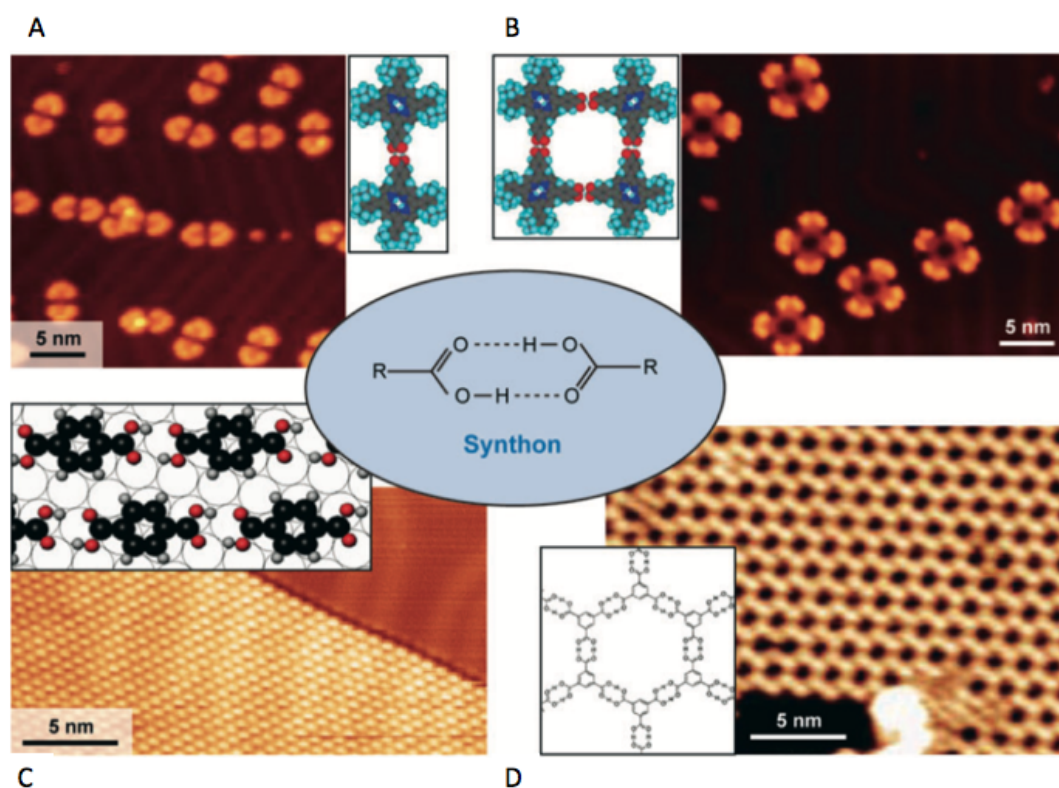


FIGURE 2.1: Different structures formed by hydrogen bonding using carboxylic acid groups as synthon. Two (A) and four (B) carboxyphenyl substituted porphyrins molecules were deposited on Au (111) surface to form different type of clusters on elbow sites. C) It is also possible to have two dimensional islands using Hydrogen bindings. In this case Terephthalic acid was deposited on Au (111). D) Formation of porous network on Ag (111) using tritopic trimesic-acid molecules at room temperature was also reported (from [25]).

Coverage can also be used to control dimensions of structures obtained. J. Weckser et al. [4], have examined self-assembly of 4-[trans-2-(pyrid-4-yl-vinyl)] benzoic acid (PVBA) on Ag (111) surface. This molecule is known to have a functional group for hydrogen bonding. From results obtained it has been reported that, at low coverages, deposition of molecules at room temperature will result in formation of chain-like structures. By increasing the coverage, structures expand to form compact two dimensional islands. Figure 2.2 shows a model for this molecule as well as the quasi-one dimensional chains and islands observed at different coverages.

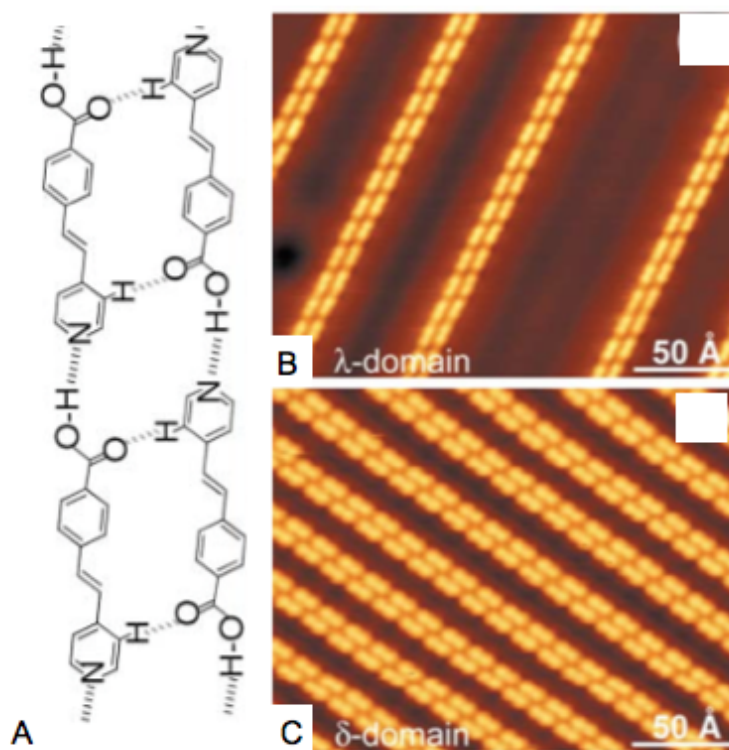


FIGURE 2.2: The 4-[trans-2-(pyrid-4-yl-vinyl)] benzoic acid (PVBA) molecule was deposited on Ag (111) surface at room temperature. A) Image A is the model used to show how molecular chains are formed by hydrogen bindings. B) An image of quasi-one dimensional chains formed at low coverages is presented. C) By increasing the coverage, two dimensional island have been observed (from [4]).

Production of more complex structures requires co-deposition of different atoms and molecules. An example of this is the porous networks produced from deposition of perylene tetra-carboxylic di-imide (PTCDI) molecules and melamine on silicon surface covered with thin silver film. Since melamine has three-fold symmetry, it will work as a connection point for PTCDI molecules through hydrogen bondings. The main point is to deposit PTCDI at room temperature and then anneal the sample to 100 °C for deposition of melamine. This would provide enough energy for PTCDI molecules to detach from islands and diffuse on the surface. Molecules will then bond to melamine and form a hexagonal network. In this example, coverage plays an important role too. If the initial amount of PTCDI

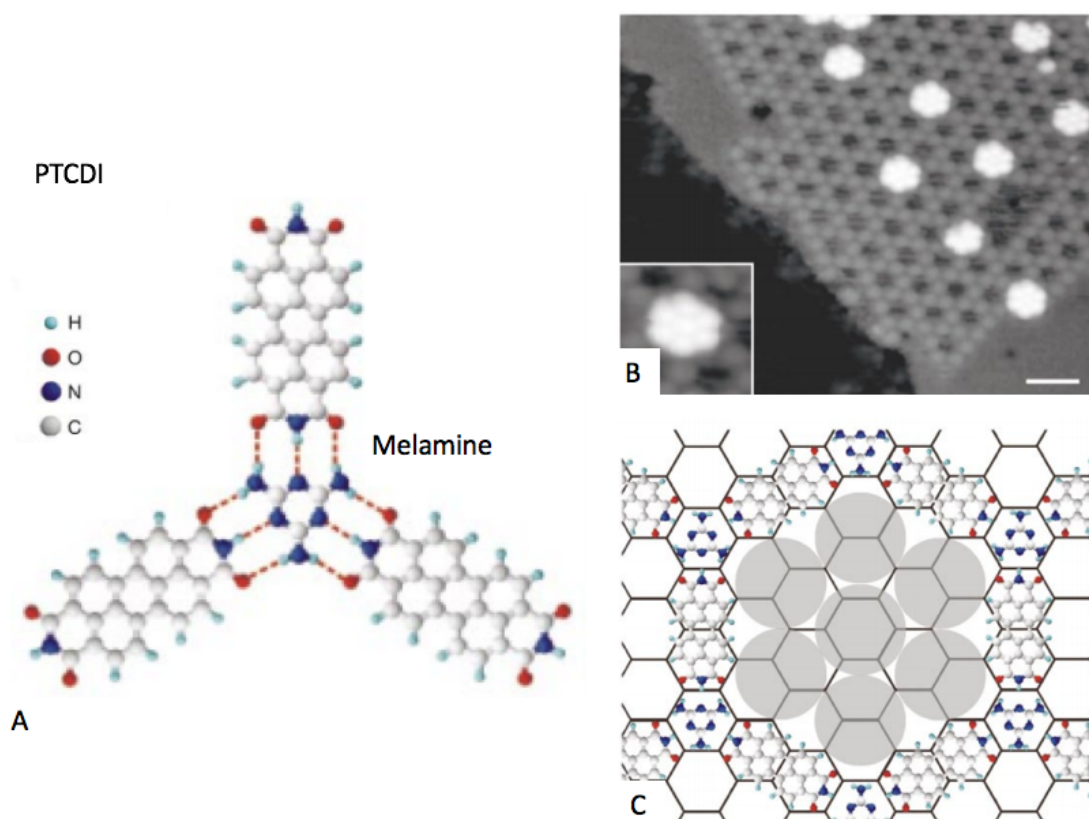


FIGURE 2.3: A) Schematic diagram of melamine-PTCDI, with hydrogen bindings being highlighted by dotted lines. PTCDI molecules are attached to each corner while melamine is located at the centre. B) Scan of the hexagonal network obtained with C_{60} molecules at the centre of porous is presented. The inset shows a high resolution image of one cluster with 7 molecules. C) Diagram used to explain the position of structures on the surface (from [5]).

molecules is too high then the porous network formed will be filled with them. Although such structures have been obtained from a single molecule deposition [32], co-adsorption can help in producing larger size pores. So that other molecules can be deposited on this network too. Figure 2.3 shows results obtained after deposition of 0.03 ML C_{60} molecules on the surface with each pore accommodating up to 7 molecules [5].

Compared to the bindings previously explained, the van-der-Waals interaction is very weak but it can play an important role in self-assembly of organic molecules such as fullerenes on the Au surface. This will be explained in more detail later in this chapter. All examples presented here highlight the potential of organic

molecules as building blocks for self-assembly of different structures. The wide range of possible bonding strengths as well as the great control and flexibility over their synthesis makes organic molecules even more favourable. Metallic surfaces also play an important role in forming and analysing these structures as some surface analysis techniques like scanning tunnelling microscopy (STM) requires conductive samples. One of these well studied surfaces is Au (111).

2.2 The Au (111) Surface

Gold is one of the most inert metals in nature, which makes it interesting for studies both in vacuum and ambient conditions. Apart from the inertness, the surface structure of Au (111) is the most surprising feature observed from metal surfaces [33]. Bulk gold is known to have a face centred cubic (fcc) structure. Fcc and hexagonal close pack (hcp) are two different lattice arrangements where atoms have high packing efficiency. The difference between these two structures is shown in figure 2.4.

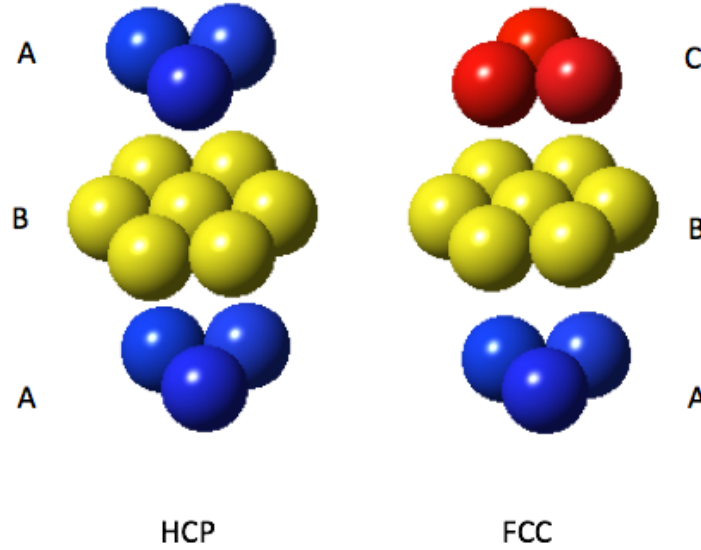


FIGURE 2.4: Hcp and fcc are two different lattice arrangements with high packing density of atoms. These structures are also known as ABA and ABC respectively.

As shown in the figure 2.4, fcc structure is formed by ABC staking and hcp by ABA stacking of atoms [34]. In ideal cases the (111) surface of fcc materials should have a hexagonal closed packed arrangement. But for Au it is different with its (111) surface showing reconstruction patterns [33]. This structure was initially observed from TEM images of Au particles grown on MoS_2 . Images obtained showed fringes with 63 \AA spacing in $\langle 112 \rangle$ directions that was suggested to be the surface reconstruction pattern [35, 36]. Previous LEED studies indicated about 5 % contraction on this surface, but it was the first time that reconstruction patterns were observed [37]. TEM results also confirmed the requirement for a clean surface and sensitivity of Au reconstruction to contamination. This explained failure of earlier experiments in the discovery of it [35, 36].

Furthermore, high resolution TEM images were used to confirm the existence of contraction (4.5 %) along the $[1\bar{1}0]$ direction and measure the unit cell of reconstruction pattern as $22 \times \sqrt{3}$ [38].

Contraction reported is known to be a result of shortening in bond lengths. Since gold atoms on the surface have a lower coordination number, compared to atoms in bulk, their bond length is expected to be shorter. Theoretical calculations were also employed to explain the surface contraction and reconstruction patterns. One of the early models used was the Frenkel-Kontrova. In this model, surface was considered as a single layer where atoms are interacting with each other by springs. This layer is then assumed to be on substrate potential to represent the bulk model. However, atomic vibration has not been considered, so it can only be applied at 0 K [39].

U. Harten et al. [40] then suggested an improved model for the Au surface using high resolution Helium Atom Diffraction (HRHAD). In this model, 23 Au atoms were placed on 22 positions on the Au surface. Position of surface atoms, with respect to the fcc bulk sites, can be divided into three groups. Atoms can be placed on the “C” position (based on figure 2.4) of crystal arrangement to form fcc, or “A” site for hcp structures. Final group correspond to atoms in transition region between fcc and hcp areas. Atoms in this region form strips known as discommensuration lines (DLs). This is in agreement with the stacking-fault model that suggested surface atoms occupying fcc (ABC) and hcp (ABA) sites alternately [41]. In this new model position of the atoms with respect to the x along the $\langle 110 \rangle$ can be obtained by

$$f(x) = \left(\frac{2}{\pi}\right) \arctan(e^{x/\Delta S}) \quad (2.1)$$

where ΔS is the full width at half maxima (FWHM) of a soliton centred between atoms positioned on “A” and “C” [40]. The model suggested is shown in figure 2.5.

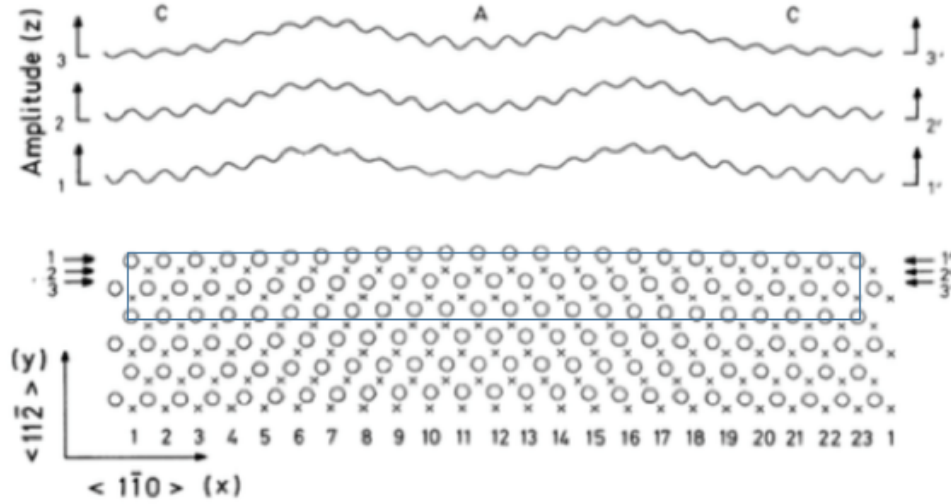


FIGURE 2.5: The model suggested for Au (111) surface is presented. Top image shows the side view and displacements of atoms along the z direction. Lower model correspond to the position of atoms. In this model “o” indicates the position of atoms on surface while “x” correspond to the second layer atoms. The blue square on this model is the surface unit cell (from [40]).

STM was then introduced to Au (111) surface studies. Initially large terraces, few thousands Å, of gold surface separated by monolayer steps of ~ 2.4 Å were observed [42]. Later, parallel pairs of lines along $\langle 11\bar{2} \rangle$ direction gained more attention. The gap between pairs was measured to be 63 Å, which agreed with previous results reported from TEM scans. Images obtained also showed the distance between lines within a pair to be ~ 44 Å, while the amplitude of corrugation was measured as $\sim 0.15 - 0.20$ Å.

Images also showed an interesting feature of the reconstruction patterns. On larger terraces, three rotational domains of gold surface can coexist. DLs on such areas, can transit from one domain to another with each domain having a uniaxial contraction along the $\langle 110 \rangle$ directions. As a result of domain transition an elbow with angle of 120° is formed. The resultant periodic zig-zag structure obtained, is known as the herringbone reconstruction. In this structure appearance as well as the direction of neighbouring elbows are different and can be divided into two

types: bulged and pinched elbows that are shown in figure 2.6 [43]. Size of hcp and fcc sites differ depending on elbow types. For the pinched elbows the hcp area is smaller compared to the fcc while on the bulged elbows they are comparable. This is due to the difference in bending of DLs on elbow sites. At these positions one of the lines has an additional row of atoms, forming a pointed elbow that expands the hcp areas and results in equal sections of hcp and fcc. This is known as type-x where atoms on both sides of the elbow are sitting on bridge-sites with different orientations. On the other hand if atoms on bridge-site have the same orientations, then they can join and form a round shape elbow, also known as type-y [44, 45]. Different types of elbows are labelled in figure 2.6A. An example of uniform reconstruction pattern on large terraces is shown in figure 2.6B. However, presence of any surface defects and steps can interfere and disturb the zigzag pattern of DLs due to the change in surface stress. A surface with disturbed reconstruction pattern is presented in figure 2.6C.

So far contraction has been introduced as the main reason for the formation of reconstruction patterns but surface stress is another important factor. As mentioned earlier, surface atoms have shorter bonding lengths within the surface plane due to the lower coordination numbers. Calculations have shown that in this situation unreconstructed surface will be under stress. To relieve this stress defects are normally formed which appears as reconstruction pattern on Au surface [46]. In this case, surface compression reaches its maximum at elbow sites, about three times higher than at the reconstruction lines, which makes them more favourable during deposition experiments [47].

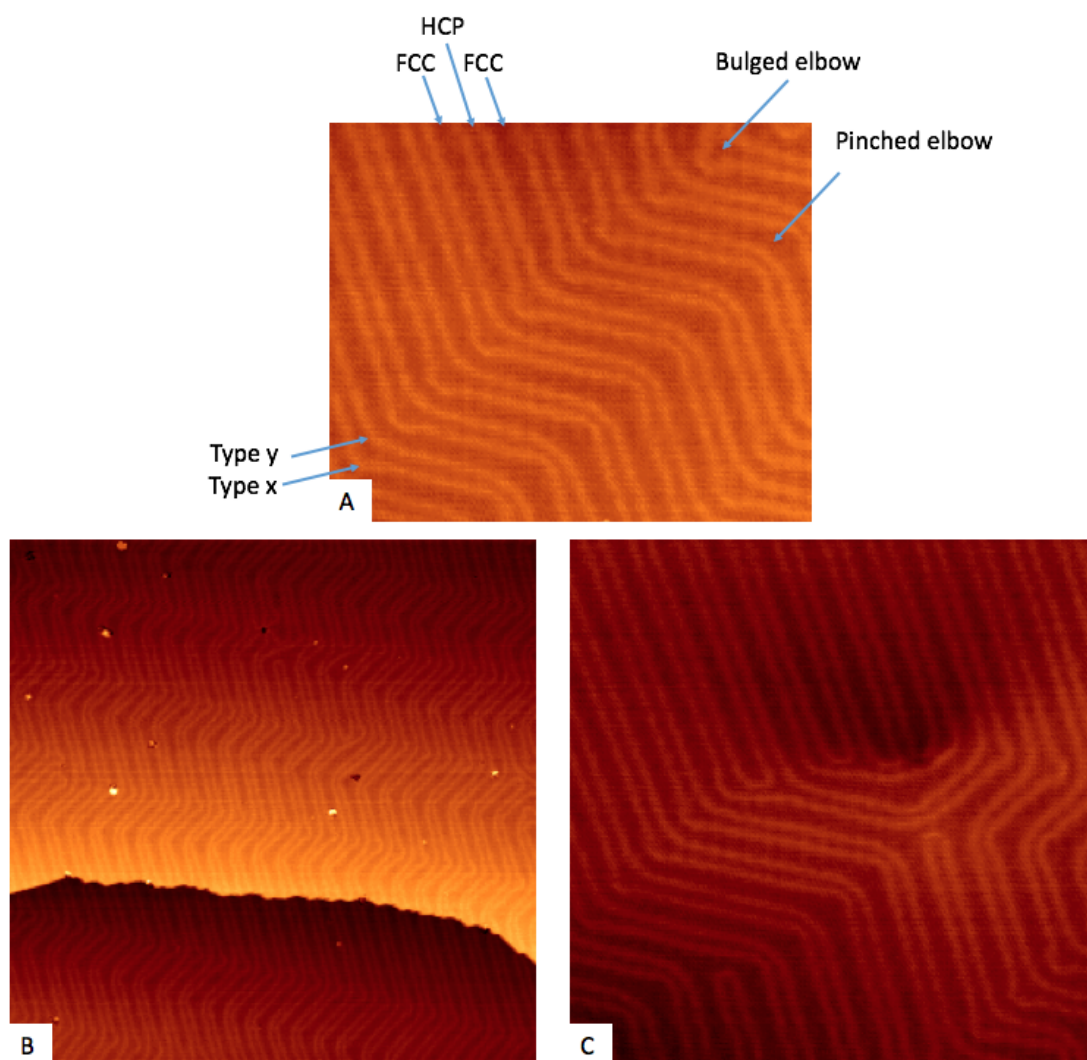


FIGURE 2.6: A) Different features of the Au (111) surface have been labelled on this image. B and C show two different areas of a clean Au surface and its reconstruction pattern. In figure B, a uniform zig-zag structure of discommensuration lines can be seen. $169.6 \text{ nm} \times 169.6 \text{ nm}$, $V = -1.89 \text{ V}$, $I = 0.04 \text{ nA}$. In image C, the reconstruction pattern has been disturbed due to the presence of surface defects. $81.5 \text{ nm} \times 81.5 \text{ nm}$, $V = -1.61 \text{ V}$, $I = 0.05 \text{ nA}$.

STM can be used not only to study surface topography, but also investigate the electronic properties of surfaces. This is known as scanning tunnelling spectroscopy (STS). STS can probe both occupied and unoccupied states. To do so, the STM tip is positioned on an area where voltage will be ramped while current is being measured. During this time, the feedback loop should be kept off to avoid changes in position of the tip. If voltage is measured in eV scales, then the data obtained

can be interpreted with energy scales corresponding to the surface energy levels [48]. K. Schouteden et al. [49] has performed the STS analysis on different regions of the Au surface and the curves obtained are shown in figure 2.7.

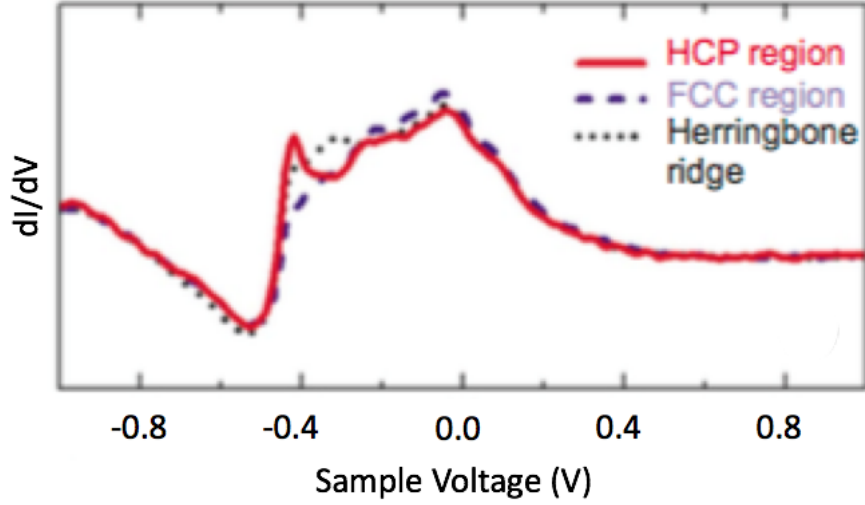


FIGURE 2.7: The dI/dV curve obtained from different parts of the Au (111) reconstruction pattern (from [49]).

The step like feature observed from hcp areas at ~ 460 meV is an indication that hcp sites are mainly occupied by low energy electrons while fcc areas have more electrons with higher energies. This is known as the signature of the Au (111) surface and can be used to check the quality of the STS calculations.

Due to the presence of the surface states, electron waves can propagate on the surface and scatter off the step edges. As a result of interference between incident and reflected waves, standing waves have been observed on the surface [50, 51]. This observation can be made at room temperature but the majority of investigations are done at low temperatures due to the coherence length being larger. Results obtained have also shown that imperfections such as grain boundaries and defects as well as herringbone reconstruction can influence the standing waves formed. This effect varies between different parts; in fcc sections the average corrugation

tends to decrease compared to hcp and soliton-walls, which is believed to be a result of the difference in local density of states (LDOS) [51].

In another study Y. Hasegawa and Ph. Avouris [52] looked at the spatial map of $(dI/dV) / (I/V)$ over an entire scan area, in order to examine the LDOS on the surface. In their study, steps appeared to be brighter which indicates higher LDOS at these sites. This increase can act as a potential barrier to reflect electrons and form standing waves, which agreed with the earlier results obtained from the LT scans.

2.2.1 Steps on Au (111) Surface

Surfaces with periodic arrangement of steps are known as vicinal surfaces. Au (111) vicinal surface is commonly used in self-assembly studies due to its potential in growth of one dimensional structures such as nano-wires [53]. In order to have a better control on growth of structures, a good understanding of interactions between reconstruction pattern and steps is required. From scans obtained it has been observed that reconstruction lines act differently once they encounter a step edge. This difference is dependent on the step edge direction. If the step is descending along $[11\bar{2}]$ (or $[\bar{2}11]$ or $[1\bar{2}1]$) direction with $\{111\}$ microfacet, it is known as step A. When DLs reach such step edges, they can pass without being disturbed. Second group of steps, known as step B, are ascending along $[11\bar{2}]$ (or $[\bar{2}11]$ or $[1\bar{2}1]$) direction and expose $\{100\}$ facet. In this case lower side of step encounters a line parallel to its edge. Since atoms close to the descending step are in fcc sites, based on their bulk arrangement, a line is required to separate the fcc and hcp areas [43, 54]. Figure 2.8 shows two possible types of steps.

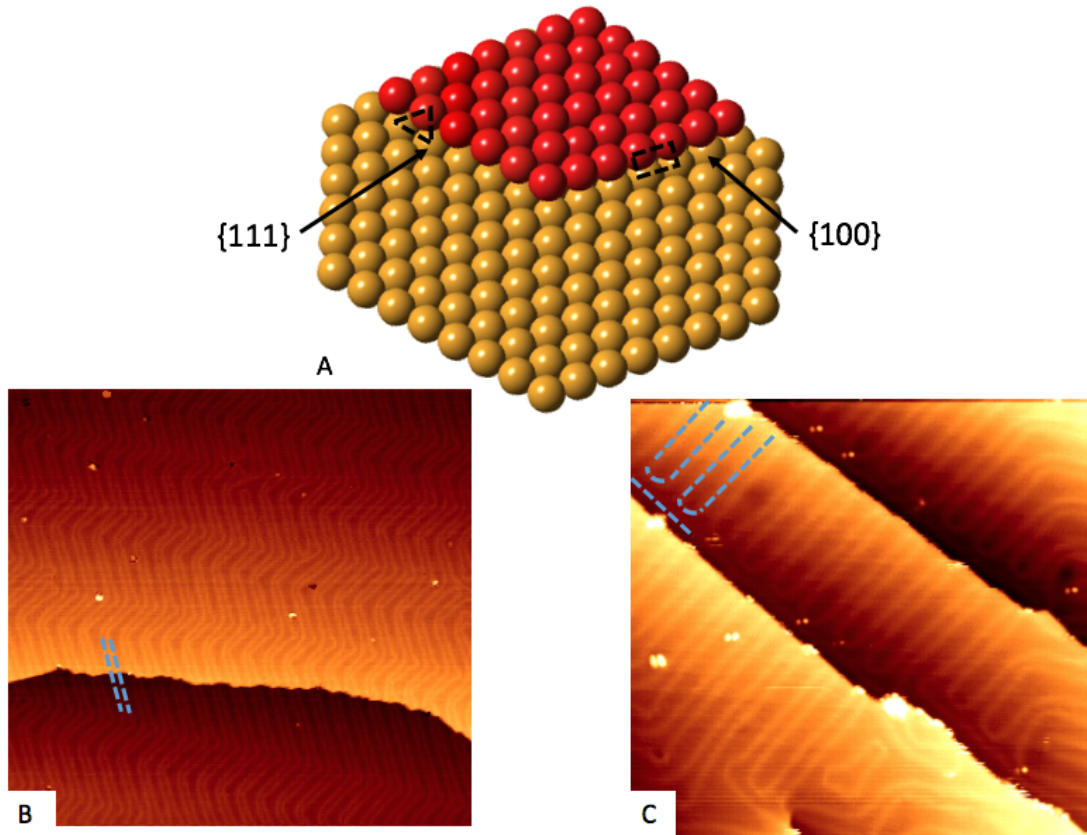


FIGURE 2.8: A) Schematic model of Au (111) surface with two kinds of steps is presented with packing arrangement on each step being highlighted and labelled. B) Scan obtained from steps A where DLs can pass over without being disturbed. $169.6 \text{ nm} \times 169.6 \text{ nm}$, $V = -1.89 \text{ V}$, $I = 0.04 \text{ nA}$. C) In step B, DL cannot pass over which results in formation of a line parallel to the step edges. $71.6 \text{ nm} \times 71.6 \text{ nm}$, $V = -1.89 \text{ V}$, $I = 0.04 \text{ nA}$. Blue lines on these images highlight the interaction of RLs with steps.

As shown, steps can greatly influence the reconstruction pattern. If the density of steps is too much, then surface atoms can relax around step edges and therefore remove the reconstruction pattern [55]. In order to increase the density of the steps and form a vicinal surface, small angle difference with respect to the close pack direction of surface is required [55]. An example of this is Au (788) which has 3.5° disorientation towards $[11\bar{2}]$ direction compared to the (111) surface. Resulted surface is covered with type A steps, where DLs can pass over without being disturbed as shown in figure 2.9. In this image DLs tend to form a V shape pattern. As atoms under the Au steps are located in bulk (fcc) sites, an expansion

of fcc areas close to the lower side of step edges are expected. This results in the formation of the “V” shape patterns observed [55].

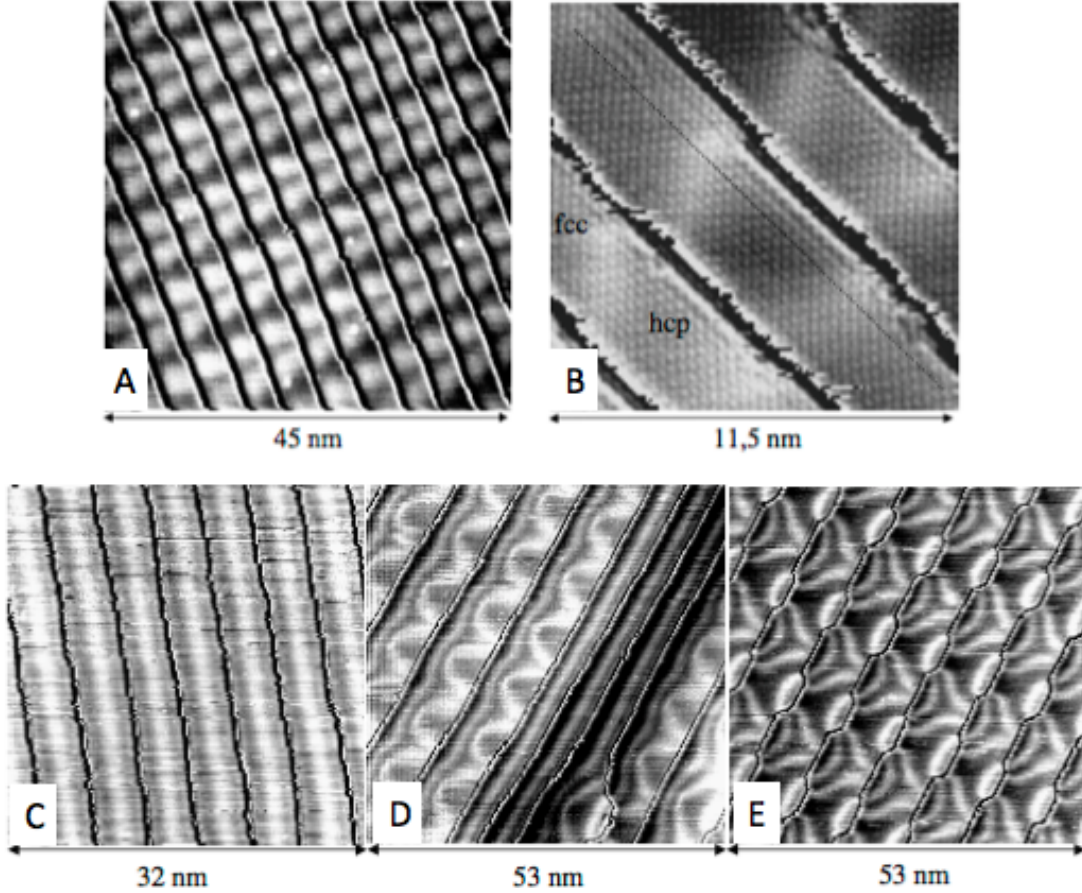


FIGURE 2.9: Steps observed on Au vicinal surface are presented. Scans A and B are obtained from Au (788) with type-A steps, which allows reconstruction lines to pass over without being disturbed. B) A zoomed in scan with atomic resolution shows DLs forming a V shape pattern due to expansion of fcc areas on the lower side of the step edges. Scans on second row are obtained from Au (12, 11, 11). The DLs pattern formed on these step varies depending on the size of steps. For smaller islands (C) straight lines are formed. As the size of islands increases (D), normal reconstruction patterns can be observed. On larger terraces, like E, triangular shapes with super-kinks are obtained that increases the fcc areas (from [55]).

It is also possible to have a surface with $\{100\}$ steps; an example of this is Au (12, 11, 11) which has angle of 2.38° towards $[2\bar{1}1]$ direction as presented in figure 2.9. Steps on this surface are less stable and therefore the width of islands formed tends to vary. As a result, different reconstruction patterns have been observed. If

the island size is very small, a single line along the step edge direction is formed. This helps in separation of the fcc regions, towards the lower edges, from the hcp on the upper sides. Normal $\{100\}$ step structures were observed for slightly larger islands. For terraces that are wide enough, the reconstruction pattern forms a triangular structure with a super-kink along their edges to reduce the step energy. This way, larger fcc areas are formed at the lower side whilst hcp areas are near the upper steps [56].

Steps can also be modified by increasing the electric field under the STM tip. It has been shown that by keeping the voltage constant (~ 1.5 V) and increasing the current to ~ 30 nA, it is possible to form tooth-like structures from existing step edges. Fingers formed tend to grow in $[110]$ direction. Scanning in this direction can also help to increase the growth rate [57, 58].

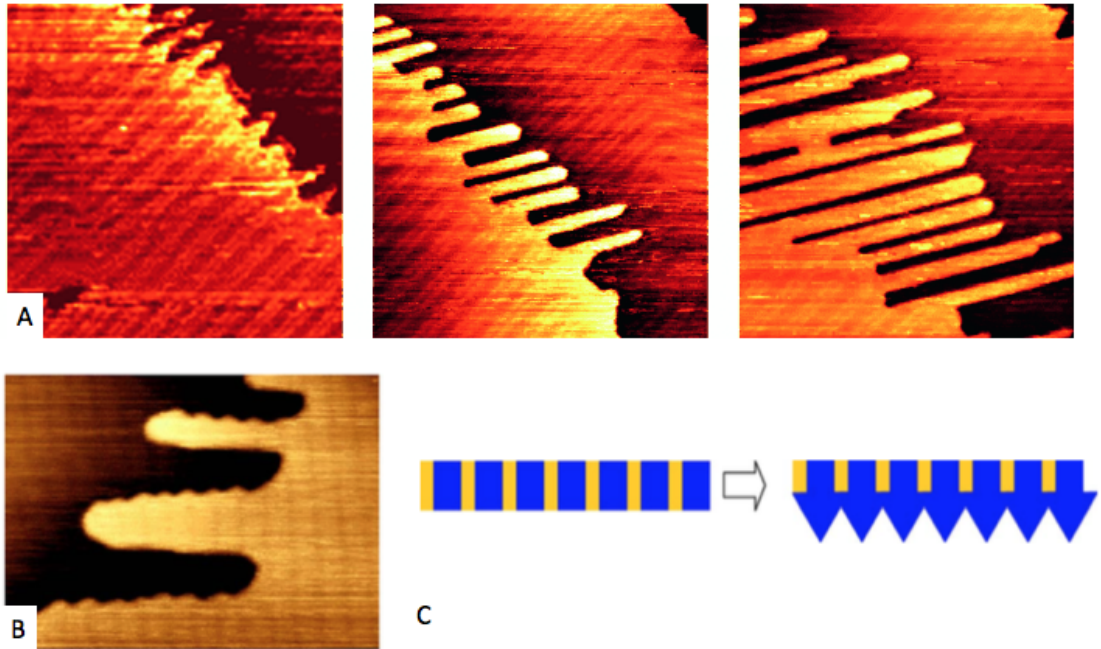


FIGURE 2.10: A) Step by step formation of Au fingers on the surface. This can be achieved by increasing the electric field under the STM tip. B) After annealing, gold fingers grow in the direction perpendicular to the reconstruction pattern along the steps with $\{100\}$ facet. C) Model for Au fingers before and after annealing (from [57]).

Fingers formed on Au (111), are stable up to 380 K. Below this temperature, in order to reduce the high energy of type-B steps, Au atoms move towards fcc areas and form small sections with $\{111\}$ microfacet. As a result, a saw-tooth structure can be observed. If temperature is raised above 380 K, fingers melt and move to their original positions. Such surfaces can be used as template to produce nano structures and devices [57].

2.3 Metal on Au (111)

Metal films play an important role in wide ranges of technological applications, from microelectronics to data storage and coatings. This attracted many researchers to focus on understanding the growth and properties of metal films under different conditions [59].

One of the surfaces commonly used in deposition experiments is Au (111). This is mainly due to three major advantages of this surface: Firstly, inertness of the gold makes it suitable for doing experiments under UHV conditions as well as in ambient [60, 61]. Secondly, the surface reconstruction pattern and its zig-zag structure can be used as a natural template [40]. And finally, apart from Au single crystals, Au films can be grown on mica or HOPG surfaces. Annealing substrate before and during deposition as well as lower deposition rate of Au atoms can help in producing samples with larger terraces (of few hundreds of nm) [62].

A wide range of metal atoms have been deposited on the Au (111) surface in order to study their growth structures. Observations made can be classified into two groups. The first group of metals form islands on elbow sites. This includes Pt [63, 64], Ni [44, 65], Fe [66], Mo [67, 68] and Co [66], where atoms deposited move on the Au surface until they reach an elbow site. It has been suggested that exchange of metal and Au atoms would result in local surface alloying. The

preference of replacing atoms at elbow sites is due to the lower coordination of Au atoms at these positions, as well as being highly strained, which makes the process favourable. Embedded atoms can then act as a centre of growth. Further deposition would then result in the expansion of existing islands [69]. An example of such surfaces is shown figure 2.11.

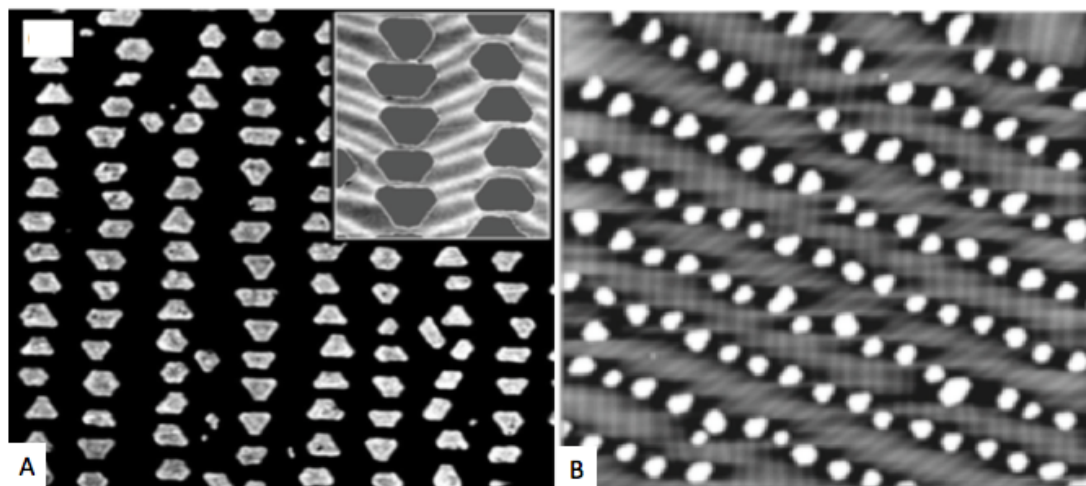


FIGURE 2.11: Different examples of metal islands grown on Au surface are shown. A) 0.25 ML of Ni was deposited on Au (111) at 300 K. The inset shows clearly the position and orientation of the clusters on elbow sites (from [70]). B) Scan obtained after deposition of 0.26 ML Co at 300 K on Au (111) surface that resulted in formation of islands on elbow sites (from [71]).

In order for the exchange process to take place, surface free energy as well as heats of sublimation for the metal atoms need to be higher than Au. Table 2.2, shows these values for some of metals described. In this table, there are three types with higher energy values compared to the gold that have preference to form regular islands on elbow sites. Metals with lower values (Ag and Al) tend to act differently [69].

Element	Surface free energy (eV)	Heat of sublimation (eV)
Ag	0.50	2.95
Al	0.56	3.39
Au	0.72	3.79
Ni	0.90	4.45
Co	0.94	4.40
Fe	0.96	4.32

TABLE 2.2: Surface free energy and heat of sublimation values for different metals in comparison with Au are presented. Values obtained from [69].

At very low coverages, silver atoms deposited on the surface move towards step edges and form finger like structures. By increasing coverages slightly, growth of islands is influenced by the DLs. On larger terraces, the Ag islands are observed on fcc areas between reconstruction lines. If the coverage is further increased, then irregular structures are formed on the surface [72].

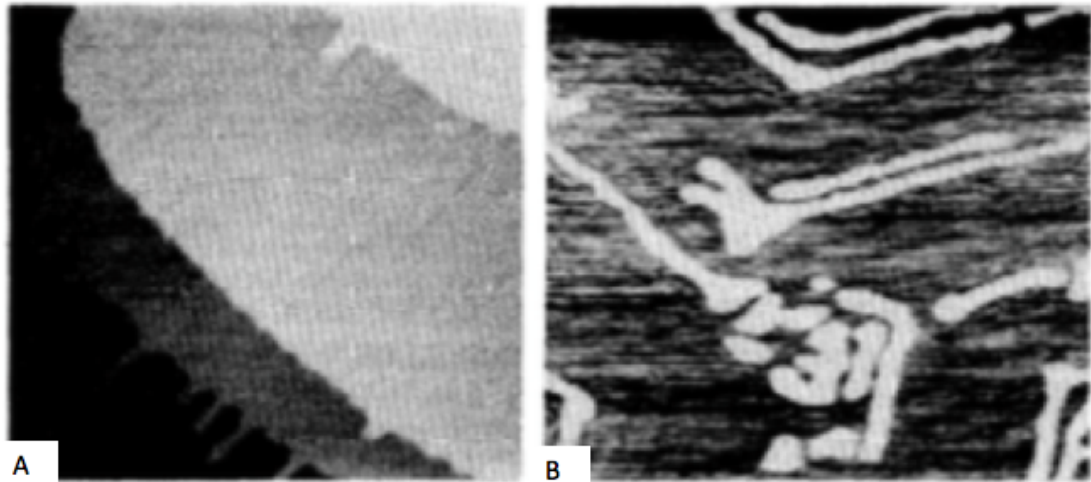


FIGURE 2.12: A) 115 nm \times 115 nm scan showing finger like islands formed on step edges with 1/10 ML of Ag on Au (111). B) Ag coverage was then increased to 1/4 ML that resulted in growth of islands to be influenced by the DLs. 115 nm \times 115 nm (from [72]).

Similar to Ag, at low coverages, Al atoms also move towards step edges. By increasing the coverage, irregular structures are formed. If more Al atoms are then added to the system, larger islands of intermixed Au and Al atoms will be created [73, 74]. An example scan area is shown in figure 2.13A.

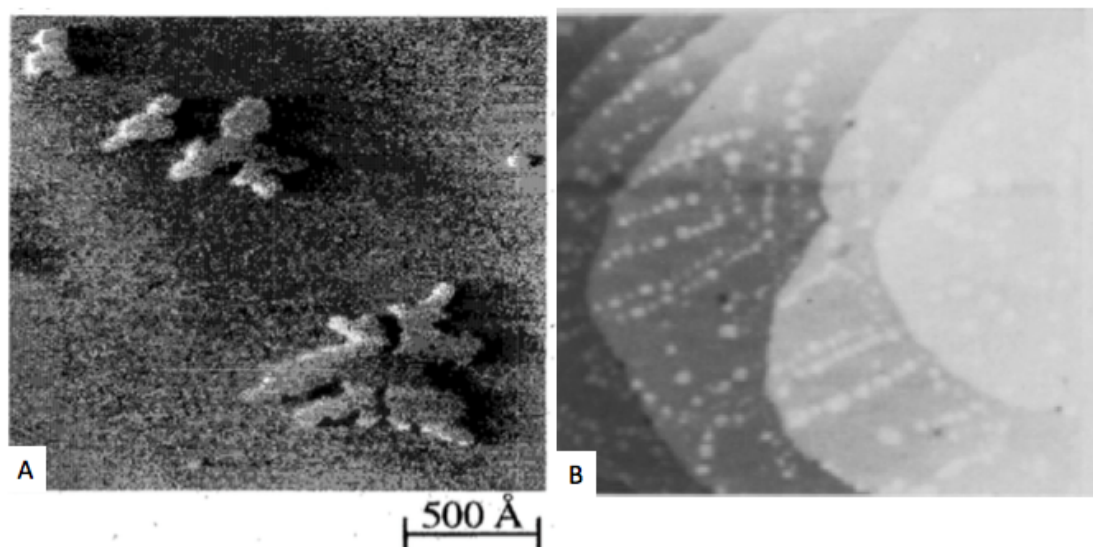


FIGURE 2.13: A) Formation of random Al islands on Au (111) with 1/5 ML coverage at room temperature was observed (from [74]). B) Scan of Au on Au (111) with 1/10 ML coverage shows islands are formed on elbow sites (from [75]).

Unlike other metals explained, Au atoms have shown different results after being deposited on Au (111) surface. Based on C. A. Lang et al. [75] results, at very low coverages, small Au islands can form on elbow sites. By adding more Au atoms, islands formed will grow in random sizes. It is important to note that the outcome obtained is very dependent on the diffusion rate and deposition flux [73]. Therefore, at RT with low deposition flux, Au atoms move towards step edges and form irregular structures.

Apart from metal deposition, many organic molecules have also been studied on the Au (111) surface. In these studies it has been observed that organic molecules tend to be very mobile at room temperature. For site specific growth, the sample's temperature should be controlled. One of the well-studied groups of organic

molecules is fullerenes. In next section, a short description of the most abundant types of fullerene molecules and their arrangement on metal surfaces is described.

2.4 Fullerene

Fullerenes are hollow caged molecules formed of only carbon atoms. Early works on fullerenes were done using an intense laser pulse to evaporate materials from graphite surfaces. These materials were then analysed to identify fractions of carbon atoms removed from samples. Both experimental and theoretical works, suggested that carbon clusters up to 10 atoms tend to form linear chains while between 10 - 30 atoms rings with certain sizes are observed. For clusters above 40 atoms, cage structures are suggested with majority being formed of 60 carbons. Results obtained from mass spectrometry have shown that formation of structures between 30 to 40 atoms is unlikely to happen [76].

After observation of the high abundance and stability of C_{60} cages, Koroto and Smalley [77, 78] studied this molecule in more details. They suggested that, 60 carbon atoms can form a very stable structure with hexagons and pentagons in a ball shape so that no atoms have any dangling bonds. Since then C_{60} , also known as buckminsterfullerene or buckyball, has been studied extensively [77]. Here a short introduction to this molecule and the next stable structure of fullerenes, C_{70} molecule, is provided.

2.4.1 C_{60} Molecule

C_{60} was discovered in 1985. By the 1990s, the methods required to produce and isolate this molecule in macroscopic scales were introduced [79]. Since then there have been many studies on properties and applications of C_{60} cages. The physical structure of it has been defined as a spherical cage made of 60 carbon atoms

arranged in a way to form 12 pentagons and 20 hexagons, with no two pentagons sharing a bond. Therefore, each carbon atom is covalently bonded to three others. In this case a double bond formed between two adjacent hexagons, known as 6:6 bond; and a single bond between a pentagon and a hexagon, called 5:6 bond is expected. Carbon-13 Nuclear Magnetic Resonance (NMR) experiments have shown that after thermodynamically freezing the molecules at about 77 K, the average bond length of a single bond is 1.45 ± 0.015 Å while for a double bond it has been measured as 1.40 ± 0.015 Å [80, 81]. Diameter of this molecule, in gas phase, was measured to be about 0.71 nm using electron diffraction results [82]. Figure 2.14 represent a diagram of a C_{60} molecule.

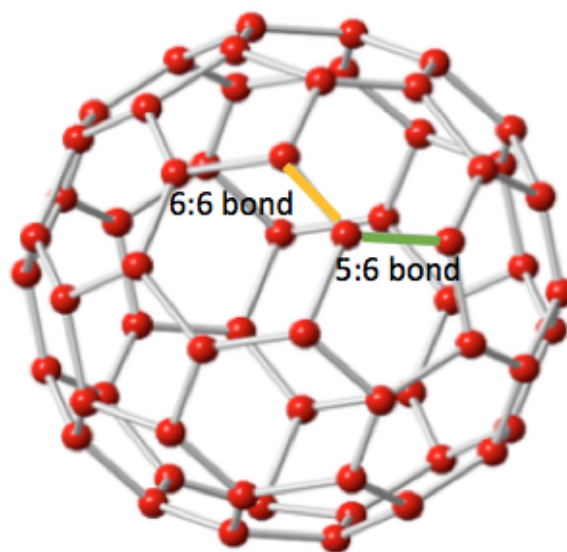


FIGURE 2.14: Schematic diagram of a C_{60} molecule with 5:6 and 6:6 bonds highlighted.

Solid C_{60} is a black powder formed of small pieces of crystalline. At room temperature the crystalline format of the C_{60} molecules adapt to an fcc structure. This structure was then analysed at different temperatures. Between 320 K to 260 K, C_{60} molecules rotate freely and independently of each other. At 260 K, the first

transition between fcc and simple cubic (sc) structure occur, where molecules start to form orientation ordering. This results in a sudden drop of the lattice constant as shown in figure 2.15. At this temperature both structures can coexist. Below 260 K down to 90 K the cubic lattice constant reduces almost uniformly, while molecules rapidly rotate in their positions. Second phase transition take place at 90 K, where the molecules rotational barrier is larger than their thermal energy. This results in C_{60} molecules to freeze in their positions.

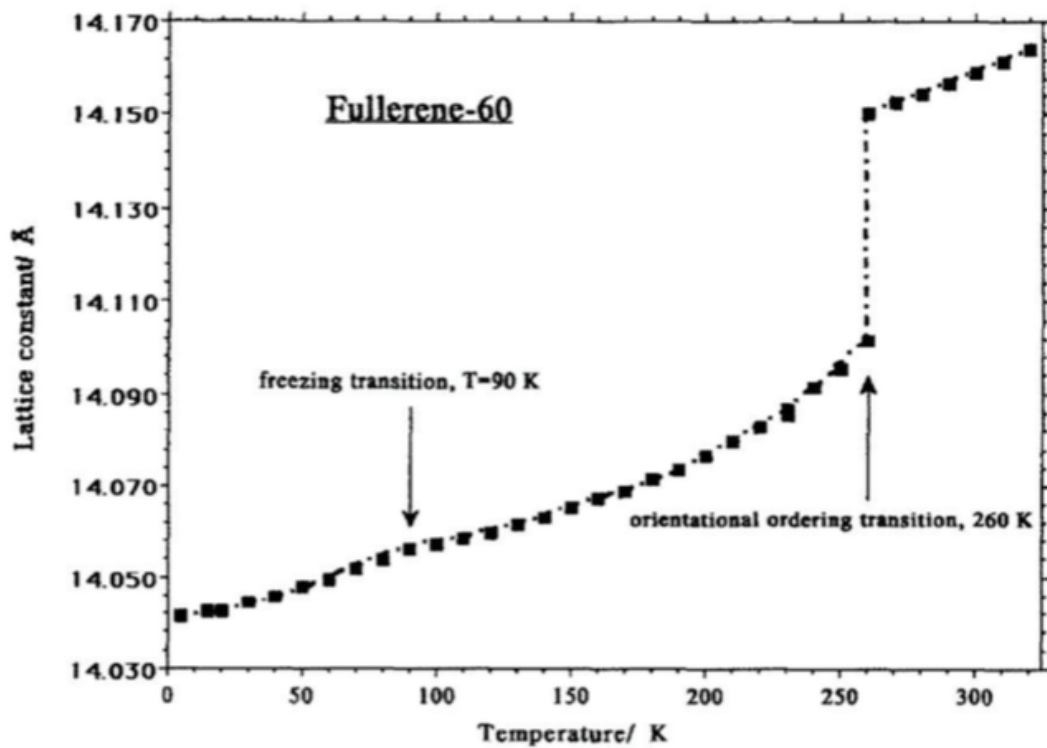


FIGURE 2.15: Changes observed in lattice constant with respect to the temperature shows two phase transitions. First transition was observed at 260 K between fcc and sc structures. At 90 K C_{60} molecules start to orientate in a way that vdW forces is optimized, this is known as the second transition (from [83]).

Finally, once the temperature is reduced to 5 K, C_{60} molecules start to fix in a position that can optimise their interaction. This can be achieved by having each electron-deficient phase (pentagons) parallel to the electron rich (6:6) bonds of neighbouring units [83, 84].

Apart from the geometric properties of C_{60} molecules, electronic structure of the molecule has also been analysed using x-ray photoemission and inverse photoemission [85]. Figure 2.16 shows the graph obtained from these techniques.

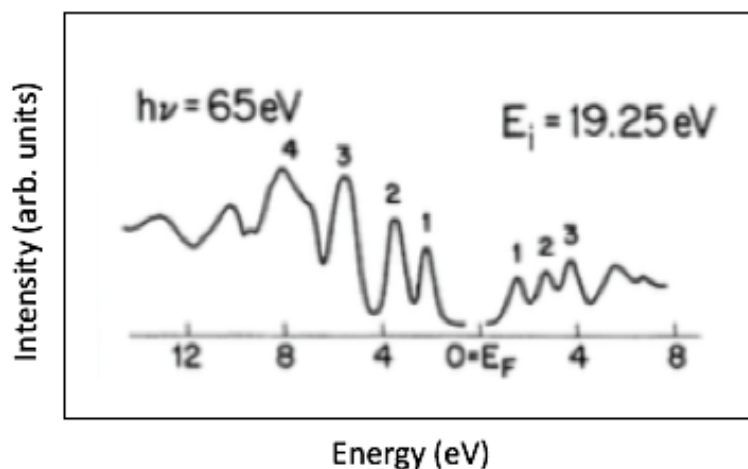


FIGURE 2.16: Graph obtained from photoemission and inverse photoemission showing occupied and unoccupied states of a C_{60} molecule. The HOMO-LUMO gap was measured to be 3.7 eV (from [85]).

In photoemission, a photon with energy of “ $h\nu$ ” is used to excite and emit electrons from occupied states, where “ h ” is the Plank’s constant and “ ν ” is the frequency of photon waves. But in inverse photoemission, incident electrons enter unoccupied levels by emitting photons [86]. Based on the electrons and photons detected, different energy levels have been identified. In figure 2.16, levels labelled as 1 on each side of the fermi level (E_F) are the HOMO and LUMO levels with the gap between them being 3.7 eV [85]. The electron affinity of the C_{60} molecule has also been measured to be 2.65 ± 0.05 eV, which makes it an acceptor during interaction with some surfaces such as noble metals [87].

2.4.2 C_{70} Molecule

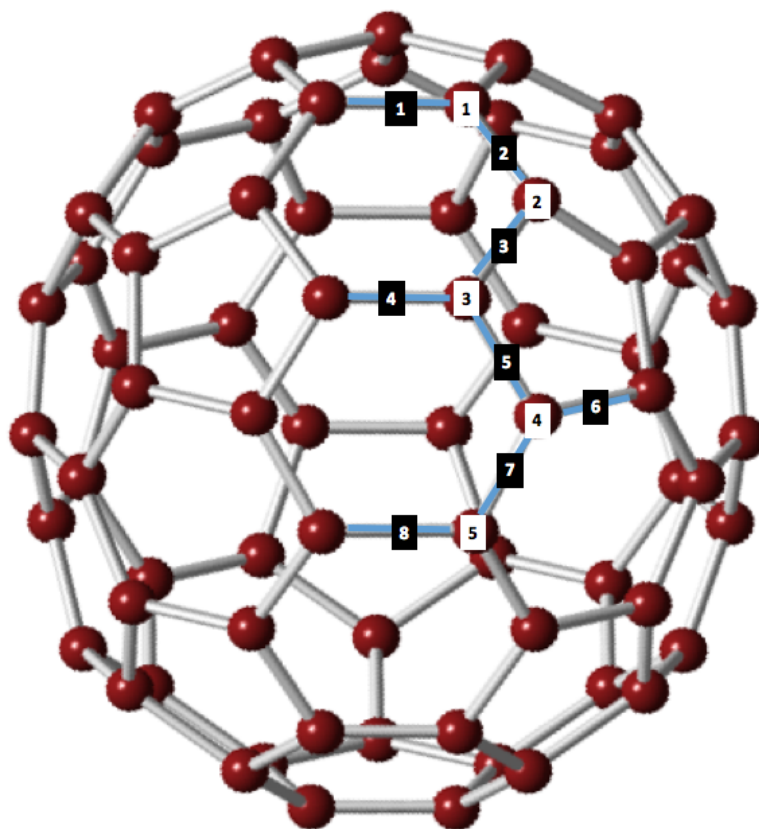


FIGURE 2.17: A model showing Rugby ball shape of a C_{70} molecule is presented. White boxes correspond to the atom numbers and black boxes correspond to different bindings involved in the molecule.

During the production process of the C_{60} molecules, fullerenes with higher molecular weights were also produced. The second highly abundant molecule observed was the rugby ball shaped C_{70} . This is due to the molecules high stability with a binding energy of 7.42 eV/C, that is ~ 0.02 eV/C atom larger than C_{60} molecules. But at the same time more energy is required to overcome energy barriers and form a molecule with 70 carbon atoms. This makes the C_{60} molecule more favourable during production process.

The geometric shape of C_{70} molecules can be visualised as a C_{60} molecule with 5 hexagons around its equatorial plane. The resultant structure has diameter of

7.96 Å along its long axis and 7.12 Å as its short axis [76, 88]. A diagram of this molecule is shown in figure 2.17.

Many theoretical studies have been performed to understand the geometric conformation and bonding lengths of C_{70} molecules better. Bindings involved in this molecule can be divided in to 8 different types, unlike C_{60} which only has two. Different bonds have been highlighted and numbered in figure 2.17. The value corresponding to each bond length is estimated based on a computational model (Hartree-Fock method) [89], and is shown in table 2.3.

Bond type:	C_1-C_1	C_1-C_2	C_2-C_3	C_3-C_3	C_3-C_4	C_4-C_4	C_4-C_5	C_5-C_5
Bond length/ Å	1.452	1.370	1.447	1.356	1.458	1.414	1.403	1.475

TABLE 2.3: Different bond lengths measured from a C_{70} molecule. Atoms have been labelled based on the figure 2.17 (Data from [89]).

The crystalline format of C_{70} , at room temperature, is fcc and rhombohedral (rh) structures with vdW attraction between molecules. Unlike C_{60} that has a phase transition at 249 K from fcc to sc structure, phases of the C_{70} molecules are less characterised [90]. For temperatures ~ 350 K and above, the fcc structure becomes stable. If the temperature is reduced mixture of coexisting fcc, rhombohedral and monoclinic phases can be formed. In other words, at higher temperatures molecules have rotational freedom that results in a formation of fcc structures. By reducing the volume of the crystal (decreasing the temperature to below ~ 270 K), the molecules lateral rotation start to freeze resulting in rhombohedral and monoclinic phases. In a perfect system, where molecules are completely static, monoclinic structure is mainly expected [91–93]. In these models, rhombohedral and monoclinic are two types of structures where crystals can be described by rhombic unit cell and a disordered rhombohedral with unequal vector lengths respectively [94].

The electronic structure of this molecule has also been investigated. The HOMO - LUMO gap energy was measured to be ~ 1.6 eV using photoemission measurements, which is almost half of the value obtained for C_{60} [95]. But the electron affinity of C_{70} molecules (2.72 eV) is comparable with the value estimated for C_{60} (2.65 eV). This indicates that, C_{70} is also an electron acceptor when deposited on noble metals [96].

2.4.3 Fullerene on Metal Surfaces

Self-assembly of molecules is known to be a promising method in the engineering of advanced structures on metal surfaces [12]. Fullerene based materials are especially interesting due to their wide range of applications, from superconductivity at critical temperatures, to transistors. Therefore, many works have focused on understanding the growth of fullerene films as well as interactions involved. Here we looked at the growth properties of C_{60} molecules on different metal surfaces.

2.4.3.1 C_{60} on Au (111)

Over the last few decades, adsorption of C_{60} molecules on noble surfaces has been the subject of many researches. The most common surfaces examined were (111) plane of Au, Ag and Cu. Here a discussion on interaction and growth of C_{60} molecules on the Au (111) surface is presented.

As it was mentioned, STM and STS are suitable techniques for studying nucleation and growth of molecules. Early STM works on C_{60} /Au system reported formation of hexagonal close packed islands on the surface [97]. Further analysis suggested that, for coverage of ~ 0.02 ML, C_{60} molecules are found at the edge of monoatomic steps. Once the coverage is slightly increased, to 0.04 ML, small chains of about three molecules form at the fcc areas of steps, being separated by hcp sections.

By adding more molecules to the surface, islands start to grow initially on the lower side of step edges before expanding to the upper terraces [20, 21]. The preference for lower step edges is due to the higher LDOS at these sites [52]. C_{60} molecules will then form a compact monolayer before moving on to the second layer. Height of molecules on the first layer is measured to be 0.7 nm whilst second layer molecules are about 0.8 nm with each molecule sitting at three-fold hollow sites [20]. Molecules on this layer do not have any preference for step edges due to weaker interactions. The interaction between molecules is by vdW, whereas, molecules on the first layer are bounded by electron transfer from the surface [98]. Photoemission and inverse photoemission experiments have shown a charge transfer of about 0.8 (or less) electrons per molecule which makes it the weakest chemical bond formed between C_{60} molecules and metal surfaces [23, 85, 99]. Due to the difference in bonding types, desorption temperature for the molecules on the first layer (773 K) is much higher than the second layer (573 K). This difference can be used to produce a uniform monolayer by depositing molecules with slightly higher coverage than 1 layer. The sample can then be annealed to about 573 K in order to remove all layers apart from the first one [20].

By comparing the close packed direction of fullerene islands with Au atoms, four different arrangements have been identified [15, 20, 100, 101]. The first structure occurs when the fullerenes closed packed direction is along $\langle 1\bar{1}0 \rangle$, which is also known as “in phase structure”. The unit cell is then formed of 11×11 C_{60} molecules or 38×38 gold atoms, which is normally referred to as $38 \times 38 R0^\circ$, with 0 being the angle between close pack direction of gold atoms and C_{60} molecules. Due to the difference between spacing of fullerenes (1 nm) and the gold lattice constant (0.288 nm) position of C_{60} molecules shifts from threefold hollow site to bridge site and then on a-top site periodically.

Another possible structure is the $2\sqrt{3} \times 2\sqrt{3} R30^\circ$. This structure is formed along the reconstruction lines which run in $\langle 11\bar{2} \rangle$ directions. So, fullerenes molecules

are rotated by 30° with respect to the Au close pack arrangement. Since $2\sqrt{3}$ times the gold-gold spacing (0.998 nm) is almost equal to the lattice constant of C_{60} molecules (1 nm), the unit cell of this structure was chosen as $2\sqrt{3} \times 2\sqrt{3}$. In this arrangement, each molecule is positioned on a-top which makes it a thermodynamically favourable structure [20].

It is also possible to form a 7×7 superstructure with 14° angle difference between C_{60} and gold layer. The 49 molecules forming this structure are positioned on a-top, bridge and then hollow sites [101]. Final structure reported is the 3×3 R 34° , in which every third C_{60} molecule is positioned at identical sites as shown by darker circles in figure 2.18D. In this figure models for other possible structures are also included [15].

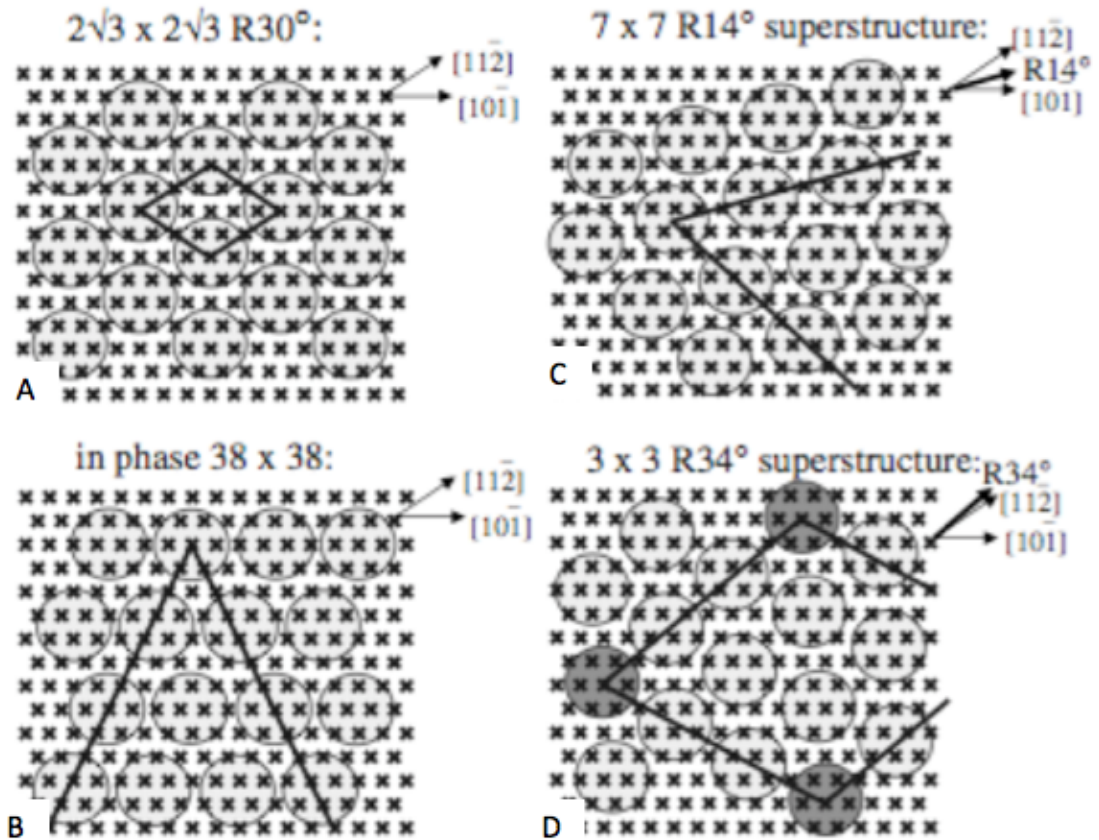


FIGURE 2.18: Schematic diagram of different arrangement of C_{60} islands on Au surface is shown. Circular structures represent C_{60} molecules, “x”s highlight the position of Au atoms and lines included on the image show the unit cells. In model “D” darker C_{60} molecules occupy identical positions (from [15]).

Apart from different close packed arrangements of fullerene molecules, STM images have shown a variation in the contrast of them. The height difference between bright and dark molecules is dependent on the scanning voltage used but in general it varies from 0.35 Å to 1.2 Å, with the largest value being obtained at -1.8 V. This effect is especially more predominate if the surface is subjected to annealing after deposition [15]. An example of molecules with different contrast and their dependence on voltage is shown in figure 2.19.

The arrangement of bright and dim molecules on the surface is defined by the structure of the fullerenes. For molecules in R30° structure, three different patterns have been reported. On this surface there can be no, few or a high density of dim molecules randomly arranged on the surface. Similar to R30° structures, molecules with R0° arrangement can have a few random dim molecules. However, for R14° and R34°, distribution of dim molecules is more uniform. In R14° for every 7 molecules a dim C_{60} has been observed that results in a superstructure with unit cell of 7×7 . But in case of R34° structures, the value of the unit cell is reduced to 3×3 molecules [15].

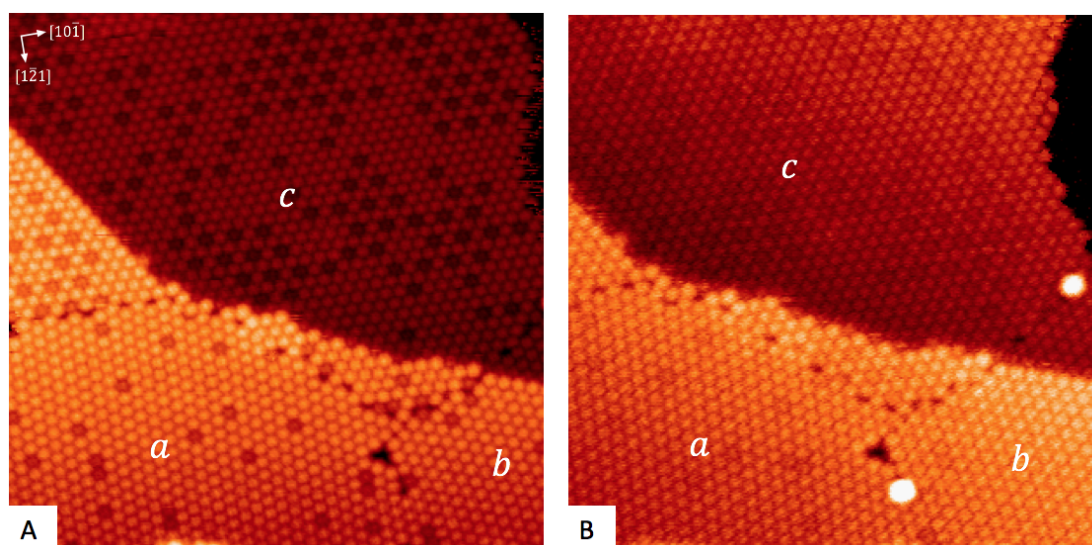


FIGURE 2.19: Different type of fullerene structures formed on Au (111) surface a: $R0^\circ$, b: $R14^\circ$ and c: $R34^\circ$ are presented. Images obtained shows changes in intensity of dim molecules at different voltages. This is an indication of electronic properties of such molecules. A) $39\text{ nm} \times 39\text{ nm}$, $V = 1.21\text{ V}$, $I = 0.05\text{ nA}$. B) $39\text{ nm} \times 39\text{ nm}$, $V = -1.21\text{ V}$, $I = 0.05\text{ nA}$.

Another property of bright and dim molecules is their ability to switch. In the disordered phase this can happen to any molecules on the surface. For $R14^\circ$ and $R34^\circ$ arrangements, where dim molecules are observed at certain positions, only molecules next to dim or within the cluster can switch. From constant scanning of the surface, it has been noted that switching is a reversible process at room temperature. Once the sample was cooled down to 77 K no more switches were observed, which is an indication that this is a kinetically driven process and not a result of the tip [15]. But STM cannot provide any details about the underlayer Au. So theoretical models have been employed to justify formation of dim molecules. Based on these studies, changes observed are a result of nano pit formation, with size of pits being one or seven gold atoms. The binding between C_{60} and Au atoms is more favourable; this can weaken the surface atoms bonds and result in mobility of vacancies on the surface [102, 103]. The mobility of the pits results in the switching of molecules observed. In addition to the existence of nano pits, changes in height variation with potential difference applied, suggest that there is

some dependence on the electronic properties too. For dim molecules located on pits, more charge transfer from surface atoms is expected. This results in a larger resistance for electrons to tunnel to the LUMO states. The difference in electronic structure of molecules contributes to the apparent dimness of them too [15].

Another surface modification observed from C_{60} molecules was the lifting of the reconstruction pattern. The chemical bonds formed between each C_{60} molecule and the Au surface can help in relieving the stress, and relaxing the Au atoms [104]. There have been reports with visible reconstruction pattern on C_{60} films. In these experiments a faster deposition rate was used, which caused a slower lifting process and therefore visible DLs during scanning time [105].

Intramolecular structure of C_{60} molecules was the next challenge to be investigated. This requires a reduction in the sample's temperature or a strong interaction with the surface to freeze molecular rotations. On Au (111), the interaction is not strong enough, so temperature of about 5 K was used to image the molecules with STM. In STM, the electronic states close to the Fermi level (HOMO-LUMO), play an important role in the current detected. For C_{60} molecules LUMO levels are mainly associated with single bands that form pentagons [76]. When imaging empty states, pentagon rings are highlighted in the fullerene cage that can help to identify bonding positions of molecules on the surface. Figure 2.20A shows STM images corresponding to possible orientations at 5.7 K [101].

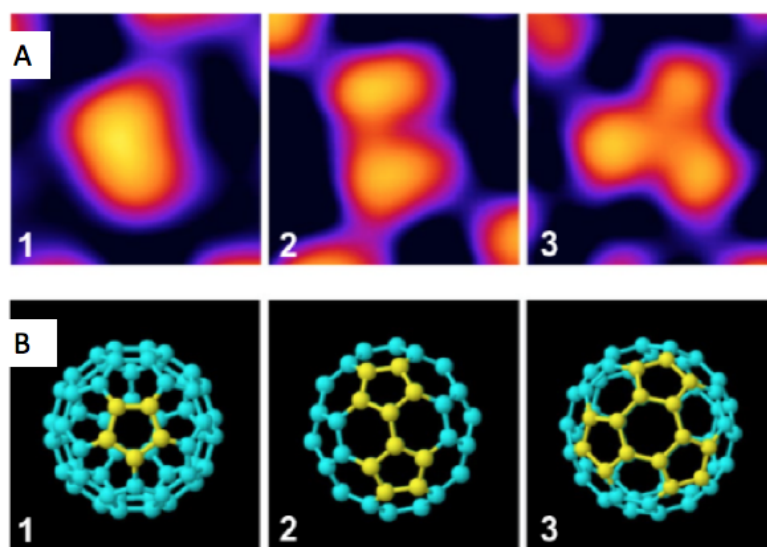


FIGURE 2.20: A) STM images obtained from C_{60} molecules on Au (111) surface showed 3 possible orientations at 5.7 K. In images obtained one, two and three symmetry structures were identified. B) Based on that, models were suggested for bonding positions in each case (from [101]).

As shown in this image three different orientations are possible: 1) C_{60} molecules can have a pentagon parallel to the surface that results in formation of one fold symmetry shape. 2) A two-fold symmetry pattern, when a C_{60} molecule is sitting on the surface with a carbon atom down, was observed. 3) Finally if a hexagon in the molecule is positioned parallel to the surface, another hexagon plus three pentagons would be facing up, in this case a shape with three-fold symmetry is obtained [101]. Model for each scenario is shown in figure 2.20B.

2.4.3.2 C_{60} on Cu (111)

After Au (111), the interaction of C_{60} molecules with other metal surfaces were examined. One of the surfaces that gained a lot of attention was Cu (111) due to its nearest neighbour (nn) distances (2.55 Å) being a quarter of C_{60} bulk crystal (10.0 Å) [106].

Similar to Au (111), studies on this surface started by looking at molecular growth structures. Deposition of C_{60} molecules at RT has resulted in formation of islands with random sizes instead of linear chains at step edges. This is an indication that the bonding between C_{60} and Cu surface is stronger than the attractions between C_{60} molecules [107]. If molecular coverage is then increased further, 2D islands start to grow on the lower side of step edges, until a full layer is obtained. Layers formed have a well ordered (4×4) superlattice in agreement with the nn values provided earlier.

The other noticeable point is the shape of individual C_{60} molecules on the Cu surface. It has been reported that using +2.0 V, three leaf-clovers shapes and for -2.0 V, doughnut like structures were observed. Triangular shapes were also reported for biases close to 0 V. This dependence on voltage is an indication that C_{60} molecules are not free to rotate, with each shape corresponding to a certain orientation of molecules on the surface. For an example the three leaf-clover shape corresponds to the hexagonal ring of the C_{60} parallel to the surface [108]. These positions agree with models suggested for molecules on Au surface. Example of structures observed at different voltages are shown in figure 2.21.

Results obtained from x-ray photoemission (XPS) and high resolution electron energy lost spectroscopy (HREELS) have shown that the LUMO state of C_{60} molecules accept charge from Cu surface [106]. The amount of charge transferred has been estimated to be around 1 - 1.6 electrons per molecule, with 92 % of the charge being localised on the hexagonal ring of the C_{60} molecule [98, 109, 110]. For higher coverages, the second layer of C_{60} molecules are bonded by vdW interactions. So similar to Au (111), the desorption temperature of first layer is about 480 °C while higher layer molecules can be removed at ~ 300 °C due to the weaker bindings formed [98].

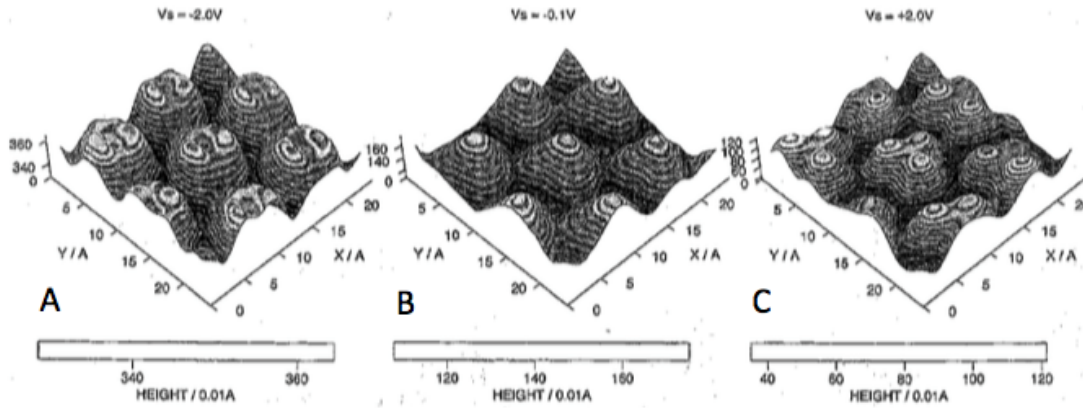


FIGURE 2.21: Voltage dependence of the C_{60} molecules on Cu (111) surface is shown. A) With sample voltage of -2.0 V, molecules had doughnut shape forms. B) Once sample voltage is reduced to -0.1 V, which means states near Fermi level are mainly dominating to the tunnelling current, a triangle shape is observed. Image “C” shows the three lobe clover shape obtained from empty states with +2.0 V sample bias (from [108]).

2.4.3.3 C_{60} on Ag (111)

The final surface of interest is Ag (111), which is especially interesting due to its similar lattice constant (0.289 nm for Ag and 0.288 nm for Au) and similar electronic structure to Au (111) but without the reconstruction pattern. Initial steps of C_{60} growth are also very similar to the Au surface. C_{60} islands start to form along step edges and once coverage is increased, two dimensional islands with hexagonal closed packed arrangement form [111].

T. Sakurai et al. [108] have identified different close packing directions of C_{60} molecules. Structures observed can have 30° , $12.5^\circ \pm 1^\circ$ and $46^\circ \pm 1^\circ$ angle difference with respect to the $\langle 112 \rangle$ direction of the Ag surface. The nn distance of molecules in all phases have been measure to be about $10.0 \pm 0.1 \text{ \AA}$, which is very close to the value of molecules in bulk C_{60} (10.04 \AA).

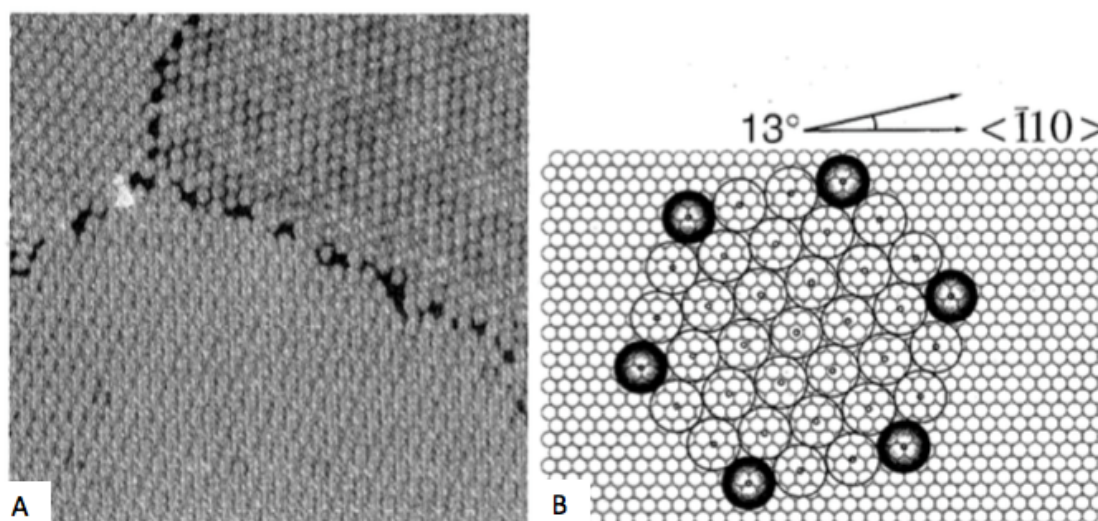


FIGURE 2.22: A) STM scan of the C_{60} monolayer on Ag (111) surface is presented. Three close pack directions with respect to Ag atoms have been reported. The right top is $R30^\circ$, the lower part phase is $R13^\circ$ and the top left is $R46^\circ$. B) In figure B model for molecules in $R13^\circ$ is suggested (from [108]).

Similar to the Au surface annealing the substrate at 300 °C for a long time results in the disappearance and conversion of all phases to $R30^\circ$. The resultant structure would have a $2\sqrt{3} \times 2\sqrt{3}$ unit cell, with molecules being positioned on a-top sites [108]. The bonding formed between C_{60} molecules and the Ag surface is expected to be stronger than Au (111), however, desorption temperature on both surfaces is about 500 °C. This suggests that the difference between their bonding strength is small [21]

Another interesting observation made after annealing the surface for a long time was formation of bright and dim molecules. The coverage of dim molecules on this surface was estimated to be $\sim 38\%$ with a random distribution [112]. Switching between bright and dim molecules was also reported. In order to justify this phenomenon, density function theory (DFT) calculations [113] as well as LEED analysis were employed [114]. Results obtained suggested that Ag atoms, right under molecules, can be displaced to form nano pits with surrounding atoms remaining in their bulk position. In this case C_{60} molecules sitting on nano pits

would have their hexagon ring parallel to the surface that makes them fixed in two possible orientations: 0° and 180° . This orientation difference can result in a change in contrast compared to molecules that can rotate freely on the surface [114].

2.4.3.4 C_{70} on metal surfaces

At low coverages, growth of C_{70} molecules on metal surfaces is very similar to C_{60} , with islands starting from step edges before expanding to form 2D structures. STM scans obtained from C_{70} monolayer have shown that there are two possible molecular orientations on surfaces [115]. They can have their long axis perpendicular to the surface, with height measured to be about 0.7 nm on Au, or have it parallel to the surface, height of ~ 0.65 nm [116]. Due to the presence of these two options, islands formed are more disordered compared to the C_{60} molecules with a nn distance of C_{70} islands being ~ 10.6 Å [115].

The close packed direction of C_{70} with respect to Au has also been investigated under different conditions. The two most common directions observed at RT from C_{60} molecules, $R0^\circ$ and $R30^\circ$ have been reported for C_{70} molecules too. N. Katsonis et al. [117] studied these domains on Au (111)/n-Tetradecene interface. This solid/liquid interface allowed for investigation of self-assembly structures in ambient conditions with height of molecules measured as 13 ± 1 Å for standing up and 11 ± 1 Å for lying down position. From their results it has been suggested that, in $R30^\circ$, the nn value of C_{70} molecules is close to the periodicity of the Au lattice along the $\langle 112 \rangle$ direction (9.96 Å). Therefore, molecules are expected to be in the upright position on three-fold hollow site of gold lattice with unit cell of $2\sqrt{3} \times 2\sqrt{3}$. This is also known as α domain.

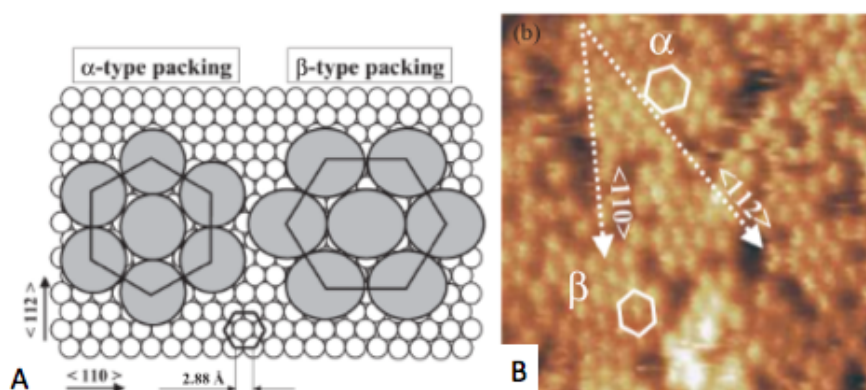


FIGURE 2.23: A) Model for two possible domains of C_{70} molecules on Au (111)/n-Tetradecene interface. α corresponds to the $R30^\circ$ domain and β is the $R0^\circ$ with respect to the Au close pack directions. B) High resolution STM scan of molecules on surface is also presented. This scan shows two different domains that can be formed on the surface (from[117]).

The other domain observed is β -type packing that corresponds to molecules being in $R0^\circ$ phase and arranged along $\langle 110 \rangle$ direction. As the long axis diameter of C_{70} molecule is about four times of periodicity along $\langle 110 \rangle$ direction (11.5 \AA), it is expected that in this phase molecules are laying flat on the surface [117]. Scan and model for these arrangements are shown in figure 2.23.

P. Wang et al. [118] then studied the effect of depositing C_{70} molecules on Ag (111) surface in ultra high vacuum (UHV) conditions. Samples were prepared by depositing about 4.5 ML at room temperature. The first point noted was the formation of second layer structure before completing the first one. This suggests the bonding of substrate - adsorbent being weaker than the interactions between C_{70} molecules. Scans obtained also showed that majority of molecules tend to be in the stand up position that can be explained by considering coulomb repulsions. Since the LUMO orbital in C_{70} molecules is located near poles, the upright position is preferred for two charged molecules. The average charge transfer for each C_{70} molecule on Ag (111) has been measured to be about 2.6 electrons per molecule [119], which is higher compared to the $C_{60}/\text{Ag (111)}$ system (~ 0.5 electron per molecules [120]). The sample was annealed at about 300°C to form a uniform

monolayer. C_{70} molecules on this layer were arranged in $\sqrt{13} \times \sqrt{13}$ R $\pm 13.9^\circ$ structure instead of $2\sqrt{3} \times 2\sqrt{3}$ R 30° that was expected. This is due to the coulomb repulsion that has increased the nn distance of molecules by 0.041 nm and formed new patterns [119].

Similar to C_{60} , after annealing sample, different contrast of C_{70} molecules were reported. Apart from bright molecules (B), three different dim contrasts formed on the surface. The first group are molecules in the lying-down or tilted position with a height difference of 0.05 - 0.08 nm compared to B molecules, known as weak dims (WD). The second group includes molecules that have height difference of about 0.1 - 0.13 nm, called middle dims (MD). These molecules are located on nano pits. Finally, height different of 0.17 - 0.19 nm were measured for dark dims (DM) molecules. This height difference suggests that C_{70} molecules are in laying-down position inside nano pits. Once the temperature is increased to about 380 °C more structures were observed in the upright position that resulted in disappearance of WD and DD molecules [118].

Cu was the next surface that was used to study self-assembly of C_{70} structures. Like other surfaces, molecules initially moved toward step edges and as coverage increased 2D islands started to grow. Based on STM images obtained both landing positions are possible on Cu (111) surface but the preferred orientation is for molecules to stand up similar to other surfaces. The over layer C_{70} molecules form a 4×4 structure with the intermolecular spacing of 10.2 Å, which is close to the distance between C_{70} molecules in the bulk form [121]. The interaction between molecule and the surface is by electron transfer with a net charge of 1.1 ± 0.1 electrons per molecule [122].

Overall bonding of C_{70} on metal surfaces is comparable with C_{60} molecules. Especially since the favoured bonding position has been shown to be the upright direction both experimentally [123, 124] and theoretically [125]. In this case the footprint of the molecule on the surface is almost the same as C_{60} . So for coverages

close to one monolayer, where molecules are densely packed, structures formed are comparable to the ones found with C_{60} molecules.

2.5 Formation of C_{60} - Au Clusters

Combining fullerene molecules with other molecules and atoms can help in production of many new structures including $(Au)_m-(C_{60})_n$ clusters. Self-assembly of Au- C_{60} magic clusters on Au (111) was first reported in our group by Xie et al. [24]. In this section a short description of the cluster production is provided.

2.5.1 Producing Magic Clusters

Earlier in this chapter explanation of how different types of bonding, mainly non-covalent, can be used in self-assembly of structures was provided. Bonding such as hydrogen-bond and metal-ligand interactions have both selectivity and directional properties that can be very useful in production of different patterns like porous networks. Another possible interaction is van der Waals (vdW) that is mainly used to bring molecules or atoms into a close pack arrangement. However, controlling a system with it can be hard. It is expected that as the size of molecules increases, strength of vdW bonding increases as well. This idea was employed to produce, $(C_{60})_m-(Au)_n$ clusters on a clean Au (111) surface. Initially, sample's temperature was reduced to 110 K for deposition of Au atoms. These atoms then move on the surface to reach elbow sites and form islands. The position of Au islands on bulged and pinched elbows is different as atoms start to nucleate from x-type elbows. So on bulged elbows, islands are formed on fcc areas while on pinched elbows they are on hcp sites [126]. Figure 2.24 is an example of a surface area after deposition of 0.01 ML Au atoms. The height profile along the white line shows each island is ~ 0.24 nm, which agrees with a single layer Au island's height.

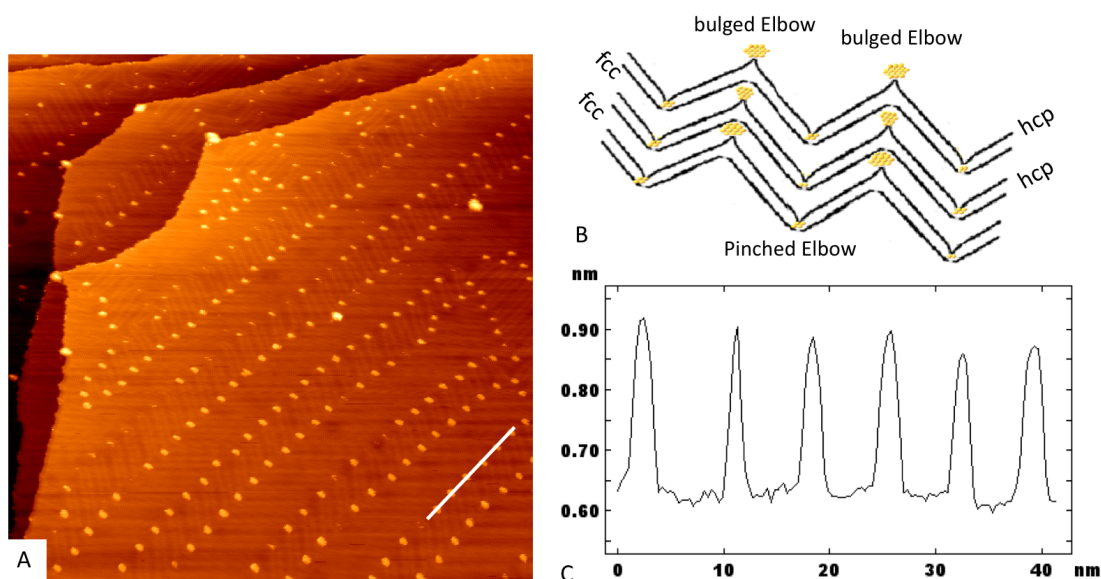


FIGURE 2.24: A) Scan obtained at 115 K after deposition of 0.01 ML gold atoms on Au (111) surface. $181.4 \text{ nm} \times 181.4 \text{ nm}$, $V = -1.89 \text{ V}$, $I = 0.05 \text{ nA}$. Small Au islands start to grow from x-type of elbows, as shown in sketch B. So, on bulged elbows islands are formed in fcc areas while on pinched they are located in hcp sites. Graph C, shows height profile along the white line in figure A, which agrees with single layer Au islands.

Once the formation of Au islands is confirmed, C_{60} molecules are added to the surface. The low temperature of the sample results in the shortening of molecule's diffusion length, but they can still diffuse for a long enough distance to find existing Au islands at elbow sites. Molecules will then encapsulate islands or arrange around them. At this stage, clusters observed can be divided into two groups: closed structures where C_{60} molecules completely cover Au islands and open structures where Au islands are still visible.

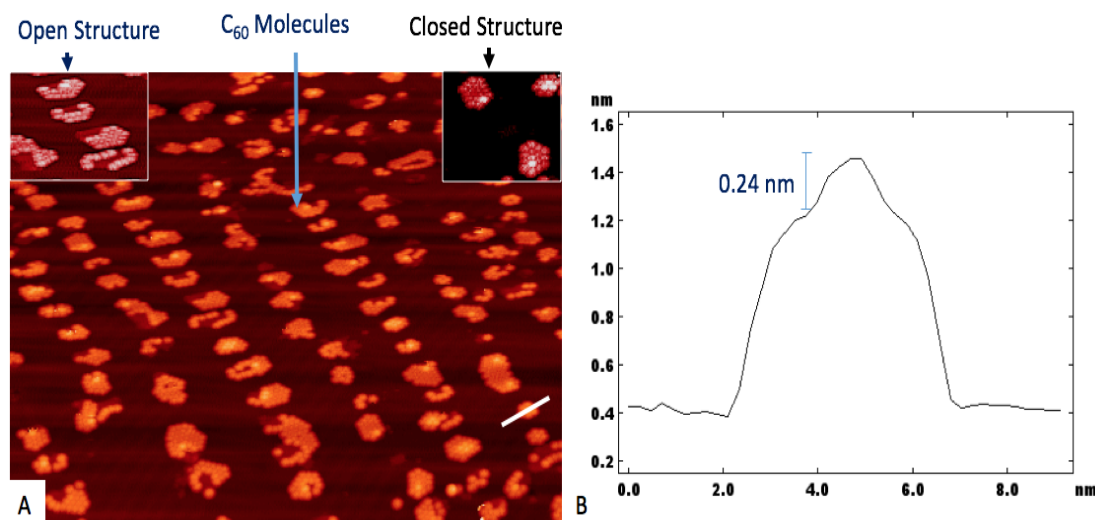


FIGURE 2.25: A) Scan obtained after deposition of 0.21 ML C_{60} on pre-existing Au islands. Clusters formed can be divided into two groups of open and closed structures depending on molecules sitting on top of the Au islands or not. Examples of such clusters are shown by inset in the upper right and left corners respectively. The brighter molecules are the ones sitting on the Au islands. This agrees with the height profile (B) obtained along the white line. 101.2 nm \times 66.8 nm, V = -2.18 V, I = 0.05 nA.

STM cannot reveal directly the under layer Au but the existence of it can be proved with the open structures as well as the height profile of the brighter C_{60} molecules. Figure 2.25B shows the height profile along the white line across a cluster with 7 C_{60} molecules at the bottom right hand side of the image. The central molecule is about 0.24 nm taller than surrounding ones which agrees with the height of one gold atomic layer. In order to produce thermodynamically stable clusters, the sample was then slowly annealed up to room temperature.

2.5.2 Magic Clusters at Room Temperature

As the temperature increases, Au atoms and C_{60} molecules gain enough energy to move around and form the most thermodynamically stable structures. The outcome is stable clusters formed at room temperature on elbow sites as shown in figure 2.26.

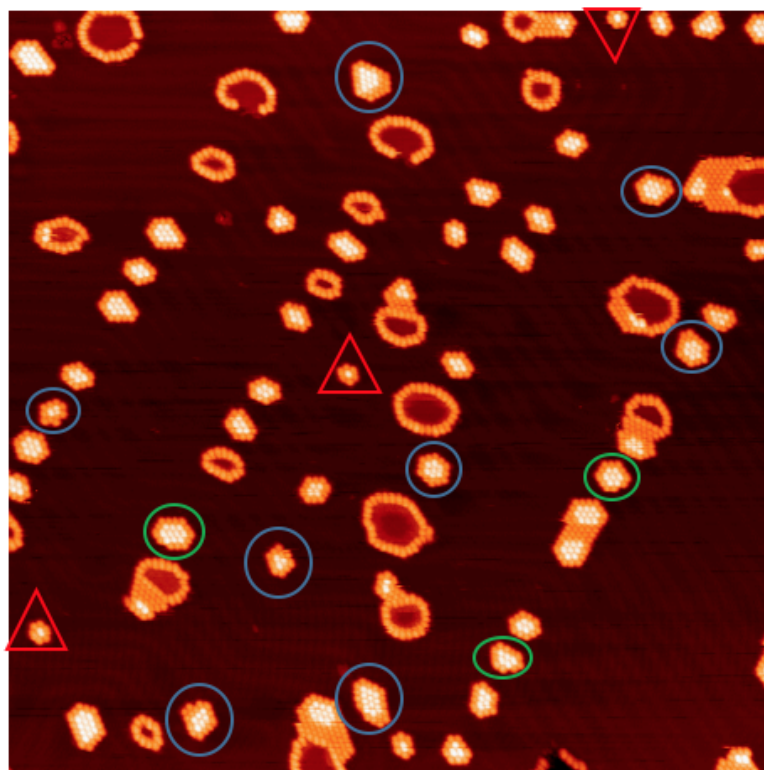


FIGURE 2.26: Scan showing stable structures observed at RT with brighter molecules being located on top of the Au islands. In this scan the smallest stable forms are highlighted in red triangle. Apart from stable structures, clusters with extra (blue circle) or missing (green circle) molecules are also observed. 121 nm \times 121 nm, $V = -1.93$ V, $I = 0.05$ nA.

As shown in figure 2.26, the smallest stable structure is formed by 7 C_{60} molecules with the central one appearing brighter due to it being positioned on top of the Au island. These clusters are highlighted with red triangles. The lateral position of the C_{60} islands in such clusters agrees with the $(2\sqrt{3} \times 2\sqrt{3}) R30^\circ$ arrangement of fullerenes on Au (111) surface. It is expected that a C_{60} molecule occupies an area equivalent to 12 Au atoms [24] with the C - Au atom distance being ~ 0.25 nm [127]. Based on this information a model has been suggested that agrees with the following conditions [24]:

- The optimum distance between C_{60} molecules (1.03 nm) is kept constant. Adding more Au atoms to this system increase the gap between molecules

and reduce their interaction.

- The C - Au distance (0.23 nm) is in agreement with the value suggested. Removing Au atoms from this model can also result in destabilising the cluster.
- The Au island is also arranged to keep its hexagonal closed-shell structure.

Based on these conditions the model recommended for smallest stable cluster is known as $(C_{60})_7-(Au)_{19}$ which is presented in figure 2.27B. This idea was then employed for larger clusters as shown in figure 2.27C and D. In these diagrams, C_{60} molecules are presented as brown molecules, blue are Au surface atoms and yellow correspond to the gold atoms deposited on the surface. Position of molecules on the surface is highlighted by red atoms. C_{60} molecules on top of the Au islands are located on a-top position while molecules around the step edges are on three-fold fcc hollow sites. Apart from magic clusters, it is also possible for closed structures to have extra or missing C_{60} molecules as highlighted in figure 2.26 by the blue and green circles respectively. Slight annealing to about 320 K provides enough energy for extra molecules to move away from structures. These free molecules on the surface can then be captured by other clusters with missing molecules to form stable structures [128].

Further increase in the temperature results in removal of clusters. An island formed of about 7 C_{60} molecules, without the Au atoms, will disintegrate at 240 K on Au (111), but magic clusters can be heated up to 400 K. It may seem that by increasing the size of the cluster the stability would also increase due to higher number of molecules interacting with step edges. However, larger structures have a higher number of molecules sitting on the Au island that are not strongly bonded to the surface compared to the step edge molecules. Therefore, all clusters tend to disappear by 400 K [24].

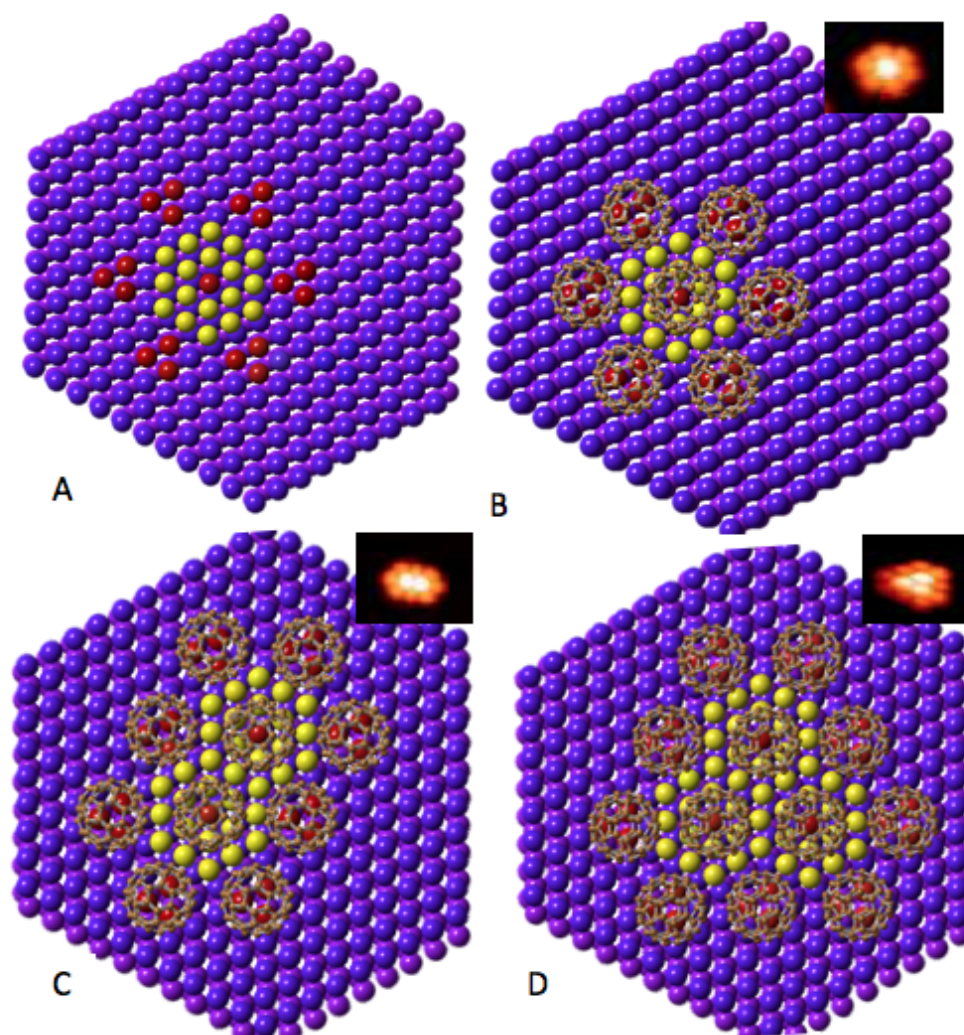


FIGURE 2.27: Models suggested for the magic cluster where blue spheres are surface Au atoms, purple spheres are second-layer Au atoms, yellow corresponds to islands formed as a result of gold atoms deposition and brown molecules are C_{60} . Some atoms are highlighted in red to show the position of C_{60} molecules on the surface. Molecules sitting on the deposited Au islands are located on a-top position while lower level molecules site on hollow sites. A) Model from Au surface without C_{60} cages to highlight the position of molecules in $(C_{60})_7-(Au)_{19}$ cluster. B) $(C_{60})_7-(Au)_{19}$ model C) This can also be applied to the larger clusters $(C_{60})_{10}-(Au)_{35}$ and D) $(C_{60})_{12}-(Au)_{49}$.

In reports published a detailed description of production process and models required to understand magic clusters are provided. However our knowledge and control on size distribution as well as position of clusters are limited and require further investigations. Chapters 4 and 5 of this thesis have aimed to address these issues.

2.6 Sputtering

Sputtering is a result of collision introduced from a beam of energetic neural atoms or ions incident on a target that can be liquid or solid [129]. Here we focus on sputtering a solid sample with an ion beam. During sputtering an energetic beam of ions is directed towards a sample, this results in interactions between fast ions and stationary near surface atoms. The incident ion is then deflected back from a single hard collision or after many correlated collisions. For ion beams with energy higher than few keV, there is increased probability that ions will finally come to rest within the sample [130, 131].

Collisions between ions and solid atoms can be divided into two groups: nuclear and electronic collisions. In nuclear, momentum and energy are conserved (elastic collision). On the other hand, electronic collisions refer to the interaction between ions and lattice electrons. During each collision a small amount of energy is transferred (inelastic collision) until the ion totally loses all of its energy [130]. In both cases, once the energy transferred is high enough for an atom to overcome its binding energy, it can be released from the surface.

The type of ions used can also have an effect on the collisions. For relatively heavy ions, the energy is deposited near the surface and starts a collision cascade that results in the ejection of surface atoms. However, lighter ions such as H^+ and D^+ are reflected from beneath the surface layer. If the energy of the ions is higher

than the surface barrier any recoil atoms can sputter off the surface. For ions with intermediate mass such as Ar both case can happen [132].

In order to study surfaces during and after the bombardment, different methods such as thermal energy atom scattering (TEAS) and low energy ion scattering (LEIS) are commonly used. STM can also be an ideal technique that allows studies of the surface morphology after the bombardment [133].

B. Poelsema et al. [134] used TEAS measurement to analyse the effect of He ion bombardment on a Pt (111) surface. Their results suggested that majority of ions create mono-vacancies even though the sputtering yield of it is larger than one (sputtering yield will be explained in the following section). It was also observed that based on the sample's temperature during sputtering, mono-vacancies can move as their lateral movement is thermally activated. At room temperature, vacancies may reach a step edge and join it or meet others and form a cluster. So temperature is another factor that can be controlled to produce desired samples.

Generally, ion sputtering is known to be a cheap, simple and efficient method for creation of nano sized structures by controlling parameters such as flux and sputtering temperature. Earlier works have shown that by controlling these parameters different pit morphology such as square pit on Cu (001) [135], hexagonal pits on Au (111) [133] and Pt (111) [136] and ripple structure on Ag (110) [137] can be obtained. Such patterns are expected to offer possibilities in technological applications [138]. Apart from many technological applications of ion bombardment, it is a common technique used to clean samples [133]. The low energy ($\sim 500 - 5000$ eV) ion beams are commonly used in surface science research for sample preparation [134].

2.6.1 Sputtering Yield

One of the common measurements of a sputtered sample is sputtering yield. Sputtering yield can be defined as the average number of atoms removed from a surface per incident particle. This expression is shown in equation below:

$$Y = \frac{\text{Average number of atoms removed from the surface}}{\text{Incident particle}} \quad (2.2)$$

In this equation, incident particles can be energetic ions, electrons, neutral atoms, molecules or larger clusters without considering the ones that maybe implanted and then re-emitted [139]. Sputtering yield measurements have received a lot of attention due to the importance in different areas such as target cleaning, near surface analysis of solids, fabrication of thin films and etc [140].

So far sputtering yield has been measured in many different systems and one of the widely used equations for this purpose is Bohdansky formula [141]. In 1994, C. Garacia-Rosales et al. [142] improved this equation to get a better fit to experimental results. This is shown as equation 2.3, where sputtering yield is a function of projectile energy assuming the angle between beam and sample is 90 degree.

$$Y = QS_n^{KrC}(\varepsilon) \left(1 - \left(\frac{E_{th}}{E_0}\right)^{\frac{2}{3}}\right) \left(1 - \frac{E_{th}}{E_0}\right)^2 \quad (2.3)$$

In this equation, E_0 is the projectile energy, E_{th} is the threshold energy when sputtering is zero, $S_n^{KrC}(\varepsilon)$ is the nuclear stopping cross section that provides the best fit to the Kr-C potential and ε is the reduced energy, which can be calculated independently using equation 2.4.

$$\varepsilon = E_0 \frac{M_2}{M_1 + M_2} \frac{a_L}{Z_1 Z_2 e^2} = \frac{E_0}{E_{TF}} \quad \text{with} \quad E_{TF} = \frac{Z_1 Z_2 e^2}{a_L} \frac{M_1 + M_2}{M_2} \quad (2.4)$$

where Z_1 is nuclear charge of projectile, M_1 is mass of the projectile, Z_2 is nuclear charge of target atom, M_2 is the mass of target atom, e is the electron charge and a_L is the Lindhard screening length that can be calculated as [142, 143]. :

$$a_L = \left(\frac{9\pi^2}{128}\right)^{1/3} a_B (Z_1^{2/3} + Z_2^{2/3})^{-1/2} \quad (2.5)$$

with a_B being the Bohr radius, which is approximately equal to 5.29×10^{-11} m.

The other unknown parameter in equation 2.3 is the $S_n^{KrC}(\varepsilon)$. This parameter can also be approximated by:

$$s_n^{KrC}(\varepsilon) = \frac{0.5 \ln(1 + 1.2288\varepsilon)}{\varepsilon + 0.1728\sqrt{\varepsilon} + 0.008\varepsilon^{0.1504}} \quad (2.6)$$

In equation 2.6, the threshold energy can be calculated based on the masses ratio:

$$E_{th} = \begin{cases} \frac{E_s}{\gamma(1-\gamma)} & \text{for } \frac{M_1}{M_2} < 0.2 \\ 8E_s\left(\frac{M_1}{M_2}\right)^{2/5} & \text{for } \frac{M_1}{M_2} > 0.2 \end{cases} \quad (2.7)$$

with E_s being the surface energy and γ the maximum energy transfer factor that can be estimated as $\gamma = 4M_{1x}M_2/(M_1 + M_2)^2$.

And finally, in equation 2.3, Q is used as the fitting parameter for the sputtering data [142, 143].

Here the angle has been assumed to be 90 degree. In studies where accurate measurements are required, it is also possible to add the angle dependence factor but for simplicity the simplest case has been considered.

As it has been shown, sputtering yield calculations are mainly done using theoretical methods. The number of experimental works, where morphology of surfaces has been examined right after the sputtering is limited. Especially for surfaces

covered with organic monolayers, our understanding of sputtering effects is insufficient. In chapter 6 of this work, morphological change of Au (111) surface with partial fullerene coverage, after few seconds of sputtering, has been investigated.

Chapter 3

Experimental Procedure

3.1 Scanning Tunnelling Microscope

The scanning tunnelling microscope (STM) was introduced by Binnig and Rohrer in 1982. Soon after, it was proven to be a powerful tool for studying surfaces and their properties [54]. The main idea behind the STM is simple; a very sharp metallic tip is brought close to a conductive sample in order to measure electron tunnelling. The value of tunnelling current measured with respect to the tip position can be used to produce a topographical image of the surface. This is known as the constant height mode. Scanning speed in this mode can be very high since the tip height does not need to be adjusted. However, a very flat sample is required to avoid any possibility of the tip crashing. The other mode of operation is constant current mode. In this case a feedback circuit is used to vary the tips height in order to keep the current constant. This mode is more commonly used, especially on new samples, to avoid damaging the tip. Movement of the tip is controlled by a piezo drive, made of piezo ceramic materials. So, by applying voltage (V_p), the ceramics can expand or contract resulting in the movement of tip accordingly [144–146].

As it was mentioned, measurements done by STM are dependent on the tunnelling current. In classical mechanic, a particle has to have enough energy to overcome a potential barrier. However, in quantum physics, there is always a possibility for particles to pass through the barrier. This is known as the tunnelling effect, which is based on wave properties of electrons. In this case electron wave function can be defined as $\psi(z)$, where z is the particles direction of propagation. The Schrödinger equation can then be used to predict the state of particles. For an electron with energy E that propagates along Z direction, the equation is described as below:

$$-\frac{\hbar^2}{2m} \frac{d^2}{dz^2} \psi(z) + U(z)\psi(z) = E\psi(z) \quad (3.1)$$

where the potential barriers height is “ $U(z)$ ”, $\hbar = \frac{h}{2\pi}$ with “ h ” being the Plank constant and “ m ” is the mass of electrons. The solution to this equation can be divided into two categories based on “ E ” being bigger or smaller than “ $U(z)$ ”. For classical regions, $E > U(z)$, the solutions can be defined as:

$$\psi(z) = \psi(0)e^{\pm ikz} \quad (3.2)$$

In equation 3.2, “ k ” is the wave vector that can be calculated using equation 3.3.

$$k = \frac{\sqrt{2m(E - U)}}{\hbar} \quad (3.3)$$

For classically forbidden regions, $E < U$, the solution is defined as:

$$\psi(z) = \psi(0)e^{\pm kz} \quad (3.4)$$

In this case the decay constant is calculated as follows:

$$k = \frac{\sqrt{2m(U - E)}}{\hbar} \quad (3.5)$$

The same tunnelling model can be applied to electrons that pass through the vacuum barrier between the tip and the sample. Once the tip is brought close enough to the sample the tunnelling would result in the fermi levels to be equalised as shown in figure 3.1A. By applying a potential difference (V_s) to the sample, its fermi level will be shifted by eV_s . Figure 3.1B shows an example where a negative voltage has been applied to the sample. In this case electrons in the filled states of the sample can tunnel to the empty states of the tip between E_f and $E_f - eV_s$. It is also possible to use a positive voltage to tunnel electrons from filled states of the tip to the empty states of the sample [144–147].

The value of tunnelling current is then not only dependent on the tip-sample separation but also the availability of their electronic states, which can be expressed as following:

$$I \propto \int_0^{eV} \rho_s(x, E_f + \varepsilon) d\varepsilon \quad (3.6)$$

In equation 3.6, $\rho_s(x, E_f)$ is the sample's local density of states (LDOS). For small voltages, this can be written as:

$$\rho_s(x, E_f) \propto \frac{1}{eV} \sum_{E_f - eV}^{E_f} |\psi(x)|^2 \quad (3.7)$$

Based on this equation and equation 3.4, tunnelling can be simplified as:

$$I \propto \exp(-2z\sqrt{\frac{2m}{\hbar^2}(\phi - \frac{eV}{2})}) \int_0^{eV} \rho_s(E_f + \varepsilon) d\varepsilon \quad (3.8)$$

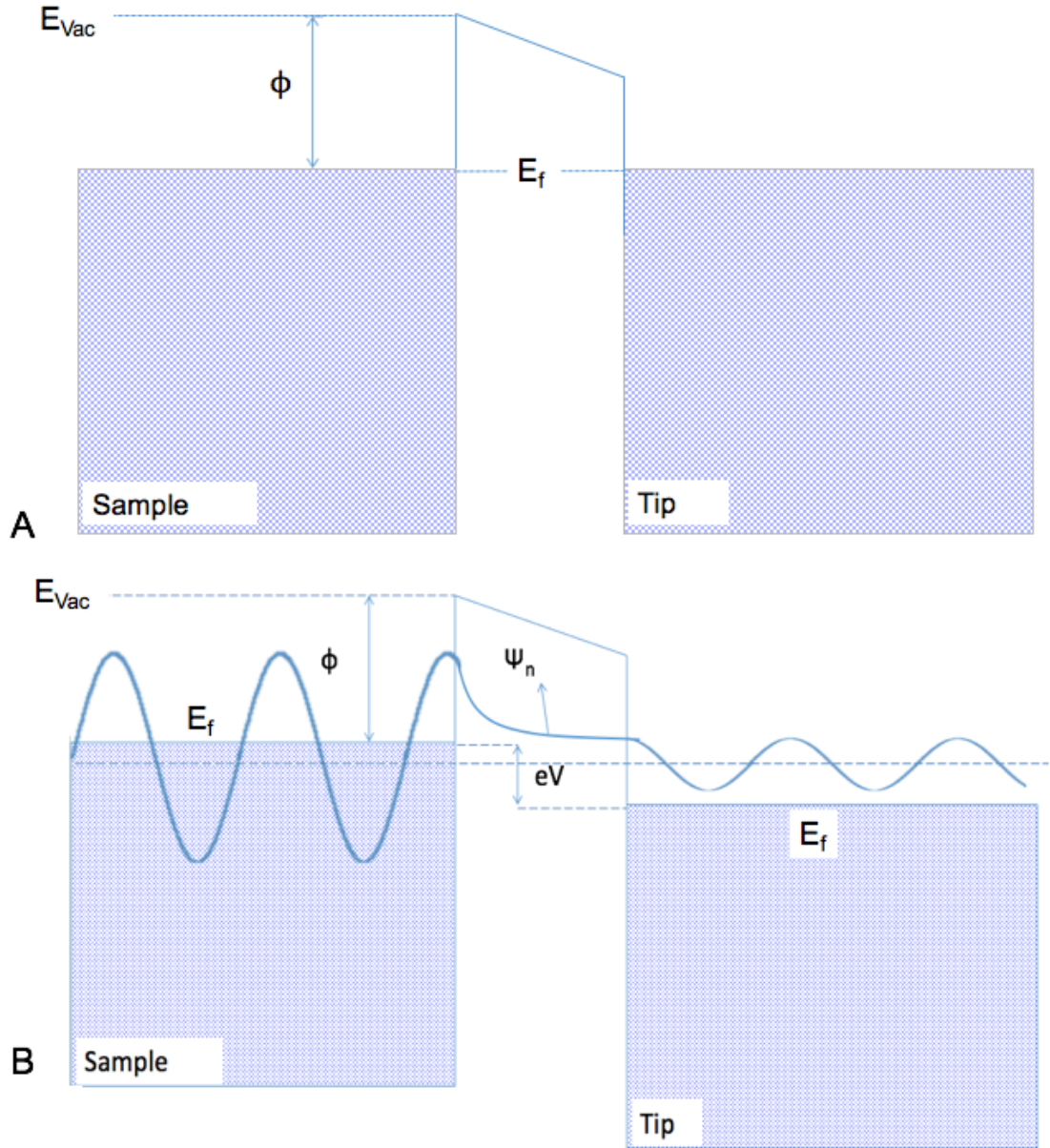


FIGURE 3.1: A model of one dimensional metal-vacuum-metal system is presented. A) The tip is brought close enough to the sample before applying voltage. B) In this example, a bias voltage (eV_s) has been applied that results in electrons between $(E_f - eV_s)$ and E_f states to tunnel from a sample to a tip.

In equation 3.8, “ ϕ ” is the sample work function and “ e ” is the electron charge. Based on this equation current is exponentially dependent on the tip-sample separation (z) [147]. So, if “ ϕ ” is about 5.5 eV, then 1 Å change in the separation would result in current varying by a factor of 10 [144–146]. This is especially helpful in obtaining atomic resolution with vertical resolution of sub angstrom [148].

As shown in figure 3.1, apart from the angstrom distance between the tip and the sample, current is also dependent on the availability of the electronic states. So STM images can be considered as superimposition of geometrical features of the surface as well as their electrical properties (the LDOS). Theoretical studies done have shown that apart from the electronic properties of the sample, tip states can also play an important role during scans. In order to explain this, different models were considered. One of the most successful models was suggested by Chen [149]. In this model p_z and d_{z^2} states of a d-band metallic tip were considered. The dangling bonds of these states at the apex atom of the tip follow and interact with the surface wave functions. This model provides a better surface corrugation compare to Fermi-level LDOS that makes it more suitable for modelling of atomic level scans.

My work presented here involves using an STM in ultra-high vacuum (UHV) conditions to ensure the work is done in a clean environment. In next sections the UHV and type of STM used are explained in more detail.

3.2 Ultra High Vacuum

In order to study the properties of a surface, it is important to make sure that the conditions remain constant over the whole period of the experiment. In another words, rate of reactive species arriving at the surface from surrounding gases should be low. The best condition for such experiments is in vacuum, where limited

amount of gas is confined in a given space. Pressures about or below 10^{-9} mbar are then called ultrahigh vacuum (UHV).

The rate of molecules arriving at the surface can be estimated as:

$$r = \frac{p}{\sqrt{2\pi k_B T}} \quad (3.9)$$

where “p” is the pressure, “ k_B ” is the Boltzmann constant and “T” is the temperature. Based on this, at pressure of about 10^{-9} mbar samples can remain clean for at least one hour. In order to obtain UHV conditions, the temperature of the system should be increased (between 100 to 300 degree C) to remove all gases (mostly water) adsorbed to chamber walls and then pumped using appropriate pumps. This procedure is known as baking [150].

For all of my experiments, an Omicron variable temperature (VT)-STM was used, that is formed of a single chamber. The chamber is pumped using an ion pump (IP) that runs at all times when chamber is at UHV condition, as well as a titanium sublimation pump (TSP) which is turned on every 8 hours for 1 minute. With the help of these pumps UHV condition can be maintained for a long time.

In order to reach UHV condition a rotary pump initially runs for about 30 minutes to reduce the pressure from atmosphere to better than 10^{-3} mbar. It also acts as a backing pump for the turbomolecular pump. So after reaching 10^{-3} mbar, the turbo pump is turned on to obtain a better vacuum [151]. Once pressure reached 10^{-6} mbar or lower, chamber is then covered with heat shields to prepare for the bake. Using a heater on the table, the temperature of the system is increased to 140 °C for 24 to 48 hours. After that the chamber temperature is left to reach about 80 °C before degassing the IP and TSP. Once successfully finished the degassing, a valve between turbo pump and the chamber can be closed, this allows rotary and turbo pumps to be vented, while chamber pressure is maintained by IP and TSP.

3.2.1 Variable Temperature STM

In order to obtain high quality scans, a vibrational isolated environment is required. In our lab the Omicron VT-STM chamber is placed on a floating stage that can help in isolating any possible vibrations. To avoid creation of noises, during scans only IP and TSP are used, this results in the base pressure of the chamber to be $\sim 5 \times 10^{-10}$ mbar. Furthermore, the STM head is located on a base plate suspended by four soft springs with resonance frequency of about 2 Hz. In order to intercept any vibration of the suspended system, eddy current damping is employed. For this purpose, the base plate is surrounded by a ring of copper plates. During scanning, the STM head is suspended that results in the copper plates being positioned between permanent magnets. For other purposes the stage can be locked using a push-pull motion (PPM) drive.

Other parts in this chamber includes fast entry lock (FEL) that is used to transfer samples or tips into the chamber. To do so, a sample or tip is placed on a designed fork. After sealing it, the FEL can be pumped down using separate turbo and rotary pumps. This helps to ensure the sample transfer does not have a major effect on the pressure of the chamber. Sample/tip is then placed in a carousel using wobble stick.

In order to degas the new sample/tip, it needs to be placed on a manipulator that allows for resistive heating up to about 1100 K. Apart from annealing, 360-degree rotation of the manipulator can be used to face the sample at different parts of the chamber. This is mainly used during Ar sputtering or some molecular depositions. A sketch of chamber with its main parts is shown in figure [3.2](#).

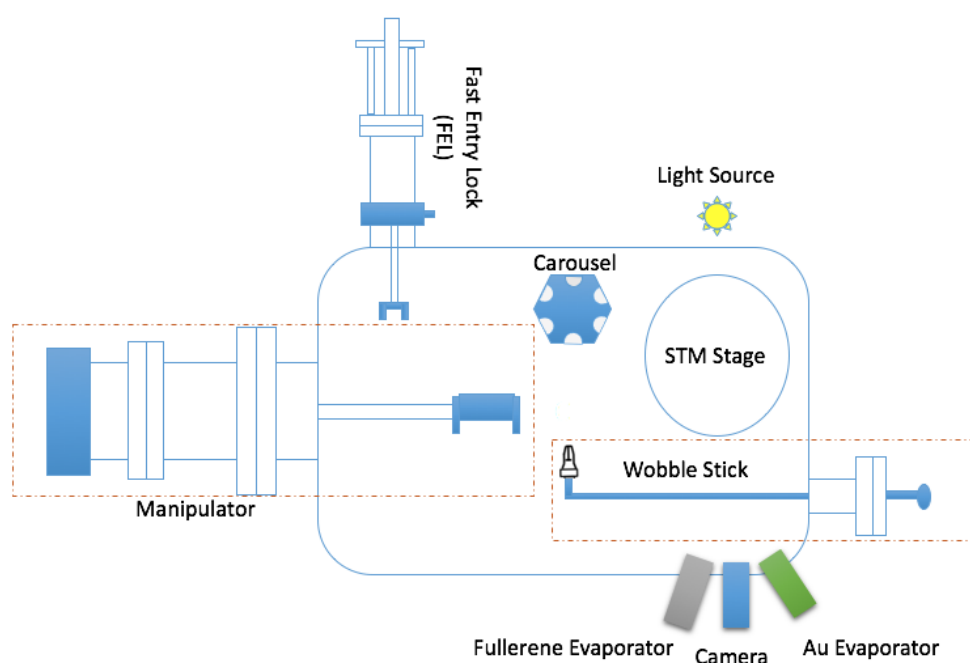


FIGURE 3.2: Sketch of the Omicron VT-STM, showing its main parts, is presented. This includes the STM stage position, carousel that allows storage of up to twelve samples and tips, manipulator that has heating stage and ability to rotate to desired directions and a wobble stick that can be used to move samples between these positions. FEL is another part of the chamber that allows transferring sample/tip in or out of the chamber.

The scanner used in this system is a single tube with z-range of about $1.5 \mu\text{m}$ and maximum scan range of about $12 \mu\text{m} \times 12 \mu\text{m}$. Other applications of this chamber includes heating and cooling systems that allows users to scan the sample at different temperatures from 25 K to 1500 K. In order to reduce the time required for different cycles of heating and cooling, the microscope stage's temperature is kept about room temperature, while the sample is heated or cooled separately.

For low temperature investigations liquid nitrogen (LN_2) bath cryostat is added to the STM. This allows performing experiments between 100 K and room temperature. As shown in figure 3.3, a gas flow control block is used with a rotary pump to control the flow of the liquid nitrogen into the system. For thermal coupling, a clamping block is placed on top of the sample holder that cools down the sample

and tip while the rest of chamber is at RT. In order to adjust the sample temperature, a heater element together with a silicon diode is fitted to the heat exchanger that can be controlled using Lakeshore temperature controller. A diagram of this set-up is shown in figure 3.3.

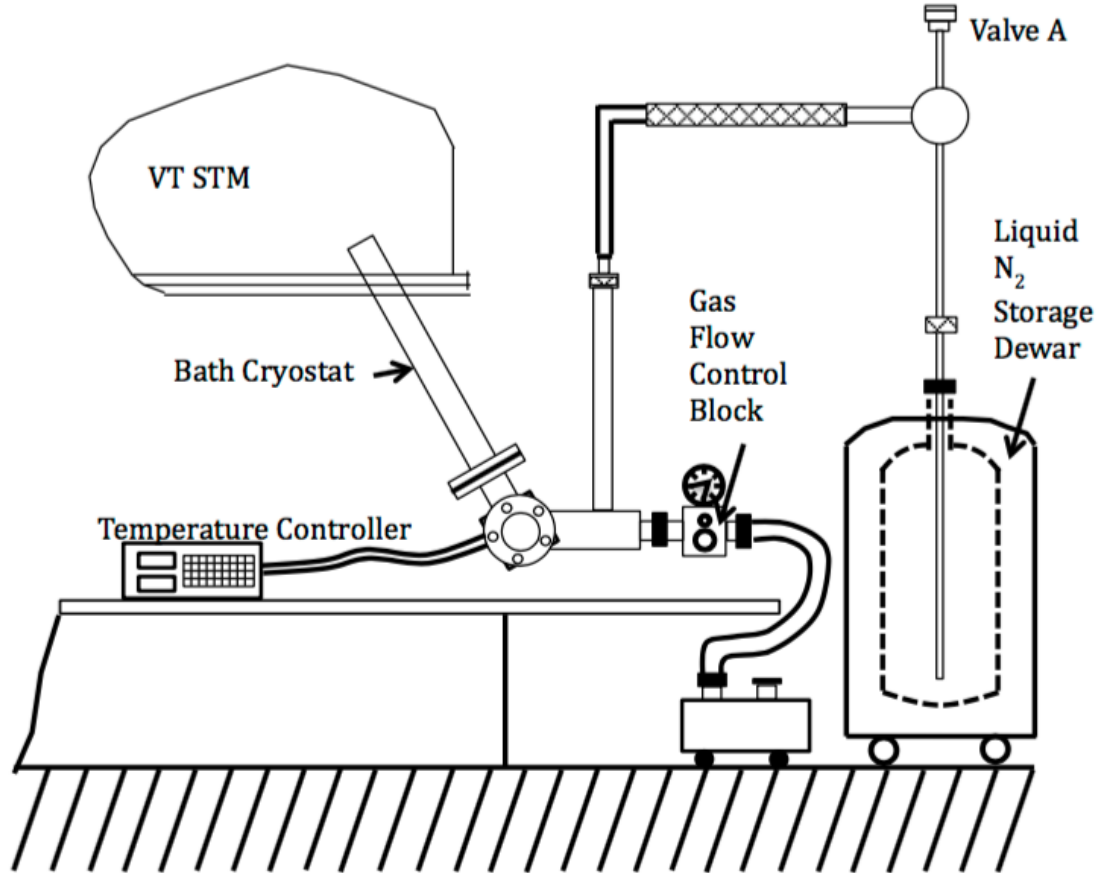


FIGURE 3.3: Schematic diagram of low temperature set up.

Achieving temperatures lower than 100 K requires liquid helium. For experimental results presented here only liquid nitrogen was used. In order to increase the temperature of sample above RT, there are two methods of direct and resistive heating. In both cases contact brushes on STM stage are used to apply DC current. For direct heating, a sample with high resistance is required that allows maximum temperature of about 1500 K. For resistive heating, current passes through a PBN plate (pyrolytic boron nitride) that is placed inside the sample holder. This method

can heat any sample up to 900 K. It is also worth mentioning that the temperature gradient between the tip and the sample can result in a thermal drift during scanning. This can be fixed after manually adjusting the area of interest for about 30 min.

3.3 Tip Etching

In order to have good resolution scans, size, shape and cleanness of STM tip plays an important role [152]. Failure in preparation of a good tip can result in problems such as formation of several mini tips. If the tip that electrons tunnel through changes, surface features can appear in the scans more than once. Contamination and oxidation of the tip can also influence the tunnelling junction and cause irregularities in the image [153]. So preparing the tip is a very important step.

There are mainly two types of tips used for scanning, tungsten (W) and Platinum/Iridium (Pt/Ir). Pt/Ir tips are commonly used for scanning flat surfaces in atmosphere. To do so, a small piece of a wire is placed inside a tip holder and then cut with a scissors to get a sharp end [153]. For experiments done in UHV conditions, tungsten tip is more commonly used due to high melting point and strength of it. In order to prepare the tip, drop-off technique by electrochemical etching is used [152]. In our lab, we use 2 moles (M) of sodium hydroxide (NaOH) solution. This is produced by dissolving 40 grams of NaOH pellets in 500 mL of distilled water. The set up used for etching is shown in figure 3.4.

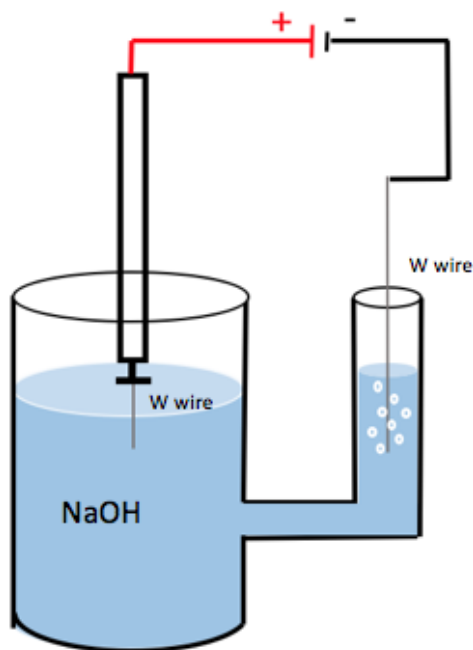
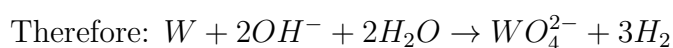
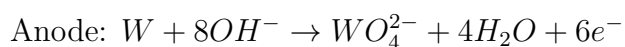
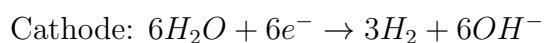


FIGURE 3.4: : Set up used to electrochemically etch tips. Beakers are filled with 2 M of NaOH solution. In this set up, the tip acts as an anode, while the other piece of W is used as cathode with potential difference of 10 V being applied across it.

In this set up, a tip is placed inside the larger beaker, which works as an anode and another piece of tungsten wire is placed in the smaller beaker as cathode. Then using a DC power supply, 10 V potential difference is applied across it. This results in the following reactions at the air - solution interface [153].



An advantage of having separate beakers is that hydrogen bubbles, formed on the cathode during etching, will not disturb the meniscus around the tip. In this method etching will start at the air-solution interface. As the wire dissolves and its

thickness decreases, resistance increases, as a result current will also increase until the tip breaks. The power supply will then shut down automatically to prevent further etching of the tip [153]. It is important to have the dropping part as small as possible to avoid damaging the wire when it breaks [152]. During etching, the system should be isolated from any vibrations that can cause irregular shapes of the tip. After that, it will then be cleaned by dipping it in distilled water and ethanol few times. Finally, the tip can be degassed inside the UHV chamber for 1 hour at about 350 K to remove oxide layer and adsorbed contaminants.

If the image quality was not good; it is also possible to improve the tip quality during scans. A possible solution is to increase the bias voltage for few scans in order to increase the interaction between the tip and sample. The voltage is then reduced to the normal value of ± 2.5 V. Scanning current can also be increased for few seconds, this will reduce the distance between the tip - sample and may even result in a slight crash that can remove adsorbent on the tip. STS with voltage ramp from -2 V to +2 V, can also be used to clean the tip and get better images. Ideally, these processing methods should be done on a clean Au (111) surface to avoid molecules transferring to the tip.

3.4 C_{60}/C_{70} and Au Deposition

Deposition of fullerene molecules is done by a home-made Knudsen cell. To do so, a DC voltage is applied to C_{60}/C_{70} powder (from MER corporation with 99.99 % purity) placed inside a tantalum pocket. Temperature of the pocket is measured using a K-type thermocouple that has been welded on its side. A sketch of the evaporator is shown in figure 3.5.

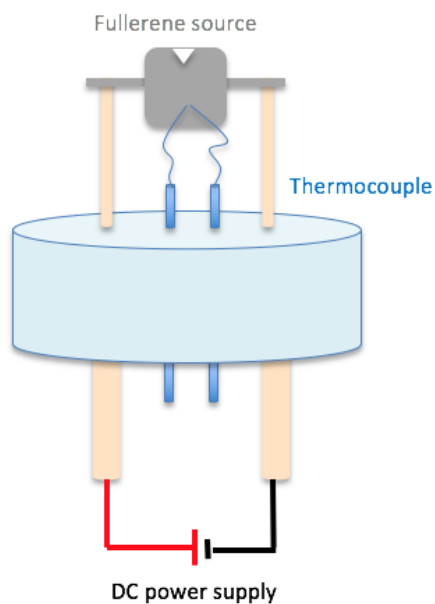


FIGURE 3.5: A model for the fullerene evaporator used.

Before deposition, the powder is degassed by increasing the temperature to 470 K for 5 min. This is then followed by further increase in temperature to about 680 K for C_{60} and 600 K for C_{70} molecules deposition, with chamber pressure being about 10^{-8} mbar. From counting fullerene molecules in different scan areas, deposition rate of C_{60} and C_{70} molecules was measured to be about 0.04 ML/min and 0.02 ML/min respectively.

Another Knudsen cell (high temperature effusion cell from Crea Tech) is used for gold atom deposition. In this case a gold wire (from Goodfellow with 99.99 % purity) is placed inside an alumina crucible with a control unit to set the temperature. During deposition the temperature of the Au source is increased to 1100 °C. Once temperature reached the required condition, a shutter, placed in front of the cell, is manually opened to start the deposition. At this temperature, deposition rate of about 0.01 ML per minute was estimated with base pressure

of 10^{-9} mbar. This value was estimated using “Image SXM 198” program. Area of individual islands was measured and added to calculate the percentage area covered in each scan. The average value of surface coverage was calculated for a given deposition time that allows for estimation of coverage, or deposition rate, per unit time.

3.5 Sample Preparation

Au (111) samples are commonly prepared by evaporating Au atoms on substrates such as mica or HOPG. Preparing Au samples by evaporation can help to get larger flat terraces in comparison to single crystals.

In our lab, production of Au samples starts by cleaving a $1.0\text{ cm} \times 0.5\text{ cm}$ HOPG sample with adhesive tapes. This helps to get a fresh, clean and flat surface. The sample is then transferred in to an Edwards evaporator, with $1.5\text{ cm} - 2\text{ cm}$ Au wire (99.99% pure from Goodfellow) being placed inside a molybdenum boat. Chamber is then pumped overnight using a turbo molecular pump to reduce the vacuum pressure to 1.0×10^{-7} mbar. Before and during deposition, the sample is annealed to degas as well as provide enough energy for incoming Au atoms to form a flatter surface. This is done by resistively heating the HOPG substrate using 3.2 A current to obtain temperature of $\sim 300^\circ\text{C}$. At the same time, the Au wire is degassed by passing 30 A through the boat for 20 min. The current is then increased to 35 A in order to melt the wire and degas it for another 5 minutes. Meanwhile, to avoid contamination sample and Au source are separated by a shutter.

Evaporation start by increasing the current to 38 A and opening the shutter. During evaporation, growth rate is measured using a quartz crystal oscillator. To obtain sample with wide flat terraces the deposition rate is kept at 0.2 nm/min ,

with base pressure of the chamber being 1.0×10^{-6} mbar. Once deposition is done, shutter is first closed and then current used to evaporate Au is set to zero. Sample is further annealed for another 15 minutes to improve the flatness of the surface. After cooling down, evaporator is vented and the sample is placed to an Omicron resistive heating sample holder, which is then transferred into the VT-STM chamber. It is further treated with Ar ion sputtering and annealing cycles. The sputtering is done with 1 keV argon ion beam and target current of $10 \mu\text{A}$ for 7 min to remove the top layer. Sample is then annealed for 1 hour at 1000 K to recover and release impurities in the bulk. This cycle is repeated until a clean reconstructed gold surface is obtained [154].

Chapter 4

Size-Control of Magic Clusters

4.1 Introduction

In chapter 2, the self-assembly and production of C_{60} -Au magic clusters were explained. One of the features that made these clusters interesting was the absence of any directional or selective bindings. In this chapter, more details on clusters and their size distributions are provided. Results obtained from variation of Au atoms, fullerene molecules and how it effects range of clusters formed are presented. So far the production of clusters with C_{60} molecules have been examined. Here C_{60} has been replaced with C_{70} molecules to check if the ellipsoidal shape of them can change structures observed.

Apart from the amount of atoms and molecules available, temperature is also known to be an effective parameter. Therefore, in later parts of this chapter, the effect of temperature on the size distribution of clusters is introduced. Finally, the result of co-depositing molecules and atoms at low temperature is explained.

4.2 Au Coverage Dependence of Cluster Size

It is known that at room temperature Au atoms can diffuse across the Au (111) terraces (few hundreds of nm) and reside along step edges without being affected by the reconstruction patterns. In order to limit their thermal energy and encourage them to form small islands at elbow sites the sample temperature should be reduced to ~ 115 K. Figure 4.1 shows formation of Au islands after deposition of atoms at 120 K. In this figure, STM images of two different Au coverages are presented. As mentioned before, the deposition rate of Au atoms was estimated to be ~ 0.013 ML/min at 1100 °C. Based on this value the expected coverage in figure 4.1A, after 390 s of deposition, is about 0.085 ML, and in figure 4.1B, after 50 s, is 0.011 ML. However, coverages measured for these images, using the method explained in experimental procedure chapter, are 0.09 ML and 0.03 ML respectively. This difference in estimated and calculated values for low coverages is a result of tip convolution. Structures that have radius (R) larger than tips (r), $r < R$, can be resolved by the tunnelling tip to obtain a clear image. However, if the object is smaller, $r > R$, the image obtained will be smeared out [155, 156]. Due to the limitation in the resolution, values obtained are more accurate at higher coverages. In order to estimate the error measured on islands area, the following equation was employed.

$$\frac{\sum_{i=1}^n (R_{a1})^2}{\sum_{i=1}^n (R_{a2})^2} = \frac{\sum_{i=1}^n (R_{m1} - c)^2}{\sum_{i=1}^n (R_{m2} - c)^2} \quad (4.1)$$

In equation 4.1, “ R_{a1} ” and “ R_{a2} ” are true radius at two different coverages, “ R_{m1} ” and “ R_{m2} ” are measured radii for each coverage accordingly and “ c ” is the error on each measurement. By assuming a circular shape for all islands observed, it is possible to convert the area measured to “ R^2 ”. If the experiments are performed under constant conditions, then the ratio of deposition time should equal to the ratio of actual areas covered. Using this information and equation 4.1, the value

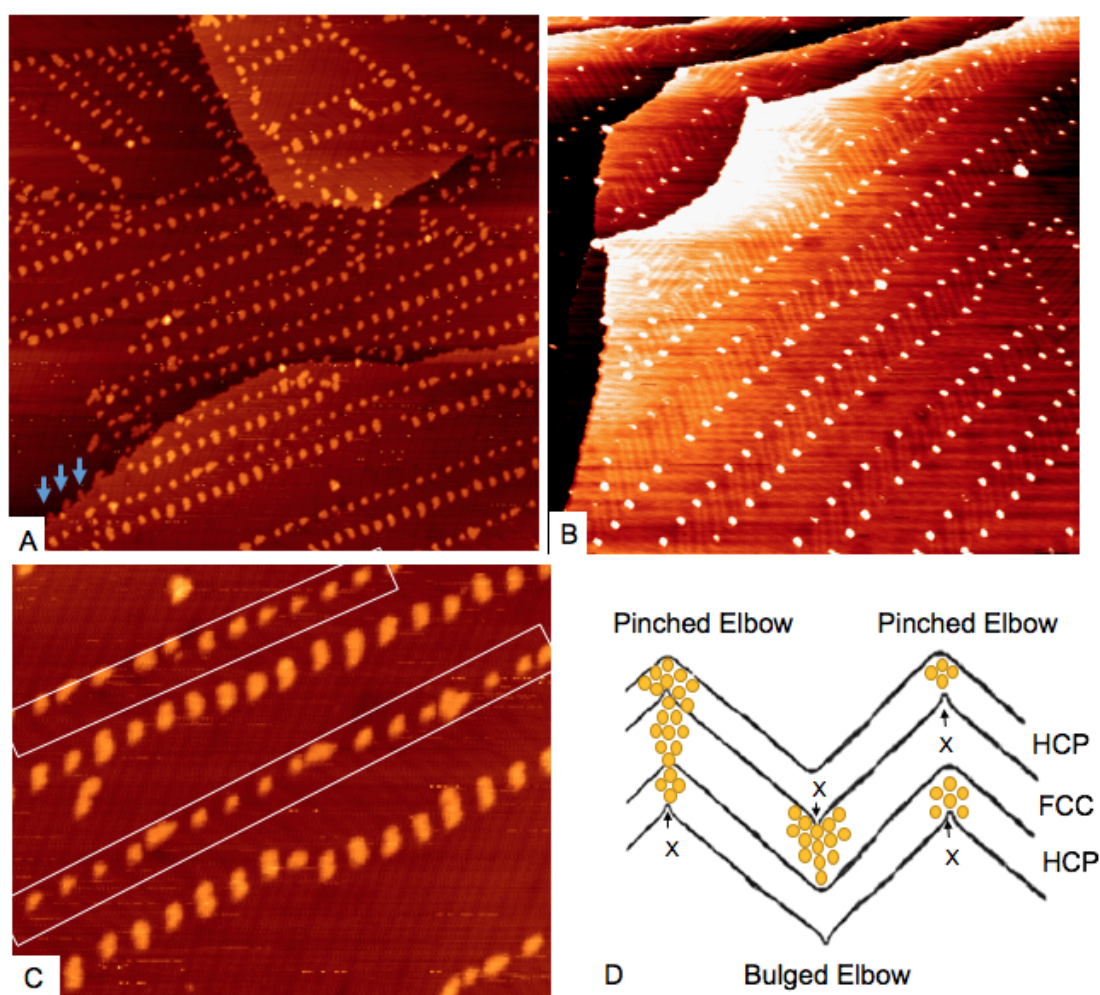


FIGURE 4.1: Different coverages of gold atoms were deposited on Au (111) surface at 115 K. A) At high coverage of 0.09 ML, islands are formed on elbow sites as well as being attached to the step edges. 254 nm \times 254 nm, $V = -1.71$ V, $I = 0.05$ nA. B) For lower coverages, 0.01 ML, smaller islands were observed only on elbow sites. 181.4 nm \times 181.4 nm, $V = -1.89$ V, $I = 0.05$ nA. C) A zoomed in scan of Au on Au (111) showing different size of Au islands on bulged and pinched elbows. Islands on pinched elbows are highlighted by white boxes. D) A schematic model of Au islands position with respect to the reconstruction pattern. X-elbows in this figure are marked by “x”.

of “c” was estimated to be ~ 0.6 nm. The code used in the Matlab is included in Appendix A. So, for the rest of this report the error has been removed from the areas measured.

The other observation made was the difference in size of Au islands depending on the elbow types. In figure 4.1C, a higher magnification image of the surface with

0.09 ML coverage is presented. In this image the difference in sizes of islands is shown more clearly, with smaller Au islands on pinched elbows being highlighted by the white boxes. The average size of Au islands, for 0.09 ML, was measured as $7.3 \pm 4.3 \text{ nm}^2$ on bulged, $4.3 \pm 3.3 \text{ nm}^2$ on pinched elbows and $6.3 \pm 4.1 \text{ nm}^2$ on step edges with their size distributions being shown in figure 4.2. The errors on these values correspond to the standard deviations on values measured.

As shown in the model 4.1D, growth of islands start from X-type of elbows located in fcc areas for bulged and hcp regions for pinched elbows. Based on values measured, the ratio of island sizes on bulged/pinched elbows is about 1.7 that is close to the area of fcc/hcp at these portions. So it can be concluded that any atom landed in the fcc area joins islands on the bulged elbows and atoms on the hcp sections are distributed between pinched elbows. Then broader growth area available is one of the reasons for observing larger islands on bulged elbows. Apart from elbow sites, finger-like islands were observed at some parts of step edges. Example of them are highlighted in figure 4.1A by blue arrows. These islands are mainly observed at areas where the density of elbows is low. Reduction of active sites results in more gold atoms to reach step edges and form islands.

After confirming and measuring the range of Au islands observed, the sample temperature was increased to 150 K for deposition of fullerenes. This slight increase in temperature allows molecules to move around the existing Au islands and encapsulate them rather than grouping only on one side of islands. In order to examine the effect of Au coverage, different amounts were deposited on the surface while the ratio of C_{60} to Au coverage was kept constant with fullerene being approximately two times higher than gold.

The sample was then slowly annealed to form magic clusters at room temperature. 300 thermodynamically stable clusters were then imaged and counted at room temperature. Figure 4.3 shows results obtained from three different coverages.

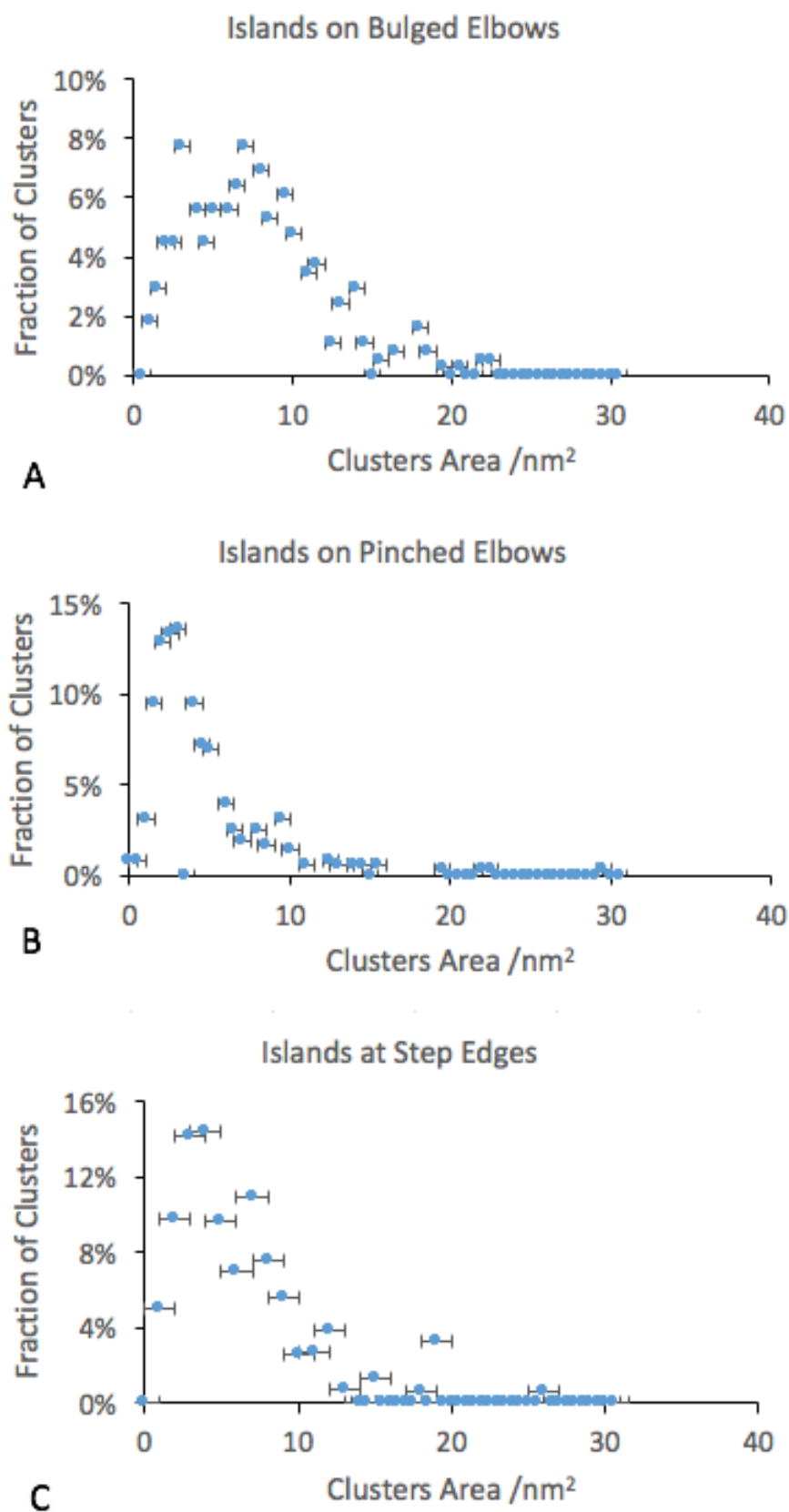


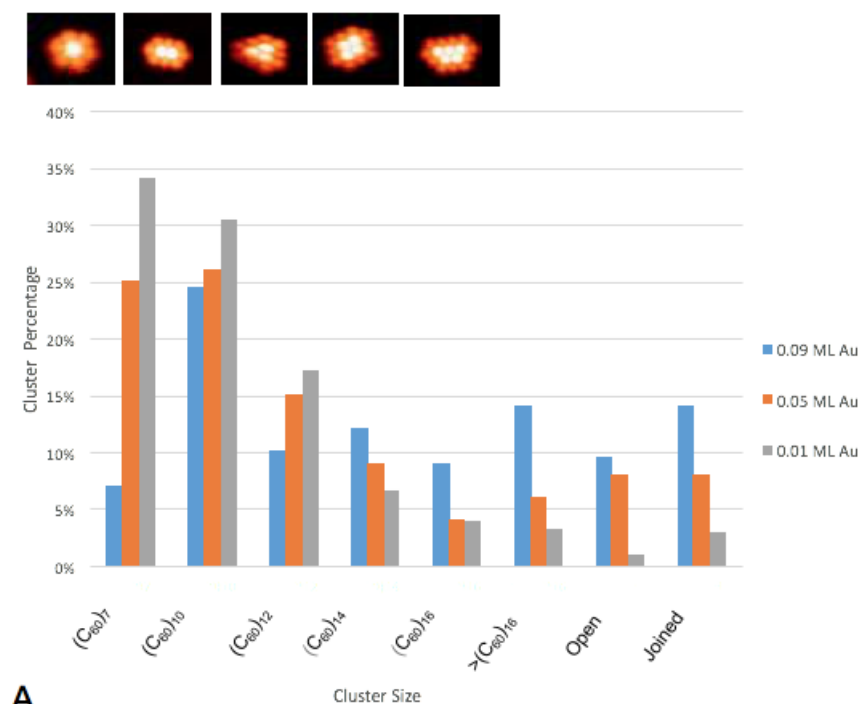
FIGURE 4.2: Size distribution of islands on bulged elbows (A), pinched elbows (B) and step edges (C). The error bars are due to the rounding of the island areas.

As it can be seen from histogram 4.3, increasing the Au coverage results in wider range of structures being obtained. At a low coverage of 0.01 ML, the majority of clusters formed were $(C_{60})_7$ (34 %) and $(C_{60})_{10}$ (30 %). In this case, as the size of clusters increases, percentage of structures observed corresponding to that size, decreases. But this trend changes at higher Au coverages, especially for 0.09 ML. In this case a sharp peak at $(C_{60})_{10}$ is observed that indicate the most common (25 %) size of clusters observed. As coverage increases the area of Au islands formed at elbow sites grows, therefore, larger clusters with higher variation in range of stable structures is expected. Figure 4.3B, shows an example of scan areas where the number of $(C_{60})_{10}$ clusters, highlighted by a blue circle, is much higher than other structures. In this image $(C_{60})_7$ is also marked with a yellow circle. Other clusters highlighted are joined clusters, marked as “J”, and open structures, “O”. These clusters will be explained in more detail in later parts of this chapter.

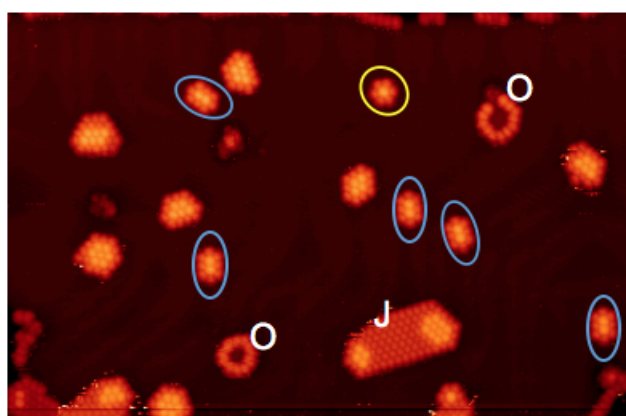
Based on results obtained it can be concluded that the Au coverage plays a critical role in the range and type of structures observed. However, controlling the size of clusters precisely is not achievable yet. One of the reasons is the movement of atoms and molecules as a result of the increase in temperature. Free molecules and atoms can be captured by other clusters to form larger structures. Therefore, temperature can play a critical role in range of clusters obtained which will be explained in more detail in next section.

4.3 Temperature Dependence of Cluster Size

One of our goals was to produce clusters with the majority having a certain size. To do so and achieve high coverages of $(C_{60})_7$ clusters, 50 s (0.017 ML), Au was deposited on the surface at 115 K. This was then followed by deposition of about 0.06 ML C_{60} at 150 K and annealing the sample slowly up to 280 K. Scans shown in figure 4.4 are examples of surfaces obtained. As it can be seen, high number



A



B

FIGURE 4.3: A) Histogram of cluster sizes with 300 structures counted. The colours correspond to different Au coverages, grey is 0.01 ML, orange is 0.05 ML and blue is 0.09 ML. C_{60} coverage was kept at about two times of the Au coverage in all experiments. Image of each cluster is shown above the graph. B) Scan obtained at RT with 0.09 ML Au and 0.21 ML C_{60} coverages, that shows higher number of $(C_{60})_{10}$ clusters, marked as blue, in comparison to the $(C_{60})_7$, yellow circle. Clusters marked with “O” are the open structures and “J” corresponds to the joined clusters. 90 nm \times 90 nm, V = -1.61 V, I = 0.05 nA.

of $(C_{60})_7$ clusters have formed at ~ 280 K. Based on the model suggested for magic clusters, figure 2.27, Au coverage of ~ 0.028 ML is required for stability of structures in figure 4.4A. This value is higher than the estimated coverage on this surface (0.017 ML). However, if we consider the minimum Au required to have a C_{60} molecule sitting on top of an island (7 Au atoms), then the coverage required is ~ 0.012 ML. This indicates the amount deposited was just enough to form $(C_{60})_7$ clusters that are not thermodynamically stable. Then, it is not a surprise that once the sample reaches room temperature, most of structures open up and form C_{60} islands at the step edges. In order to minimise this effect it is possible to limit the energy of clusters at temperatures below RT (~ 260 K).

Figure 4.4C, is another example of a surface with similar Au (0.017 ML) and C_{60} (0.07 ML) coverages at 261 K. Pattern observed is in agreement with other measurements presented in this figure. Areas marked as “E”, in this scan, and fullerene islands at the step edges are products of excess C_{60} molecules that have been released from unstable structures. The other noticeable point is the formation of clusters mainly on bulged elbows. This is not a surprise since the size of Au islands on pinched elbows are smaller compared to that on bulged elbows. Unstable structures formed at pinched elbows tend to open up at much lower temperatures, ~ 200 K. As previously mentioned $(C_{60})_7$ clusters observed are also not stable at room temperature. Figure 4.5 shows an image of the surface after being at room temperature for 12 hours.

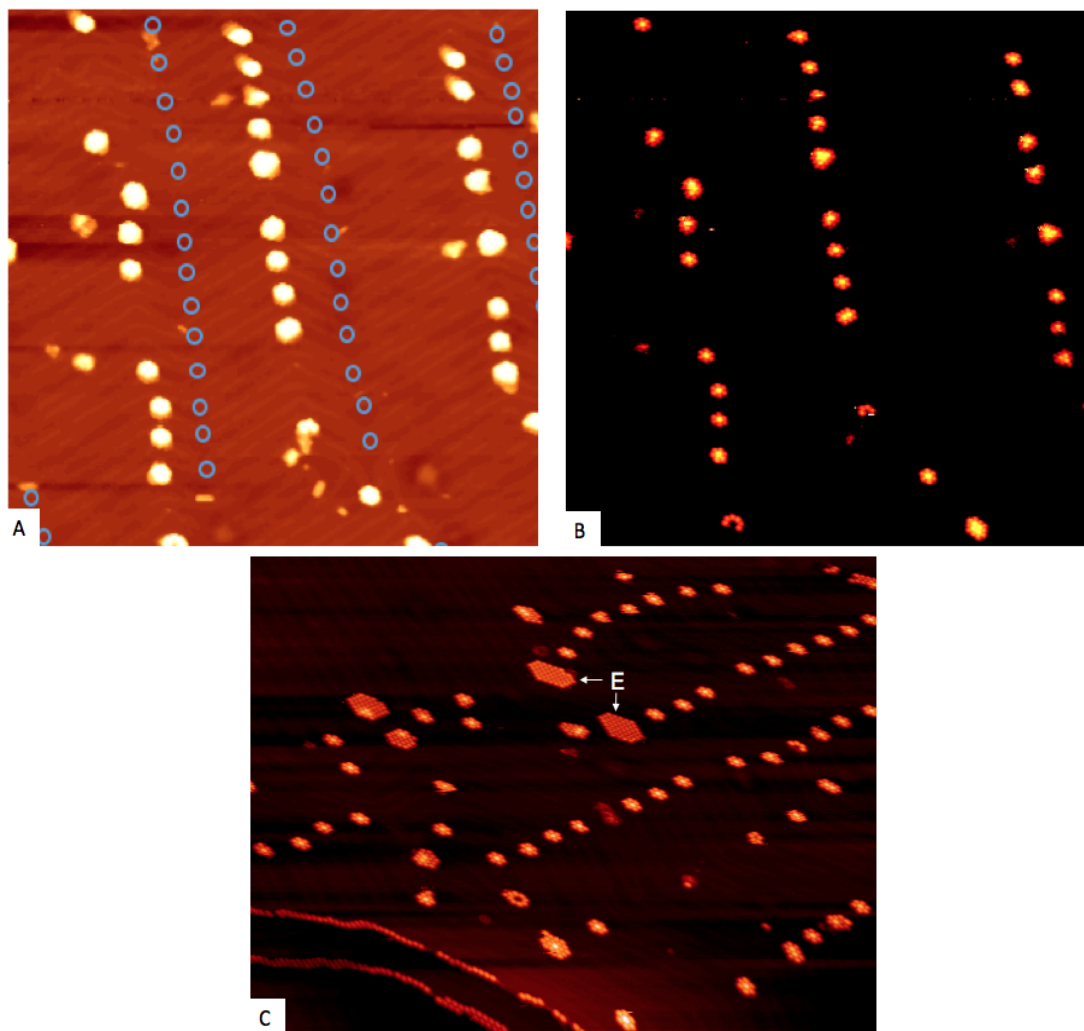


FIGURE 4.4: Scan obtained at 283 K after deposition of 0.017 ML Au and 0.06 ML of C_{60} molecules. From images it is clear that majority of clusters (63 %) are $(C_{60})_7$. The contrast has been adjusted so that reconstruction (A) and clusters (B) are easily visible. The blue circles in A, highlights pinched elbows which are empty of clusters. 100 nm \times 100 nm, $V = -1.54$ V, $I = 0.05$ nA. C) A scan obtained at 261 K with 0.017 ML Au and 0.07 ML of C_{60} coverage. On this surface about 83 % of clusters are $(C_{60})_7$ with majority being on bulged elbow. "E" highlights the islands formed from extra C_{60} molecules released by opening of clusters on pinched elbow. 130.26 \times 94.64 nm; $V = -2.05$ V, $I = 0.05$ nA.

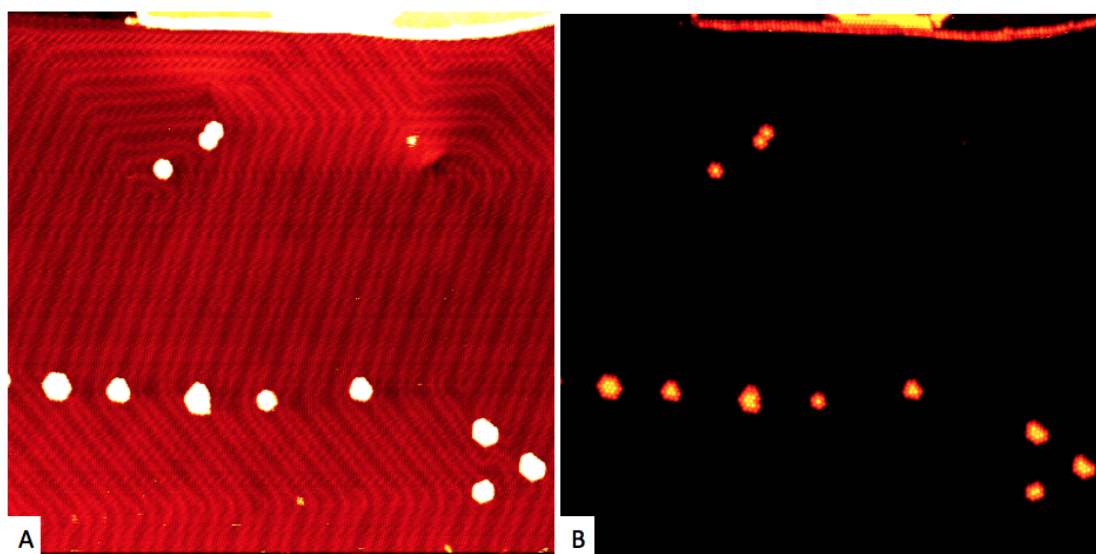


FIGURE 4.5: Scan obtained at RT with 0.017 ML Au and 0.07 ML of C_{60} coverage. Two different contrasts are used to make reconstruction (A) and clusters (B) more clear. In this scan majority of the $(C_{60})_7$ clusters have disappeared and larger structures are observed on pinched elbows. 127.25 nm \times 127.25 nm, $V = -1.97$ V, $I = 0.05$ nA.

At this point majority of $(C_{60})_7$ clusters have disappeared. Instead larger structures that are not necessary on the bulged elbows were observed. Figure 4.5 shows an example of such areas, where most of clusters are located on pinched elbows. It should be noted that as temperature increases atoms and molecules in clusters gain more kinetic energy. Smaller structures that have not reached the thermodynamically stable forms will then open up to join other existing molecules/atoms on the surface and create larger stable clusters. New structures formed can move to pinched elbows where the fcc area available is larger.

Temperature is known to have a direct effect on kinetic energy of molecules and atoms on the surface. So by lowering the temperature it is possible to kinetically control the range of structures formed. In this case, atoms and molecules are trapped to form magic clusters due to their lower mobility. Structures observed require much longer duration or higher temperature to overcome the kinetic trap and reach thermodynamically stable forms in an irreversible process [157].

4.4 Fullerene Dependence of Cluster Size

4.4.1 Formation of Clusters with C_{60} Molecules

After the Au coverage and sample temperature, C_{60} coverage was the next parameter examined. To prepare samples, Au atoms were deposited at 115 K on a clean Au (111) sample for 390 s (0.09 ML). This was then followed by deposition of different amounts of fullerene molecules at 150 K. Two scans, presented in figure 4.6, show results obtained at RT with 0.17 ML (4.6A) and 0.21 ML (4.6B) of C_{60} coverage.

One of the first observations that can be made based on figure 4.6 is the reduction in number of ring structures with higher coverage of fullerene molecules. At these coverages there are enough fullerene molecules available to form closed and stable clusters. Another observation made was the increase in number of joined structures due to the larger fullerene islands formed at LT. Example of such clusters are highlighted in the figure 4.6 as “J” and “O” corresponding to joined and open clusters respectively.

In order to have a better statistical understanding of the effect of C_{60} coverage on size of clusters, 300 structures were counted. Results obtained are displayed in figure 4.7.

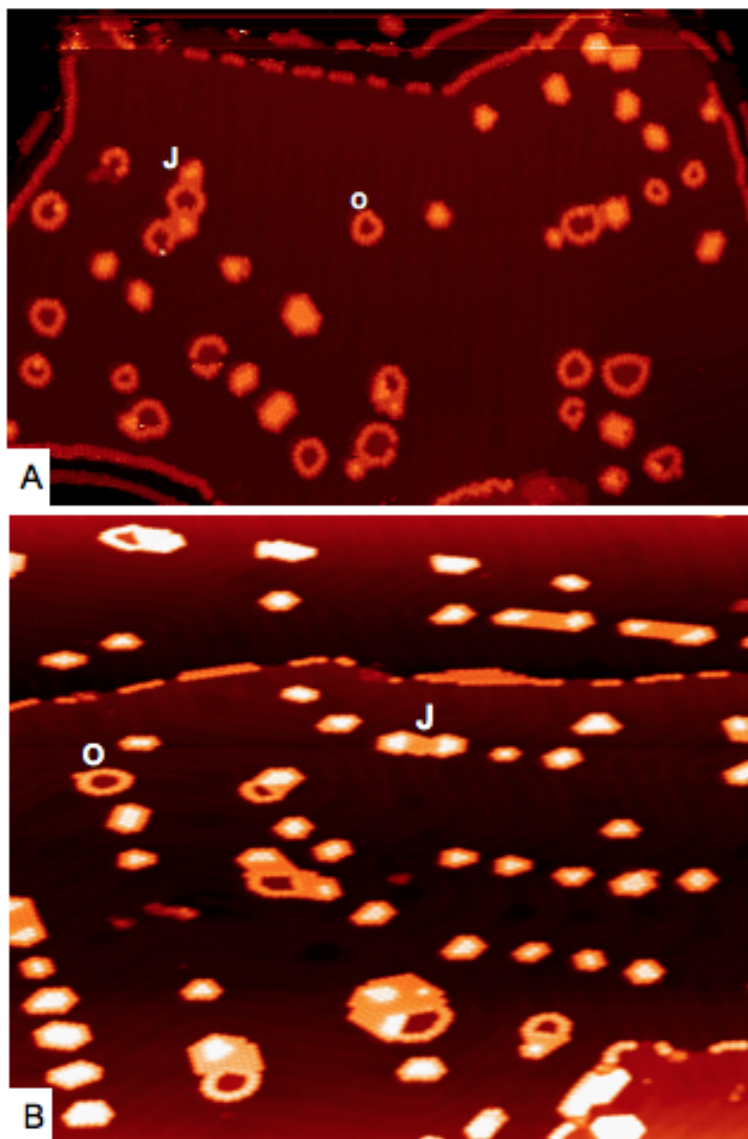


FIGURE 4.6: Scans obtained from surfaces at room temperature. In both cases the Au coverage has been kept constant at 0.09 ML, but the amount of C_{60} deposited has increased from 0.17 ML, in figure A, to 0.21 ML in scan B. As a result, formation of larger clusters as well as a decrease in the number of ring structures has been observed. In these scans “J” stands for joined and “O” for open structures. A) 141 nm \times 81.8 nm, $V = -1.85$ V, $I = 0.05$ nA. B) 90 nm \times 90 nm, $V = -1.61$ V, $I = 0.05$ nA.

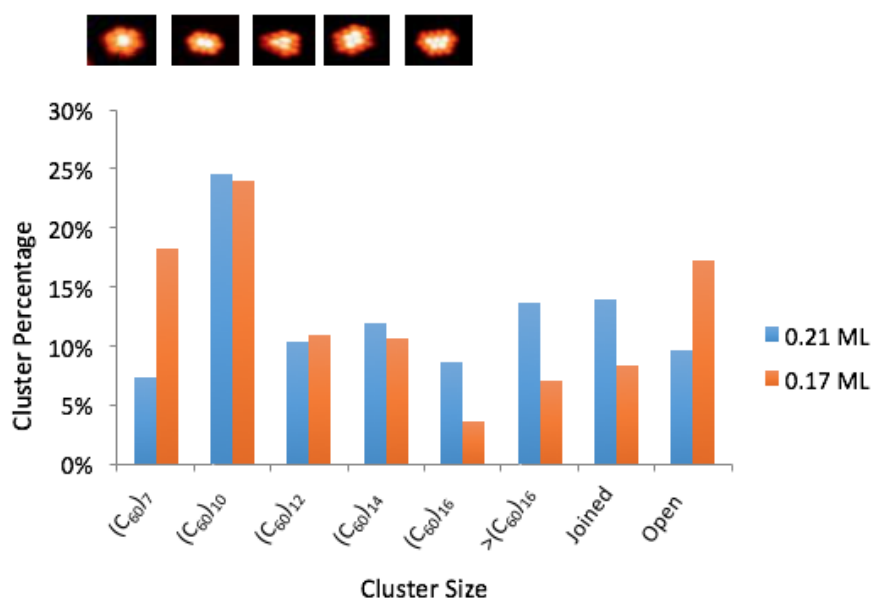


FIGURE 4.7: Size distribution of clusters with constant Au (0.09 ML) and different C_{60} coverages (0.21 ML and 0.17 ML). Results presented has shown that lack of fullerene molecules available can result in the formation of more open structures. Once the coverage is higher, probability of observing joined structures increases. Slight changes in number of 7 C_{60} clusters can be due to break down of larger structures to smaller ones in order to reach the thermodynamically stable form.

Another point noted is the slight decrease in the number of smallest stable structure, $(C_{60})_7-(Au)_{19}$. This decrease can be a result of larger structures breaking down to form smaller thermodynamically stable clusters. In another words, when there is not enough C_{60} molecules available, clusters that are not thermodynamically stable, can lose their Au atoms or/and C_{60} molecules in order to reach smaller stable forms.

Based on these observations, it can be summarised that deposition of too many C_{60} molecules would result in the molecular trapping by stable structures and formation of joined clusters. Whilst lack of C_{60} molecules, with respect to the size of Au islands, can result in formation of open (ring) structures. Therefore, the percentage of open and joined clusters can act as a measure to check if there are enough fullerene molecules available on the surface or not.

4.4.2 Formation of Clusters with C_{70} Molecules

For next part of the experiment C_{70} molecules were used to check if the rugby ball shape of it can have any effect on the clusters formed. Samples have been prepared using the same method as explained before, with Au being deposited at 110 K and C_{70} molecules at 150 K. This was then followed by slowly annealing it to room temperature. Figure 4.8, shows an example of thermodynamically stable structures observed.

As shown in this figure, all stable clusters formed with C_{60} are also observed with C_{70} molecules. Figure 4.8B, shows a zoomed-in image of the part highlighted by the blue square with a height profile along the white line. The apparent height of fullerene molecules around step edges has been measured to be ~ 0.9 nm. This value indicates that molecules are “standing up” with their long axis perpendicular to the surface. The graph also shows the central molecules to be ~ 0.25 nm taller than the surrounding ones; this suggests that the central molecule is on a Au island with the same orientation, standing up. Then, the diameter of molecules parallel to the surface is almost the same as C_{60} which allows us to apply the $(C_{60})_m-(Au)_n$ model for these clusters as well. This similarity can be confirmed using histogram 4.9, that shows the comparison of clusters formed at room temperature with same coverage of Au (0.09 ML) and fullerene molecules (0.2 ML). In this graph blue bars correspond to clusters formed with C_{60} molecules and the orange bars are measurements obtained from C_{70} molecules.

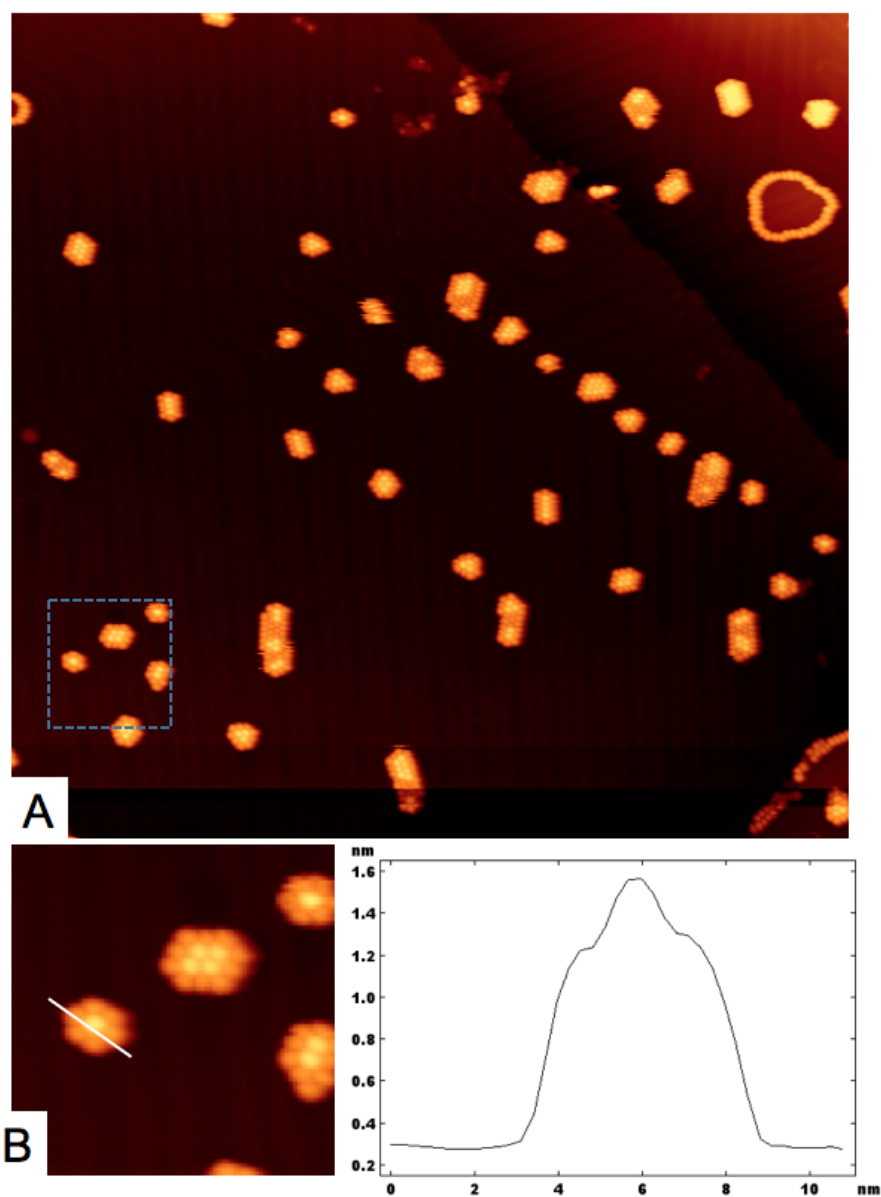


FIGURE 4.8: A) Stable structures formed at room temperature with 0.09 ML Au and 0.21 ML of C_{70} molecules. $145.28 \text{ nm} \times 145.28 \text{ nm}$, $V = -2.18 \text{ V}$, $I = 0.05 \text{ nA}$. B) Zoomed in image of part highlighted by a blue square with height profile along the white line are presented. Results agreed with molecules having their long axis perpendicular to the surface.

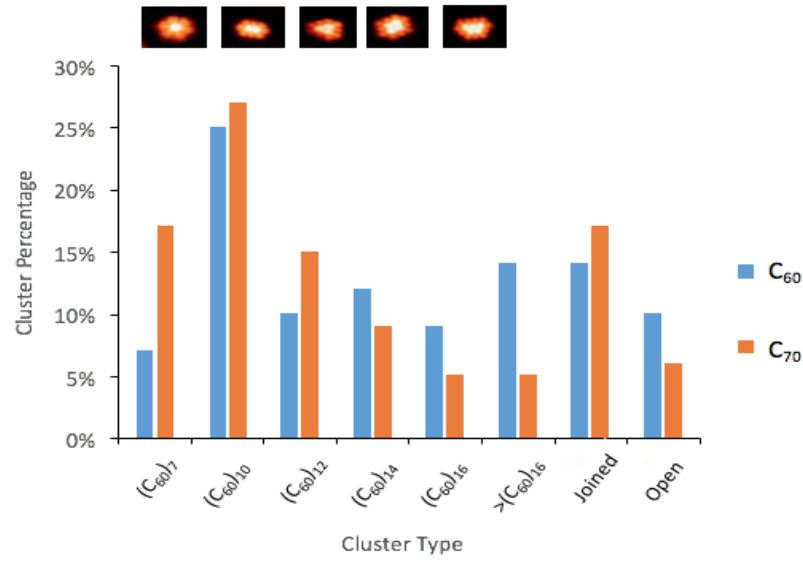


FIGURE 4.9: Distribution of cluster sizes for both fullerene molecules (C_{60} and C_{70}) with same coverage of Au (0.09 ML) and fullerene (0.2 ML) is shown. Orange bars correspond to the results obtained with C_{70} molecules while blue shows results of C_{60} molecules deposition. It can be seen that in both cases ranges of clusters obtained are very comparable.

Here, since similar ratio of fullerenes to Au have been used, the percentage of joined and open structures observed are also comparable. The formation and type of such clusters are explained in more detail in the next sections.

4.4.3 Joined Clusters

It has been shown that, at low temperature, fullerene molecules tend to join step edges of Au islands deposited on elbow sites. As fullerene coverage increases, C_{60} -Au clusters that are close to each other can join and form a joined structure. Then, the only requirements for formation of such clusters are high fullerene coverage and two or more closely spaced Au islands. Figure 4.10, shows the effect of temperature on movement of fullerene molecules that resulted in the formation of such structures.

As shown in figure 4.10, initially the space between two Au islands in clusters marked as “a” was filled by C_{70} molecules. The position of Au islands are highlighted by blue circles on this structure. A neighbouring cluster, “b”, was also observed to have a large fullerene island around it. As the temperature increases, extra C_{70} molecules that are not directly attached to the Au islands start to move. If the fullerene islands formed around clusters is big enough then movement of molecules can help in filling the gap between neighbouring structures, resulting in the formation of a joined cluster. This can be seen from the image obtained at 266 K (image 4.10E). Increasing temperature further will then help molecules to reach a thermodynamically stable close packed arrangement.

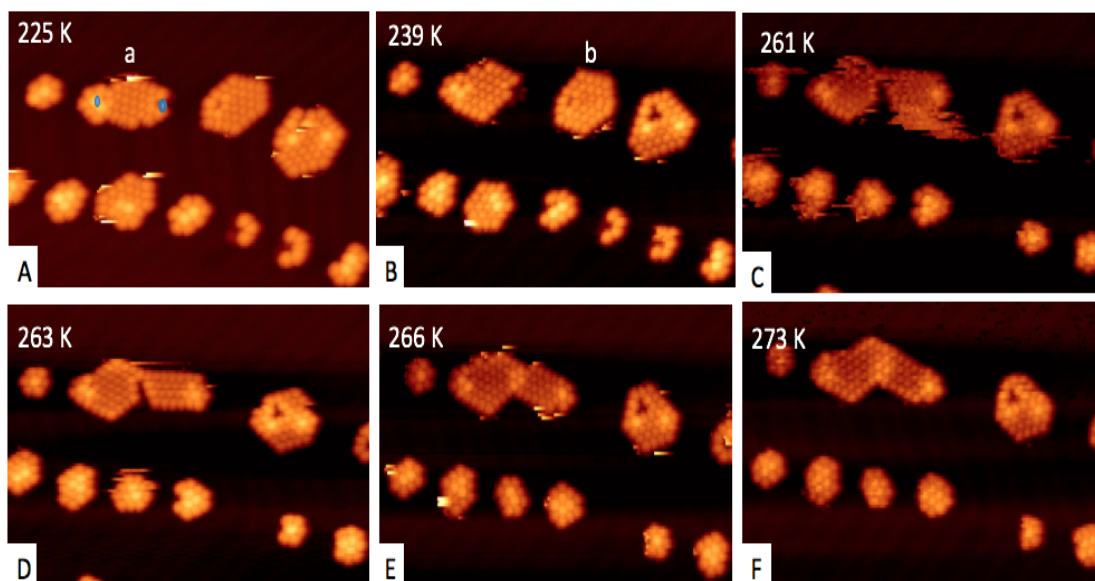


FIGURE 4.10: Changes observed in surface as temperature increases from 225 K to 273 K. As temperature increases, molecules on large clusters, marked as “b”, can move around and get attached to neighbouring structures, marked as “a”, to form joined clusters. Further increases in temperature would result in the fullerene island forming the most thermodynamically favoured arrangement.

Joined structures can be divided into three groups: close packed fullerene islands formed on fcc areas (group one), joined clusters formed of Au islands on the same elbow type (group two), and finally formation of joined clusters with a ring structure (group three). Example of each group is presented in figure 4.11.

Group one are clusters that mainly form in places with larger fcc areas. This enlargement in fcc sections are normally a result of surface defects. Clusters observed on such areas do not change the reconstruction patterns and form a close packed structure within the reconstruction boundaries.

Group two correspond to structures formed on closely spaced Au islands on one elbow type. In this case fullerene molecules can pass over the reconstruction pattern to join clusters. Joining molecules on same elbow type without disturbing the reconstruction pattern is not a new phenomenon. A similar scenario has been observed where deposition of trans-BCTBPP molecules at 63 K resulted in formation of chains up to 100 nm in length [28]. However, our clusters show joining of maximum three structures with coverages examined. Figure 4.11B, shows examples of such clusters as well as the corresponding structural models. In models presented here, each ball is a fullerene molecule, where yellow spheres correspond to the ones sitting next to the step edges, reds are molecules on top of Au islands and blues are extra fullerenes. It has been observed that such structures require about 4 rows of molecules. The number of extra molecules can vary from 5 to 51 but in almost all cases at least four molecular rows have been observed.

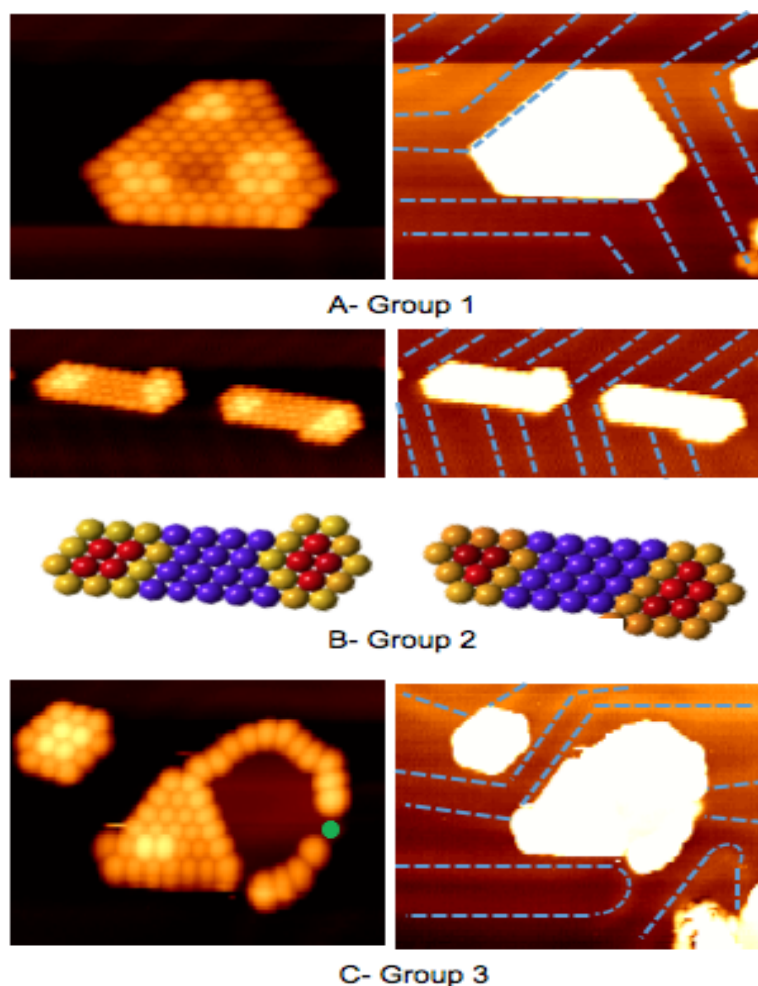


FIGURE 4.11: Different types of joined structures were observed on the surface. In each case two contrasts are presented to highlight the structure and the reconstruction pattern. Blue lines on images indicate the position of DLs. A) An example of the closed pack fullerene structure with three Au islands. The structure is formed within fcc area without disturbing the reconstruction lines. Scan “B” shows example of two joined clusters close to each other with their models. In each model yellow molecules are attached to the Au step edges, red are molecules on top of the Au islands and blue are the extra molecules. In scan “C” a joined cluster involving a ring structure is presented. Such clusters can influence the reconstruction pattern as the Au island has tendency to grow and expand fcc sections.

Final group, group three, are clusters with an open or ring structure involved, as shown in figure 4.11C. In this case, the Au island in the ring structure can expand towards fcc area and disturb the reconstruction pattern. If the island grows large enough, reconstruction lines can also appear on the ring structure as well. In this

case fullerene molecules, around the step edges, prefer the fcc sites that explains the gaps in ring structures observed. In the example presented here this gap is highlighted by a green dot.

So when the coverage of C_{60} with respect to Au is high then joined structures are observed. But the probability of forming each type of structure is very dependent on the coverage used. Over all, the least common type is group one (Image 4.11A) that requires surface defects to form and the most commonly observed structure, for coverages examined, is group two (Image 4.11B). Formation of ring structures requires high coverages of Au at the same time. In next section more details on the ring structure will be provided.

4.4.4 Ring Structures

Open or ring structures are another type of clusters observed on the surface. Such structures can form when the amount of fullerene molecules on an island is not enough to reach a stable magic cluster. In this case molecules will only cover the step edges to stabilise the structure up to room temperature and above (~ 410 K).

Based on the Au islands formed, ring structures can be divided into three groups. For smaller Au islands, structures observed are in fcc sections only. In this case the shapes of structures are influenced by the reconstruction lines, as clusters do not pass over them. For larger Au islands there are two possibilities: the Au island can grow and part of surface that is now covered by the new Au atoms would then relax to form fcc section. This results in modification of the reconstruction lines to fit the new fcc areas. The other possibility is the growth of Au island towards hcp sections with reconstruction lines passing over them. In this case, fullerene molecules show preference for the fcc side of step edges, similar to the ring structures observed in joined clusters.

Disturbing the reconstruction pattern or expanding to hcp areas, can be explained based on the type of Au step formed. Depending on the position of Au atoms deposited, reconstruction lines can pass over the step edges or make a turn. Therefore, the shapes of clusters formed are dependent on the number of Au atoms and fullerene molecules available as well as the position of the clusters. Figure 4.12, shows three type of clusters explained with different colours. In this figure, different contrasts of scan area have been used to make the clusters and reconstruction lines more clear.

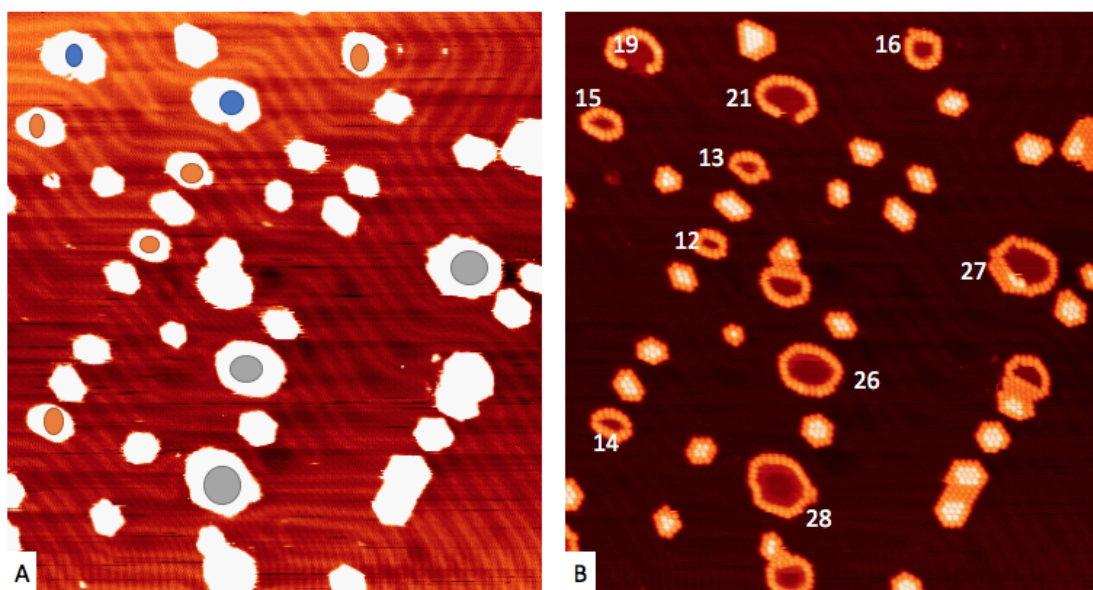


FIGURE 4.12: Scan obtained at room temperature showing three different types of ring structures. Two different contrast are included to show the reconstruction pattern (A) and clusters (B) more clearly. Orange correspond to small Au islands that can fit within the fcc regions. Blue are larger Au islands that do not disturb the RLs but can expand to hcp areas. Finally, grey shows large Au islands that have expanded the fcc regions and as a result modified the RLs. In Image B values given next to each ring structure show the number of C_{60} molecules. $121\text{ nm} \times 121\text{ nm}$, $V = -1.93\text{ V}$, $I = 0.05\text{ nA}$.

In figure 4.12, clusters marked as orange are small ring structures formed on bulged elbows. This can be surprising as (at low temperatures) the average size of Au islands on these sites was shown to be greater than that of pinched elbows due to the larger fcc areas available (in comparison to hcp sites). However, measurement

of fcc areas on both elbow types has shown that on bulged elbows it is ~ 1.2 nm smaller than pinched elbows [126]. This explains the smaller size of structures observed, compared to clusters formed on the same position of pinched elbows.

For ring structures formed on pinched elbows the average size of Au islands confined in the fcc sites, grey islands, is ~ 16 nm² and for islands expanded towards the hcp areas, marked as blue, is ~ 14 nm². This increase in size of Au islands, compared to ~ 7 nm² measured right after deposition of atoms, is a result of unstable structures breaking down at higher temperatures. As it was mentioned, free atoms can join existing islands and form even larger clusters or ring structures. It should also be noted that at low temperature, almost all clusters were formed on hcp sites of pinched elbows. However, ring structures shown in this scan are located in fcc sections. It is expected that as temperature increases clusters would move in the form of loosely bound groups from hcp to fcc areas [126].

In figure 4.12B, numbers next to each ring structure correspond to the number of fullerene molecules involved. Table below shows percentage of ring clusters observed in each categories out of 55 structures counted with the average number of C_{60} molecules around it.

	Small Close Rings	Large Close Rings on fcc	Large Rings Expanded to hcp
Percentage of clusters observed	58 %	26 %	16 %
Average number of C_{60} molecules	12	23	21

TABLE 4.1: Distribution of different ring structures and average fullerene molecules decorating the step edges. In total 55 clusters were counted.

The most common type of clusters observed are the small Au islands formed at the elbow sites that do not require atoms from other clusters. And the least common structures are clusters expanded to hcp sites as they require higher number of Au atoms. The average number of fullerene molecules observed also increases with the size of Au islands that indicates more molecules are required to stabilise larger Au island up to room temperature.

In order to obtain higher percentage of larger ring structures, it is possible to anneal the sample. Breaking and merging other structures can help in production of large ring structures [126]. Another possibility is to deposit Au and fullerene molecules at the same time at ~ 180 K. Increasing deposition temperature would result in formation of larger islands and ring structures on the surface. Atoms at higher temperature would have enough kinetic energy to form larger Au islands and clusters in a shorter time after reaching the surface.

Figure below shows ring structures formed from both methods recommended. Scan 4.13A is an example of a surface at room temperature after deposition of 0.04 ML Au and 0.1 ML of C_{70} at 200 K with Au deposition being started one minute earlier. As it can be seen, at room temperature, about 65 % of clusters are ring structures.

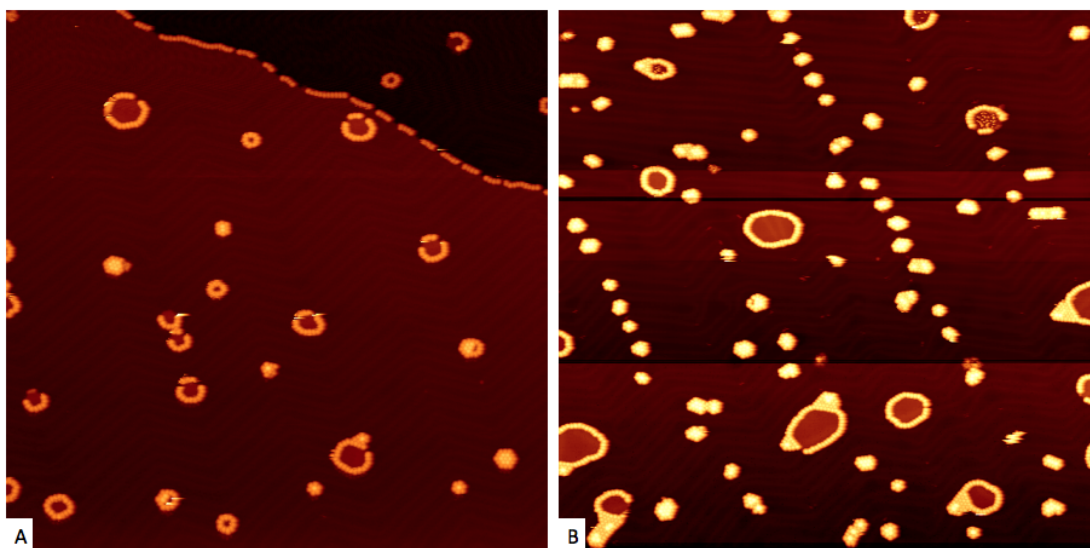


FIGURE 4.13: Ring Structures formed at room temperature. A) 0.04 ML Au atoms and 0.1 ML of C_{70} molecules were deposited at 200 K with Au being deposited 1 minute earlier. 150.29 nm \times 150.29 nm, $V = -1.71$ V, $I = 0.04$ nA. B) Scan obtained after 15 minutes annealing of the sample covered with magic clusters at 360 K. The coverage used for this surface was 0.08 ML Au deposited at 110 K, surface was then annealed to 150 K for deposition of 0.2 ML of C_{70} . 163.32 nm \times 163.32 nm, $V = -2.36$ V, $I = 0.05$ nA.

Scan 4.13B, shows formation of large ring structures after annealing a sample

covered with magic clusters for 15 minutes at 360 K. The coverage used was 0.09 ML Au deposited at 110 K, followed by deposition of 0.2 ML of C_{70} at 150 K. Sample was then slowly annealed to room temperature; an example of room temperature scans is presented in figure 4.8. Only after confirmation of the clusters sample was then annealed that resulted in formation of larger ring structures with reconstruction lines on clusters.

As it was mentioned, formation of ring and joined structures can act as a reference point to determine if the fullerene coverage was enough or not. But such side products can also have potential in different applications. For example, the ring structure observed is similar to the naturally existing Rhodospireillum photometric rings that has photosynthetic properties [158]. The C_{60} and Au films are also commonly used as building blocks of solar cells. Normally a polymer layer with optical adsorption properties is used to generate bound excitons. Due to the high electron transportation properties of fullerenes, excited electrons would move quickly towards fullerene layers, which would then initiate the flow of current [159]. Being able to arrange fullerene molecules in a similar manner to photometric cells can help to produce new devices with tunable properties [126].

4.5 Co-Deposition of Au and Fullerene Molecules

So far in all experimental results presented, Au atoms were initially deposited and only after confirming the existence of Au islands, fullerene molecules were added. This increased the chance of molecules finding existing islands step edges and forming magic clusters. So, next step was to check the effect of depositing Au and C_{70} at the same time. Scans below show results obtained after deposition at low temperature as well as the surface at room temperature.

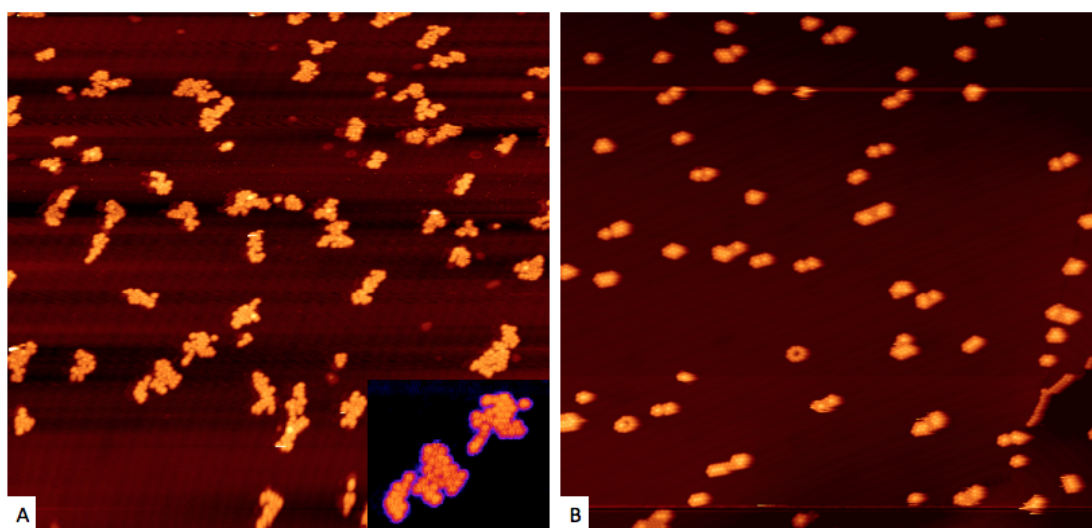


FIGURE 4.14: Scans obtained from deposition of 0.04 ML Au and 0.2 ML C_{70} at 110 K (A) and room temperature (B). A) At 110 K, fullerene and Au atoms are mixed rather than having C_{70} molecules around Au islands. 140.27 nm \times 140.27 nm, V= -1.89 V, I= 0.04 nA. B) Once sample reaches room temperature normal magic cluster shapes can be observed. 148.29 nm \times 148.29 nm, V= -1.97 V, I= 0.04 nA.

Figure 4.14A, shows a surface at 110 K after deposition of Au and C_{70} almost at the same time. In the previous method fullerene molecules are attached to step edges of the Au island or sits on top of it at low temperatures. This resulted in formation of uniform fullerene islands on elbow sites. However, here we have a mixture of Au and C_{70} molecules. The inset in figure 4.14A, shows two examples with Au atoms being trapped in fullerene islands. This opens opportunity of forming magic clusters away from the elbow sites. If the flux is high enough then molecules can join and form clusters before they reach elbow positions. Then, density of structures obtained at room temperature can also increase.

Scan 4.14B, was obtained at room temperature, that shows all clusters being formed off the elbow sites on the fcc regions with similar range of structures obtained from the old method used. It can be concluded that “mixing” Au and fullerene molecules at 110 K would give almost the same result as the step by step deposition with higher probability of clusters being formed away from elbow

sites. This requires the sample temperature being below 150 K. As explained in earlier section, deposition of molecules at temperatures above 150 K will result in formation of few extremely large clusters or ring structure.

4.6 Summary

After production of C_{60} -Au magic clusters the next step was to study how we can control the size of structures observed. This includes varying Au and fullerene molecules coverage, temperature and delay in deposition time.

Results obtained have shown that Au coverage plays an important role in controlling the range of clusters observed on the surface. So as coverage increases a wider range of structures can be formed. But controlling the size of Au island at each elbow site is hard and producing a high percentage of one type of clusters can be challenging. In order to improve this, the effect of temperature was analysed. It was shown that by controlling temperature just below room temperature (~ 260 K), it is possible to produce a sample with more than 50 % of clusters being $(C_{60})_7$.

Fullerene coverage, with both C_{60} and C_{70} molecules, was the next parameter to be examined. It has been shown that, if the amount of molecules deposited is not enough then a higher percentage of open, also known as ring, structures are observed. On the other hand, for high coverages joined clusters are more commonly formed. These results were confirmed by both C_{60} and C_{70} molecules that indicated ellipsoidal shape of C_{70} molecules doesn't have any effect on structures formed. Results obtained have suggested that C_{70} molecules tend to have their long axis perpendicular to the surface. As a result, the diameter parallel to the surface is comparable to that of the C_{60} molecules. This allows the same model of $(C_{60})_m$ - $(Au)_n$ being applied to the clusters formed. Finally, it was shown that rather

than step by step deposition of Au followed by fullerene molecules it is possible to deposit both at the same time at low temperatures. This does not have any effect on the range of structures observed but increase the probability of clusters being formed away from elbow sites.

The next chapter will provide more detail on how we can control the position of clusters formed as well as manipulating magic clusters by depositing more Au/ C_{60} at low temperatures on stable structures.

Chapter 5

Manipulating Magic Clusters

5.1 Introduction

In chapter 4, different parameters that can have an effect on the range of clusters observed were examined. In this chapter the main focus is on the manipulation of the position and size of the clusters. The results presented here can be divided into two sections. In the first part, a short description of the clusters' position with respect to the Au reconstruction pattern is provided. This is then followed by a description of how the majority of structures are located on one elbow type. In the second part of this chapter, the effect of further deposition of Au and C_{60} molecules at low temperature on the magic clusters is investigated.

5.2 Controlling the Position of Clusters

5.2.1 Position of Clusters at Room Temperature

The first step was to study the position of clusters with respect to the elbow sites. Figure [5.1](#) shows the same area of a selection of structures observed at room

temperature, using two different image contrasts to highlight the clusters and their positions relative to the reconstruction pattern. In figure 5.1B, blue lines show the central position of elbows in the reconstruction. Discontinuities in these lines are due to the disturbance of the DLs and therefore a change in their pattern. As explained in the previous chapter, the formation of rings or joined clusters can be a reason for such changes. Based on these lines, it can be seen that the majority of clusters are positioned with their centre of mass located at the elbow sites of the reconstruction.

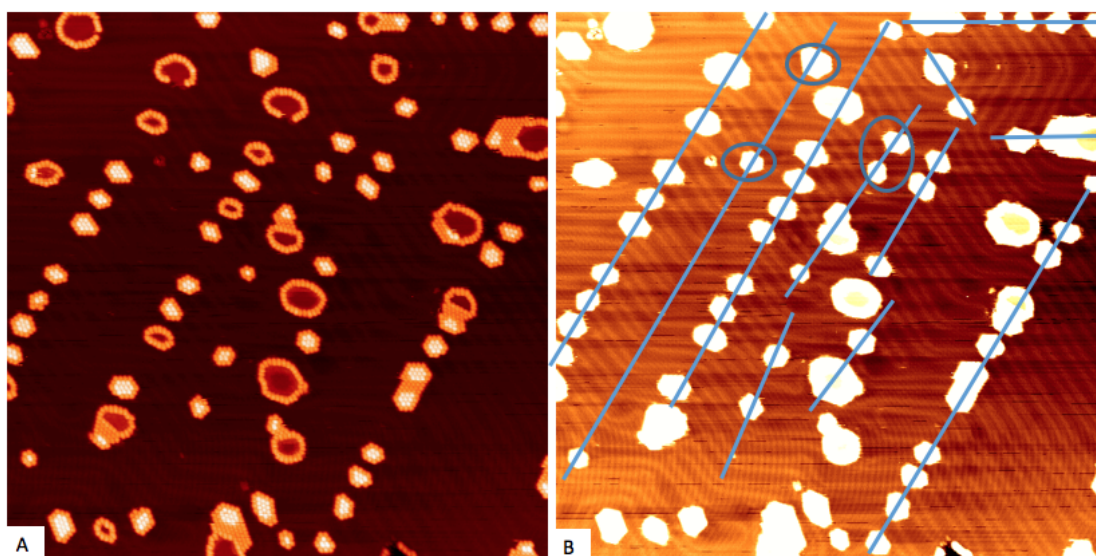


FIGURE 5.1: Different image contrast of the same area are presented to highlight cluster's size (A) and position (B). Blue lines in figure B, pass through the centre of elbow sites, indicating that the majority of clusters are formed at central position in fcc and hcp areas. Clusters positioned on hcp sites of pinched elbows are highlighted by the blue circles. 121 nm \times 121 nm, $V = -1.93$ V, $I = 0.05$ nA.

At low temperatures, both elbows are normally fully covered with Au and fullerene islands. After reaching room temperature, as presented in figure 5.1, clusters have shown to be preferentially located at bulged elbows. Since Au islands start to form on type-x of elbows, the stability of structures formed on pinched and bulged can be different. At bulged elbow sites, the formation of clusters starts from fcc areas, which makes them to be more stable up to room temperature due to its larger area and lower potential. This explains the higher coverage (on average 70 %) of

clusters observed at these sites. However, at pinched elbow sites, structures have been observed on both fcc and hcp areas. In this case, cluster formation starts from the hcp areas, where type-x elbow is positioned. As the sample temperature is increased, the clusters can overcome the DLs boundaries and move towards fcc areas in the form of a loosely bound group, similar to the behaviour of ring structures [126]. In figure 5.1, the clusters observed on hcp areas are highlighted with blue circles.

Over all, clusters display preferential growth on fcc areas compared to hcp sites, while forming on on top of the DLs, or crossing over them, is avoided.

5.2.2 Effect of Temperature on Au Islands

Efforts were made to control the self-organised growth of the clusters using the surface reconstruction as a template. So far the elbow sites of the Au (111) reconstruction pattern were responsible for growth of the clusters. The aim of the following experiments was to check the possibility of arranging clusters on one type of elbow, i.e. pinched or bulged, only.

It has already been shown that after the formation of magic clusters on the Au surface, annealing it to about 350 K causes the clusters to migrate to the location of the pinched elbows [128]. These elbows are known to have larger fcc areas, which makes them more favourable for cluster growth. At this temperature, only fully compact clusters or large Au islands with C_{60} molecules decorating their step edges were observed. An example of this type of surface is shown in figure 5.2A, where empty bulged elbows are highlighted by white boxes.

After demonstrating that clusters could be selectively organised on the pinched elbows of the herringbone reconstruction, attempts were made to arrange the structures on the bulged elbow sites. To do so, Au atoms were deposited at 115 K followed by heating of the sample to 180 K for at least 90 minutes. The sample

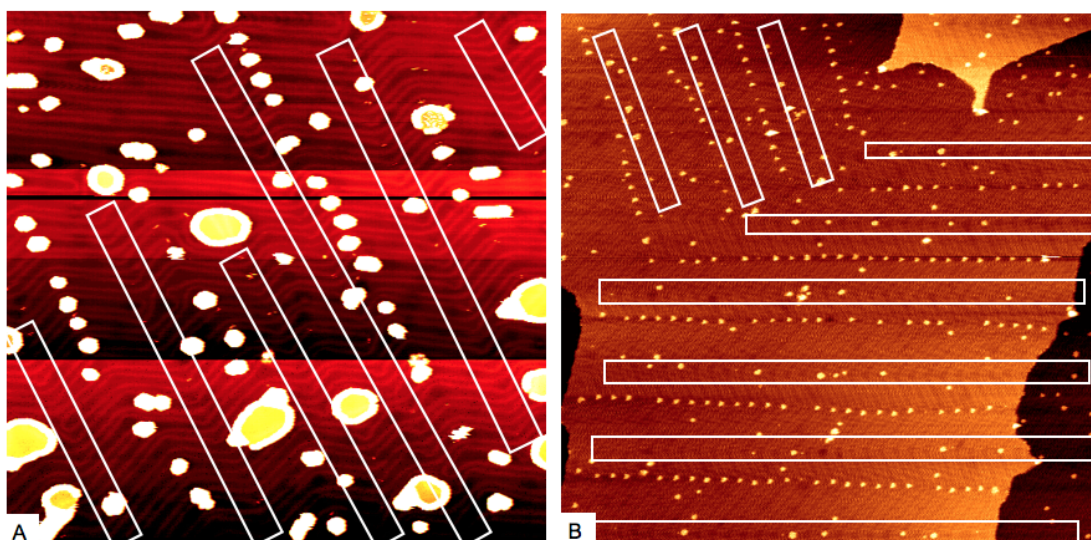


FIGURE 5.2: A) 0.09 ML of Au atoms and 0.04 ML of C_{70} molecules were deposited at low temperature. After confirmation of magic clusters at room temperature, sample was annealed at about 350 K. This helped to migrate the clusters to the pinched elbows. Empty bulged sites are indicated by white rectangles. 163.32 nm \times 163.32 nm, $V = -2.36$ V, $I = 0.05$ nA. B) Scan obtained at 180 K after annealing a sample with 0.01 ML of Au atoms for 2 hours. The Au islands have moved from the pinched to the bulged elbows. In this scan, pinched elbows are highlighted by white boxes. 250.5 nm \times 250.5 nm, $V = -1.6$ V, $I = 0.05$ nA.

was then cooled down to 150 K for deposition of fullerene molecules. This extra annealing step results in almost all of Au islands formed on pinched elbow sites to move. An example of this type of surface is shown in figure 5.2. In figure 5.2B, deposition of 0.01 ML Au at 115 K was followed by annealing the sample at 180 K for two hours. This resulted in Au islands re-organising from pinched to bulged elbows. In this image, the empty pinched elbows are highlighted by white boxes.

It has previously been explained that at low temperature, on pinched elbows, Au islands are formed on hcp areas. By increasing the temperature to about 180 K it is possible to provide energy for these atoms to move away from the hcp sites. During this time, atoms are expected to be removed from Au islands. Due to the lower potential barrier for atoms to move from the hcp sites to the fcc regions than the reverse action, a net flow of Au atoms to fcc area is obtained

[160, 161]. However, the energy of them is not high enough to move freely on the surface. In this case, reconstruction lines can act as barriers that guide the atoms, towards neighbouring islands on bulged elbow sites. This was confirmed by the constant coverage of the elbow sites (0.01 ML) before and after annealing. The size distribution of islands was also measured and the results obtained are presented in the histogram shown in figure 5.3.

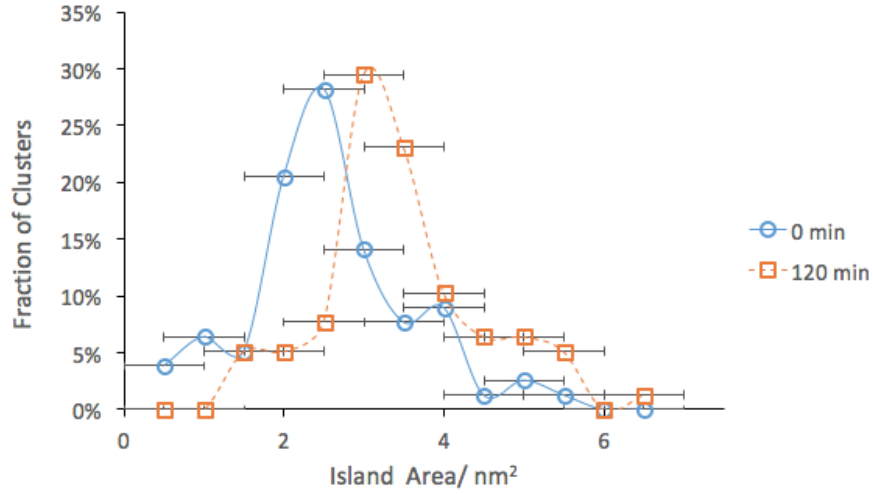


FIGURE 5.3: Size distribution of Au islands on bulged elbows before (blue) and after (red) annealing the surface for two hours at 180 K. Error on measurements are due to the rounding of the values.

The results presented in figure 5.3 show a range of sizes obtained for Au islands on bulged elbows. Based on this graph, before annealing the majority of the Au islands consisted of $\sim 2.5 \pm 0.5 \text{ nm}^2$, while after annealing, the peak position has shifted to $\sim 3.0 \pm 0.5 \text{ nm}^2$. The error on these values are estimated based on the FWHM of the distributions. This indicates a 0.5 nm^2 increase in the area of islands on the bulged elbows after annealing. At this point the amount of Au originating from islands on hcp areas is larger than the number of atoms lost from the step edges of the islands located on fcc areas. Until the Au flux leaving the edges of the fcc - located islands becomes comparable to the flux coming from islands on hcp areas. Then the rate of re-attachment of Au atoms to islands on

fcc areas equals rate of detachments. This has been confirmed by measuring the average size of Au islands on bulged elbows after 350 minutes of annealing at 180 K. Results obtained are shown in figure 5.4.

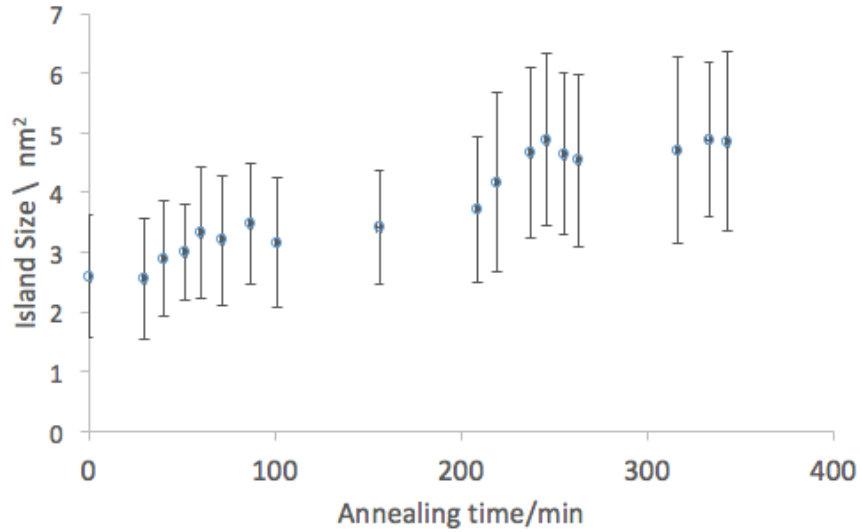


FIGURE 5.4: Variation in average size of Au islands measured over fcc areas of herringbone reconstruction as a function of annealing time at 180 K. Error bars correspond to the standard deviation on measurements.

The variation in average islands size as a function of annealing time at 180 K is presented in figure 5.4, and was obtained from a surface with 0.01 ML Au coverage. The area measured at 0 min corresponds to the average island size at 115 K, before annealing starts. Based on this graph, the average size of the Au islands linearly increases with time up to 250 min of annealing. After that no major changes were observed, indicating that the number of Au atoms gained by the islands is comparable to the amount lost.

Being able to displace Au islands, opens up the opportunity to control the size distribution of the clusters on the elbows sites. To do so, after each deposition, the surface can be annealed so that Au islands move away from pinched elbows. Repeating deposition and annealing steps would result in growth of Au islands on bulged elbows, while after deposition alone small islands are observed on pinched

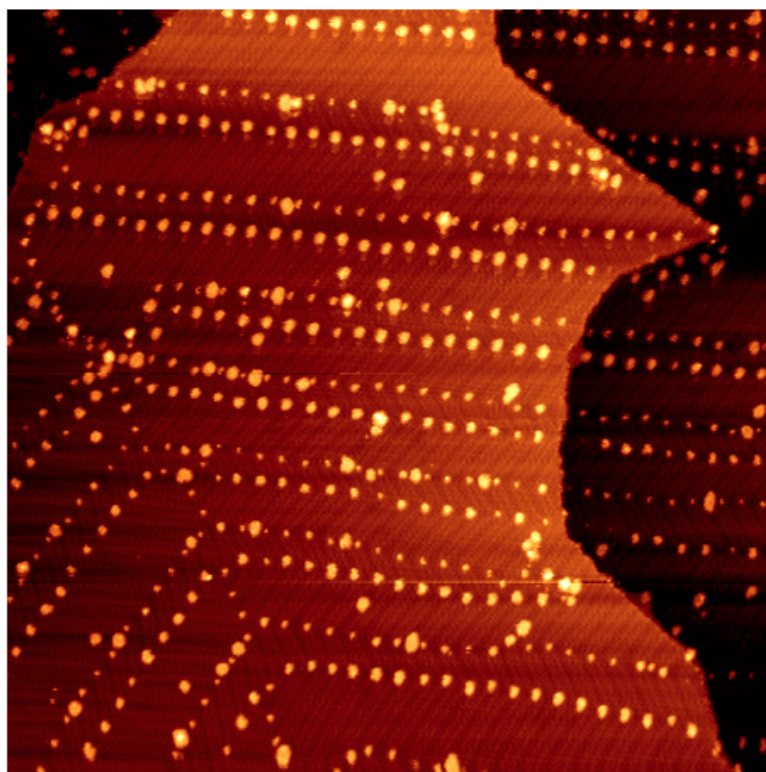


FIGURE 5.5: Scan obtained after three depositions of 0.01 ML Au at 110 K followed by annealing at 180 K for two hours after the first and second depositions. 253.49 nm \times 253.49 nm, V= -1.93 V, I= 0.05 nA.

elbow sites. Figure 5.5 shows an example of the type of surface obtained after 2 steps of deposition and annealing at 180 K for 2 hours. During each deposition 0.01 ML Au was deposited onto the surface at 110 K and after each annealing step individual islands on bulged elbow receive about 7 Au atoms. Finally, an additional Au coverage (0.01 ML) was deposited on the surface.

It also worth noting in figure 5.5 that there are Au islands on pinched elbows, locating on fcc sites rather than hcp areas where they are expected. At these positions the Au atoms have gained energy and moved away from hcp areas but they have formed stable islands before reaching other elbow sites. Such clusters can also be viewed as a by-product of the annealing process. The histogram shown in figure 5.6 shows the distribution of Au atoms on pinched and bulged elbows after three cycles of deposition and annealing.

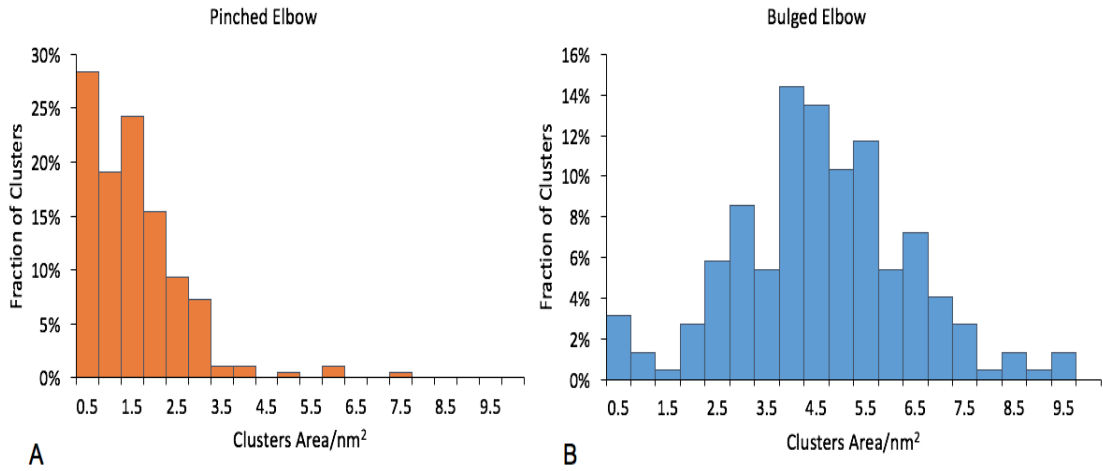


FIGURE 5.6: Distribution of Au atoms on pinched and bulged elbows are presented. The results obtained show that the average size of Au islands on bulged elbow is ~ 3 times larger than islands formed on pinched elbows.

It can be seen from this analysis that the average size of the Au islands on bulged elbows ($4.6 \pm 1.9 \text{ nm}^2$) is almost three times larger than the size of those on pinched elbows ($1.4 \pm 1.0 \text{ nm}^2$). The error on these values correspond to the standard deviation on measurements. The average values obtained are in agreement with general evidence presented in figure 5.5.

So by depositing Au atoms at low temperature and annealing surface at 180 K, it is possible to control the size as well as position of Au islands. The ability to control the position of Au on a solid surface can be useful in production of Au nano-materials such as optical sensors [162]. Since the Au islands are the building blocks of the magic clusters, this method can help to control the clusters formed too. More information on formation of clusters is provided in next section.

5.2.3 Formation of Clusters on Bulged Elbow

As mentioned, Au islands is a major building block in defining the size and position of magic clusters. To prepare magic clusters away from pinched elbows, 0.01 ML of

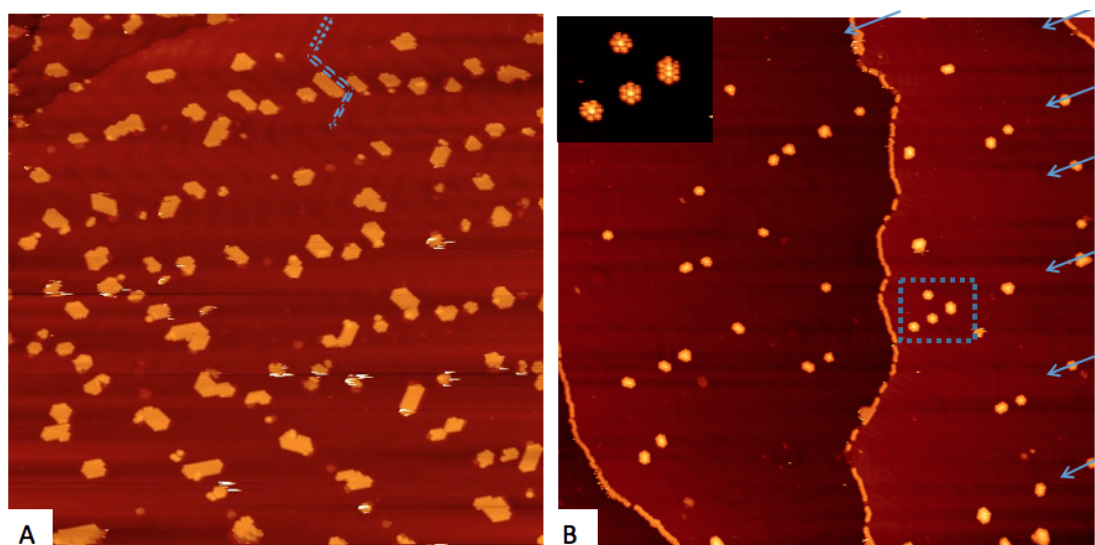


FIGURE 5.7: A) After annealing 0.01 ML Au on the reconstructed Au (111) surface for 2 hours at 180 K, 0.1 ML of C_{60} molecules were deposited at 150 K. The STM image shows the formation of fullerene islands on the bulged elbows at 150 K. 150 nm \times 150 nm, $V = -2.5$ V, $I = 0.05$ nA. The surface is then annealed to RT where most of the clusters (86%) are on bulged elbows as highlighted by the blue arrows. Some of the clusters formed are shown in top right hand side inset corresponding to the area marked by the blue box. 189 nm \times 189 nm, $V = -2.14$ V, $I = 0.05$ nA.

Au was deposited onto the reconstructed Au (111) surface at 110 K and annealed at 180 K for 2 hours to reorganise the Au islands selectively on to bulged elbow sites. 0.1 ML of C_{60} molecules were then deposited at 150 K. The resulting surface is shown in figure 5.7A. Although fullerene islands are observed on some of the pinched elbows, the majority of C_{60} molecules have formed islands around the Au step edges on bulged elbows. The sample's temperature is then gradually increased to room temperature in order to form thermodynamically stable structures. Figure 5.7B shows the resulting magic clusters observed at room temperature, where 86% of them are located on bulged elbows highlighted by the blue arrows. In this scan, the extra fullerene molecules have decorated the step edges.

After confirming the formation of magic clusters, the size distribution of the observed structures was analysed. The histogram in figure 5.8 shows that the range of clusters obtained is very similar to the pattern observed in chapter 4 (figure 4.3)

for low coverages. Since the amount of Au deposited on the surface is very small, the range of structures obtained has not changed. Similarly, the highest coverage of clusters observed was $(C_{60})_7$ with a decrease in the number of structures as their size increases.

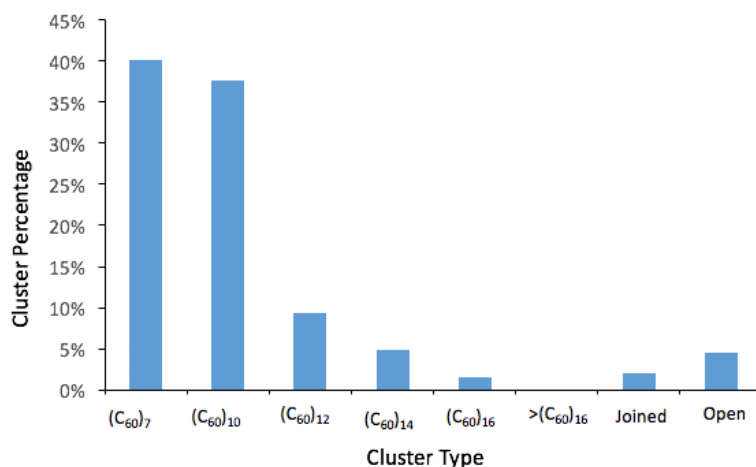


FIGURE 5.8: Range of clusters observed at room temperature with 0.01 ML Au and 0.1 ML fullerene coverage.

To summarise it is possible to organise almost all of clusters on bulged elbow sites by adding an annealing step before the deposition of the fullerene. The same procedure can also be employed to control the size of the structures on the surface. This requires a few steps of deposition and annealing and then a final step of Au deposition before adding the fullerene molecules to the surface.

5.3 Addition of Au Atoms to Stable Structures at LT

As for the next part of project, stable clusters were manipulated by adding Au atoms at low temperature. This allows to investigate how the magic clusters interact and transform in the presence of extra atoms. In order to do so, magic

clusters formed on the Au (111) surface were cooled down to 115 K prior to deposition of more Au atoms. Figure 5.9 shows an example of scan areas with an additional 0.03 ML Au deposited on the fullerene dosed surface. As shown in figure 5.9A, elbows with no clusters have been decorated with monolayer Au islands. This is confirmed by the height profile (shown in 5.9B) obtained between the blue arrows in figure 5.9A.

Figure 5.9C shows another scan area where the attachment of Au to the $(C_{60})_m$ - $(Au)_n$ clusters can be seen more clearly. There are three ways that Au atoms can interact with the magic clusters. In the first case, Au islands attach to one side of the $(C_{60})_m$ - $(Au)_n$ structure, next to fullerene molecules, without modifying the structure of the magic clusters. Examples of such clusters are highlighted in figure 5.9C by blue circles. In the second case, indicated by yellow circles, Au atoms deposited have reached the central island and resulted in opening of the clusters. Finally, it is possible for both scenarios to take place on a cluster, examples of such scenarios are highlighted with purple circles. In this case, on one side, Au atoms have formed islands next to the fullerene molecules and on the other side, atoms have reached the existing Au island.

These structures are only observed at low temperatures, as the temperature is increased the Au and fullerene molecules tend to mix and arrive at a stable form. At higher temperatures, extra Au atoms can diffuse onto the central islands. If there are enough fullerene molecules available, or there have been captured during the annealing process, then larger stable clusters can be observed. Otherwise, molecules on top of the island will move down to be attached to the lower step edges of the structures where the bonding is stronger. This results in the formation of ring structures. The process involved is shown in figure 5.10 below.

In figure 5.10, at 115 K, two $(C_{60})_7$ and one $(C_{60})_{10}$ structures are observed, which have opened up. Since such structures are not stable at room temperature and are only observed after deposition of the Au atoms, it can be concluded that it

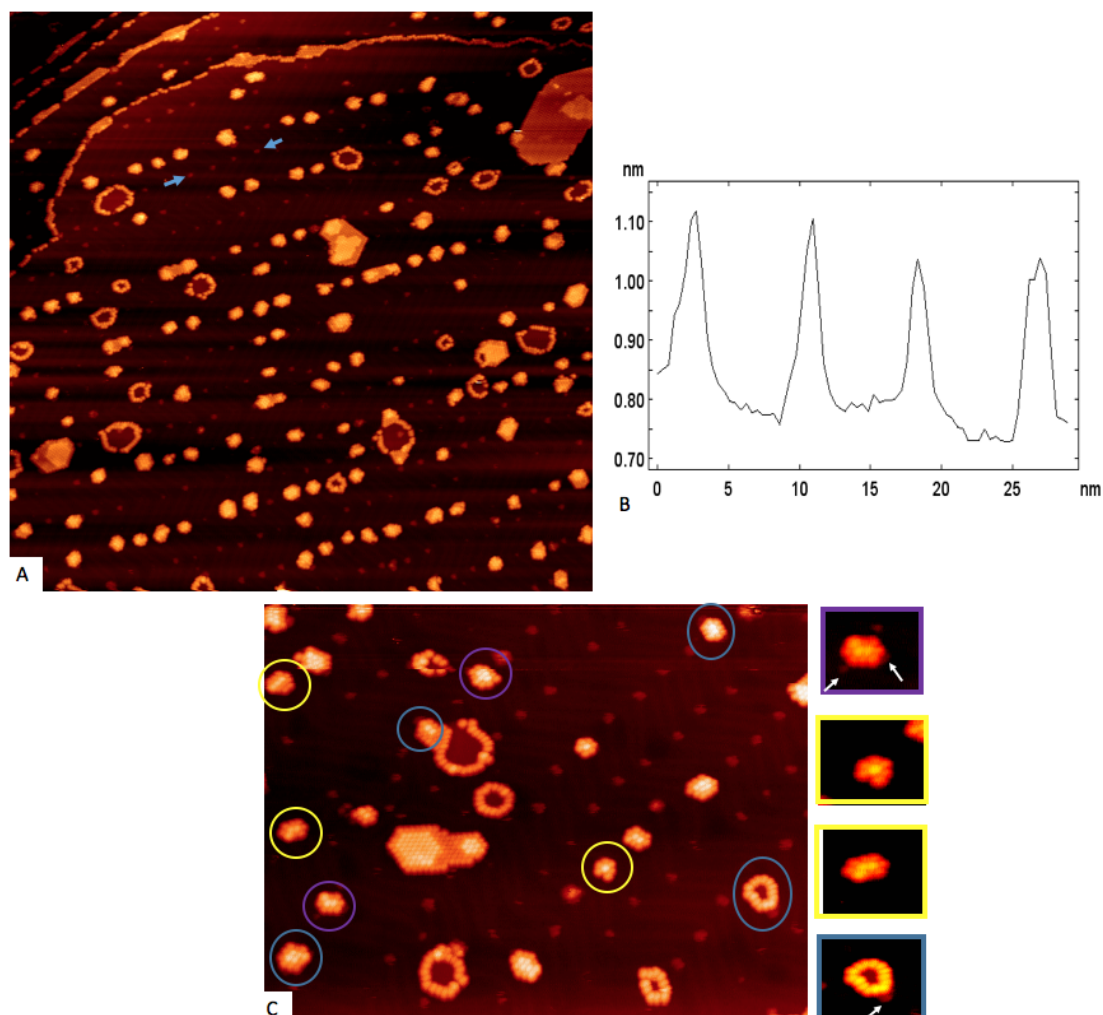


FIGURE 5.9: A) 0.03 ML of Au atoms were deposited at 115 K onto a surface covered with magic clusters that resulted in the formation of islands on empty elbows as well as attaching to existing clusters. B) Height profile between the blue arrows indicated in the previous image, showing that the islands between the magic clusters are monolayer high Au islands. 200 nm \times 200 nm, $V = -1.89$ V, $I = 0.05$ nA. C) Another scan area that shows clearly how extra Au atoms are attached to clusters. This can be divided into three groups: blue circles highlight Au islands being formed on one side of the structures, yellow circles highlight cases where Au atoms are deposited on top of magic clusters, while purple circles indicate a combination of both scenarios. Zoom in image of some examples are shown on the right hand side. White arrows in these images correspond to the position of Au islands next to the clusters. 100 nm \times 61.3 nm, $V = -1.97$ V, $I = 0.05$ nA.

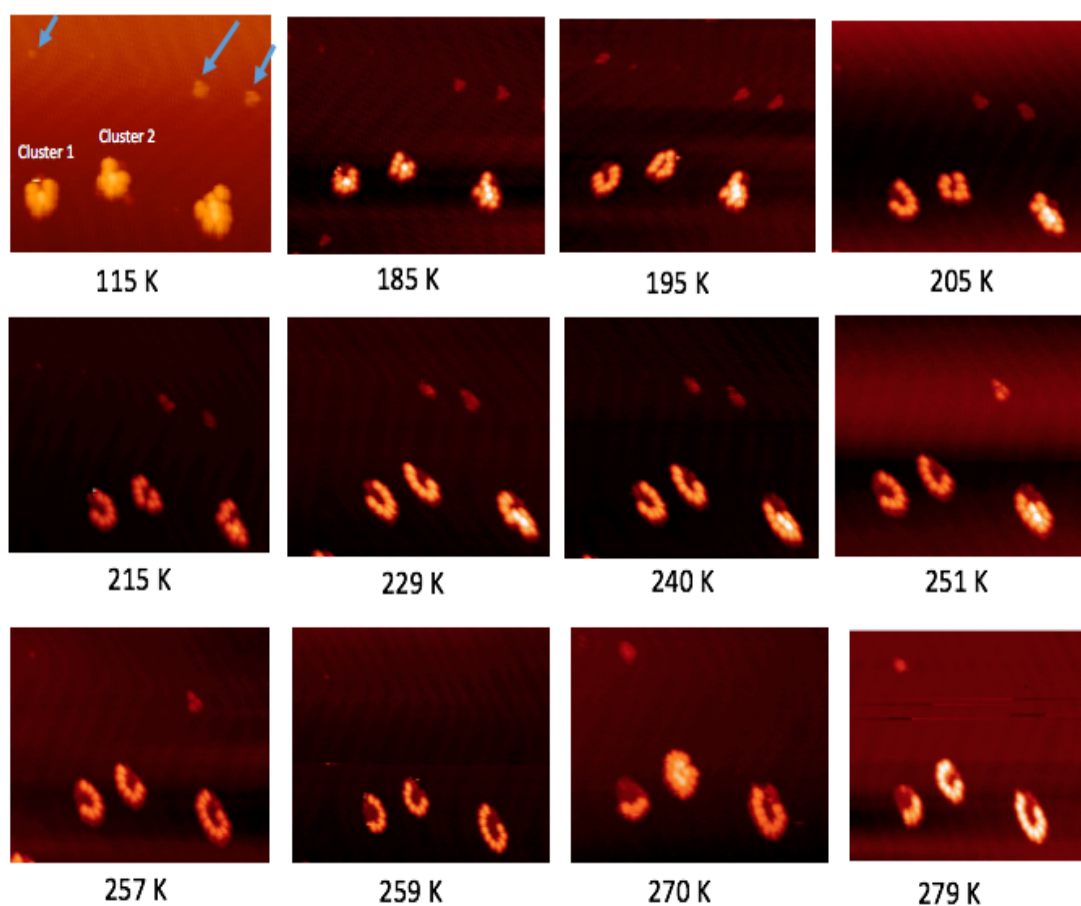


FIGURE 5.10: Clusters with extra Au atoms deposited at LT were imaged from 115 K up to 279 K, showing how the structures have opened and formed ring patterns. On empty elbows Au islands can be observed which are indicated by blue arrows. These islands are stable up to about 260 K, after which they decompose and join existing structures.

is an effect of extra Au atoms merging into the central Au islands. Based on the grouping explained before, such structures, agree with the second type suggested. As the temperature increases, fullerene molecules on top of the Au islands come down to join the step edges where the bonding is stronger. At 270 K, cluster 1, lost 3 of its fullerene molecules and the neighbouring structure gained another 9, leaving it with 16 molecules in total. This was expected as molecules from other broken clusters have enough energy to move freely on the surface until they reach and attach to other structures. However, since the resultant cluster has not reached the thermodynamically stable form, when the temperature was increased

to 290 K, it opened up to form a ring structure. The other point noticed was the growth of Au island sizes from 115 K to 279 K.

Apart from clusters, at 115 K, single layer Au islands were observed on empty elbow sites as highlighted by the blue arrows in figure 5.10. At higher temperatures, atoms in Au islands that do not have fullerene molecules attached around their steps gain enough energy to overcome the surface potential at elbow sites. As a result, at about 240 K, Au islands start to disappear from their positions. The resulting free atoms on the surface can then be captured by open structures, helping to increase their size or reach step edges. The change in the size of the Au islands with respect to temperature (for clusters 1 and 2 in figure 5.10) is shown in figure 5.11 below.

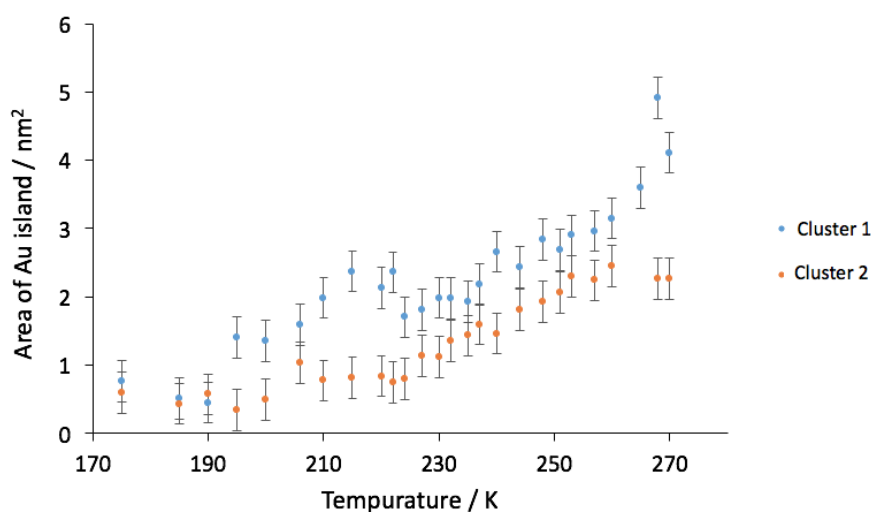


FIGURE 5.11: Variation in Au island size (measured from two clusters labelled in figure 5.10) with respect to the temperature. The error bars are based on standard deviation of measurements.

Based on graph 5.11, the Au island sizes measured from cluster 1 and 2 were initially comparable since they were both $(C_{60})_7-(Au)_{19}$. As the temperature was increased, the Au island size also increased. However, above 230 K, the rate of change in cluster size tended to grow. This can be explained by the release of Au atoms from empty elbow sites that join the ring structures.

It is also worth noting that C_{60} molecules start to move around on the surface from 190 K while Au islands are stable up to ~ 250 K. The greater stability of the Au islands make production of new clusters possible. So apart from formation of ring structures, subsequent deposition of Au atoms can also result in enlargement of existing clusters or creation of new ones. An example of cluster enlargement is shown in figure 5.12.

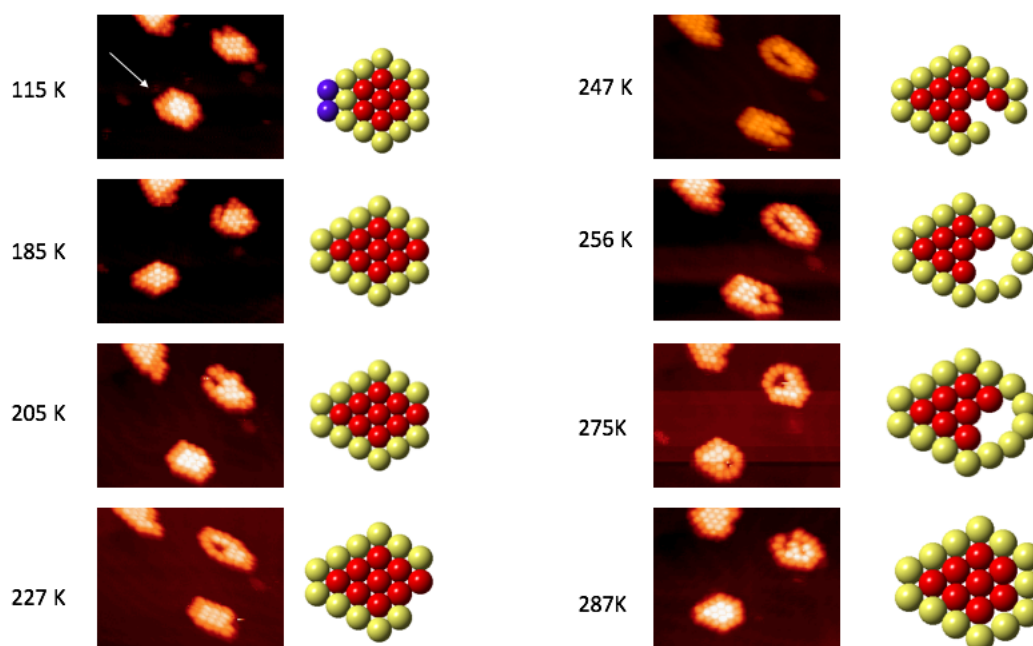


FIGURE 5.12: The effect of increasing temperature on stable $(C_{60})_m-(Au)_n$ clusters after deposition of Au atoms is examined. A $(C_{60})_{19}$ cluster with two extra C_{60} molecules, shown by the white arrow, has grown to a $(C_{60})_{21}$ as a result of extra Au atoms available on the surface. On the right hand side of each image a model for the cluster is presented, where yellow molecules correspond to atoms sitting around the Au island step edges, red are molecules positioned on top of the Au islands and blue are extra molecules.

Figure 5.12 shows an example of a cluster growing in size as a result of Au deposition at low temperature followed by slowly increasing the temperature to RT. In this case, the cluster of interest is indicated by a white arrow and the model next to it shows its structure. In the model provided, yellow spheres denote C_{60} molecules attached at step edges, while red ones denote molecules on top of the Au island and blue spheres denote extra molecules around the cluster. At 115 K, gold

atoms are sitting next to the fullerene molecules. As the temperature is increased to 185 K, extra Au atoms join the existing island at the centre of cluster. As a result of this, the number of C_{60} molecules on top of the Au island increases from 7 to 9 molecules. However, there are not enough molecules available to form a stable cluster. Therefore, C_{60} molecules are free to move around the structure until the temperature reaches 247 K whereupon two of molecules have moved down and joined the step edges of the Au island. At this point their binding is strong enough to minimise the probability of molecules moving back on top of the island. By increasing the temperature further, molecules and atoms can move around the structure until they reach the thermodynamically stable form of $(C_{60})_8$. Movement of molecules observed after 247 K could be due to the Au island losing some of its atoms while the temperature is increasing. However, STM doesn't provide any information regarding the underlying Au, so confirming it is not possible.

In order to have a better understanding of the overall effect of the deposited Au atoms on the range of clusters formed, a sample of 300 clusters were counted before and after deposition. The graph shown in figure 5.13 summarise the results obtained.

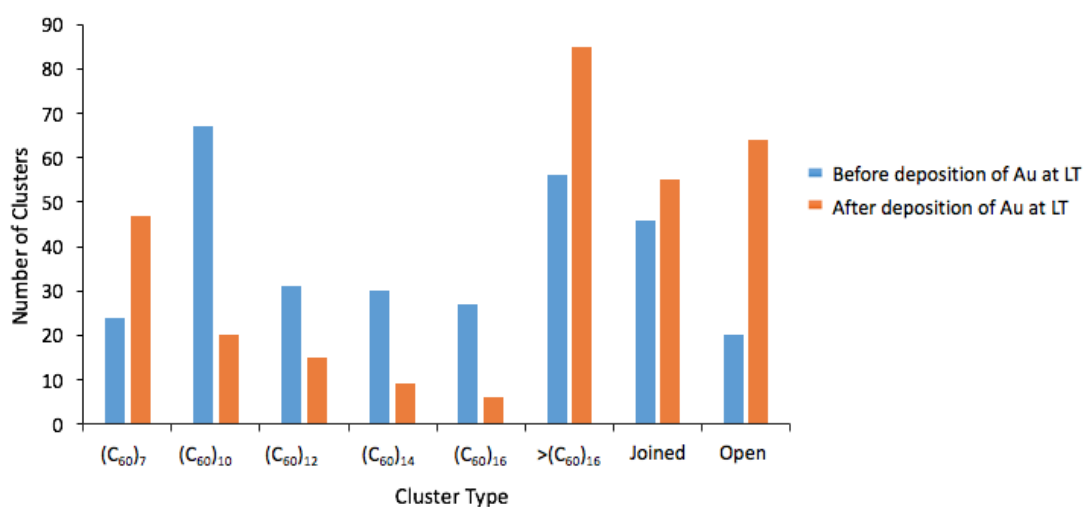


FIGURE 5.13: Comparison between ranges of clusters formed on the surface at room temperature, before and after deposition of Au atoms.

As expected, the number of open structures observed has increased. This could be due to opening of stable clusters as shown in figure 5.10, which coincides with the reduction observed in most sizes of stable structures. Another change observed is the increase in clusters with more than 16 fullerene molecules, $> (C_{60})_{16}$. This is a result of Au atoms being successfully added to a cluster and increasing its size, like the example shown in figure 5.12. It is also possible for the Au islands formed on empty elbows to capture fullerene molecules and form a stable structure. Since the amount of Au deposited is very small (0.03 ML), most of the clusters formed are expected to be $(C_{60})_7\text{-(Au)}_{19}$. This explains the increase in the population of these clusters after deposition of Au atoms.

5.4 Addition of C_{60} Molecules to Stable Structures at LT

The effect of depositing C_{60} molecules on stable structures at low temperature was also examined. As described in the previous section, a sample with a high coverage of C_{60} -Au magic clusters was prepared and cooled down to 115 K for deposition of fullerene molecules. Figure 5.14 shows a surface at 115 K after depositing 0.07 ML of C_{60} molecules. It can be seen that a few elbows have been decorated with a single C_{60} molecule (as marked by white arrows), but in most cases fullerene molecules have decorated pre-existing structures. On average each cluster has 7 extra fullerene molecules around it. Table 5.1 shows how many extra fullerene molecules have been attached to each cluster with their average values. These molecules are arranged along the fullerene R30° close pack directions.

As the temperature is increased extra molecules around the edges start to move away from clusters. By 250 K about 70 % of the clusters have lost their extra molecules. These free molecules can then be captured by other clusters and form

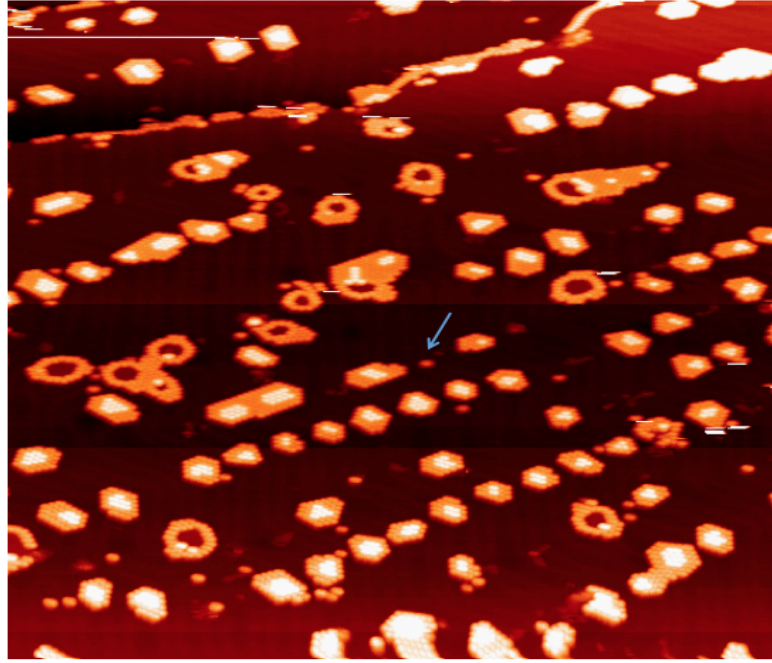


FIGURE 5.14: Scan obtained at 110 K after deposition of 0.07 ML of C_{60} onto stable $(C_{60})_m-(Au)_n$ structures. Almost all of the fullerene molecules deposited have joined and extended islands around magic clusters. A few single fullerene molecules have been captured by elbow sites, one of these molecules is highlighted by the arrow. 119 nm \times 119 nm, $V = -2.27$ V, $I = 0.05$ nA.

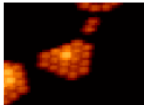
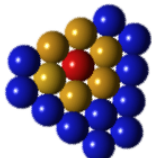
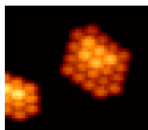
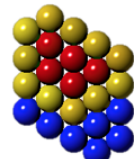
$(C_{60})_7$	$(C_{60})_{10}$	$(C_{60})_{12}$	$(C_{60})_{14}$	$(C_{60})_{16}$	$(C_{60})_{18}$	$(C_{60})_{19}$	$(C_{60})_{21}$	$(C_{60})_{23}$	
6	3	9	2	5	10	2	9	6	
8	3	6	10	6	12	10	10	10	
11	6	4	4	3	4	2	14		
	8	11	5	11	7	15			
	4	4	4	7	5				
	3	5	2	12	11				
	6	8	4	8	6				
		9	5	6	8				
			7						
Average:									
8	5	7	5	7	8	7	11	8	

TABLE 5.1: Number of extra C_{60} molecules counted on different structures with their average values are presented. On the right hand side of table two examples with their models are shown, where red spheres represent C_{60} molecules sitting on top of Au islands, yellow sphere are molecules positioned next to the step edges and blue spheres are additional molecules.

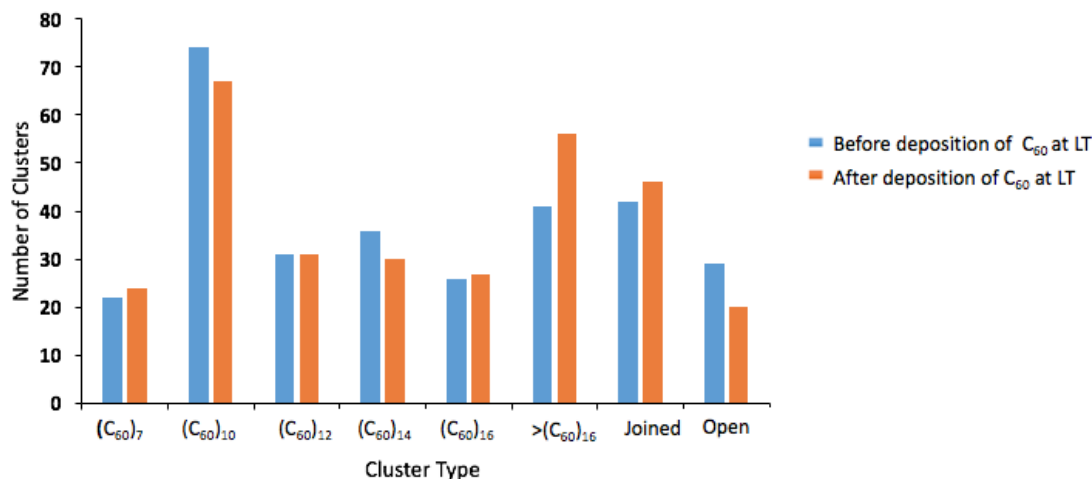


FIGURE 5.15: Size distribution of clusters before and after deposition of C_{60} molecules at 110 K. Results obtained suggest no major changes.

joined structures. To check the overall behaviour, a sample of 300 clusters were counted before and after the deposition of fullerene on the surface. The results obtained are presented in figure 5.15. As can be seen, there is not a significant difference in the cluster population before and after deposition. This indicates that the extra fullerene molecules do not play a major role in defining the size of the clusters. As shown earlier, the amount of Au deposited is the main parameter in defining their sizes.

5.5 Summary

By studying the position of the clusters under various deposition and annealing scenarios it has been shown that both types of elbows can be accommodated by structures. Based on earlier works, annealing the sample to 350 K can help to move structures from bulged to pinched elbows where the fcc areas of the surface reconstruction is larger. The challenge was to find conditions where the structures were organised on bulged elbows only. Here it is shown that after deposition of Au atoms at 110 K and annealing them at 180 K, atoms would have enough kinetic

energy to move from hcp to fcc sites. Heating the sample for 2 hours at 180 K results in almost complete removal of pinched islands. The resulting atoms can be combined with the existing structures on bulged elbows. This was confirmed by measuring the area of islands before and after annealing, which showed an increase of $\sim 0.5 \text{ nm}^2$. The measured size of the islands tends to increase up to 250 minutes of annealing, after which no major change in cluster size was detected. At this point the amount of Au atoms lost by islands is comparable to the amount gained by them. Once formation of structures on bulged elbows was confirmed, deposition of fullerene molecules at 150 K can help to produce clusters at these sites only. It is also possible to deposit more Au atoms after annealing the surface. Repeating these cycles can help in controlling the size of Au islands as well as the range of $(C_{60})_m\text{-(Au)}_n$ clusters obtained on elbows.

To understand the effect of Au on cluster growth, Au atoms were deposited on the stable structures at 110 K. Extra atoms on the surface can form islands next to the existing clusters or join their central Au island to open up the structures. It is also possible to have both cases occur on the same cluster. By increasing the temperature, the structures can open up to form a ring or adsorb free fullerene molecules and reach a larger magic cluster size. The other observation made at 110 K, was the formation of Au islands on empty elbow sites. These islands can also adsorb free C_{60} molecules to form new stable structures.

Finally, the effect of depositing additional fullerene molecules at low temperature on stable clusters was investigated. The results obtained showed that most of the fullerene molecules reach and form islands around the magic clusters. These fullerene molecules are not attached to the Au step edges; instead they are bonded to other fullerene molecules through vdW interaction. Therefore, increasing the temperature can result in the removal of extra molecules on more than 70 % of clusters by 250 K. These results agree with earlier findings that identified Au island area as being the main parameter in defining $(C_{60})_m\text{-(Au)}_n$ cluster sizes.

Chapter 6

Sputtering of C_{60} /Au surface

6.1 Introduction

Fullerenes and especially C_{60} molecules have been extensively investigated due to their wide range of applications. Some of these studies focused on altering the properties of the molecules using different techniques such as sputtering. Studies of the sputtering and fragmentation of molecules helped to answer question regarding stability [163] and possible modification of their properties during the production of new structures [164]. In most of these experiments molecules were bombarded in the gas phase. Here we have studied the effect of low ion energy sputtering of C_{60} supported on Au (111) surface, after looking at effects of sputtering on bare gold surfaces.

6.2 Sputtering of Au Surface

There has been a range of sputtering investigations on the Au (111) surface. One of the earliest works was performed by D. Cherns [154], where an Au foil was sputtered by 1 MeV electrons in a transmission electron microscope (TEM). They

studied the etch pits formed and their movement towards step-down edges by annealing the surface up to 450 K. Since then, effect of sputtering by different beams from Au clusters [165] to noble gases [140, 166] on Au (111) surfaces have been investigated. One of the most commonly used gases is argon. Ar ion beams with energy of a few eV to tens of keV are used for patterning, cleaning or depth profiling of surfaces [129]. Here, the results obtained from analysing the Au surface after sputtering for 10 second at different beam energies (between 700 eV to 1200 eV) are presented.

The sputtering procedure was as follows; the sample was placed on a manipulator that was then rotated away from the ion source. Once the pressure inside the chamber reached $\sim 8 \times 10^{-6}$ mbar, which was the nominal pressure for operating the ion source, the sample was then rotated towards the Ar gun for 10 seconds. During this time sputtering current was also recorded. Figure 6.1, shows an example of the Au (111) surface after being bombarded by Ar ion beam with energy of 700 eV and 1200 eV. The current density during sputtering was $20 \mu\text{A}/\text{cm}^2$.

In figure 6.1A, monolayer etch pits of various sizes are observed. This is confirmed by the height profile across the blue line. You might note that room temperature is sufficient to anneal out the damage caused by the sputtering, resulting in the hexagonal etch pits. The structures formed are bounded by two kinds of steps; they can show {111} or {100} facets when moving on the surface. Due to the difference in formation energy of them, pits observed may not have perfect hexagon structures [133]. As explained previously, steps with {111} facets have lower energy due to their higher atomic density which makes it the dominate type that is formed [56].

The size distribution of the etch pits was measured to characterise the effect of the beam energy on the surface. It has already been shown that sputtering at very low ion doses creates etch pits with relatively uniform size distributions. As ion dose increases formation of new holes starts to compete with the removal of Au atoms from existing ones, and so a wider range of structures will be obtained

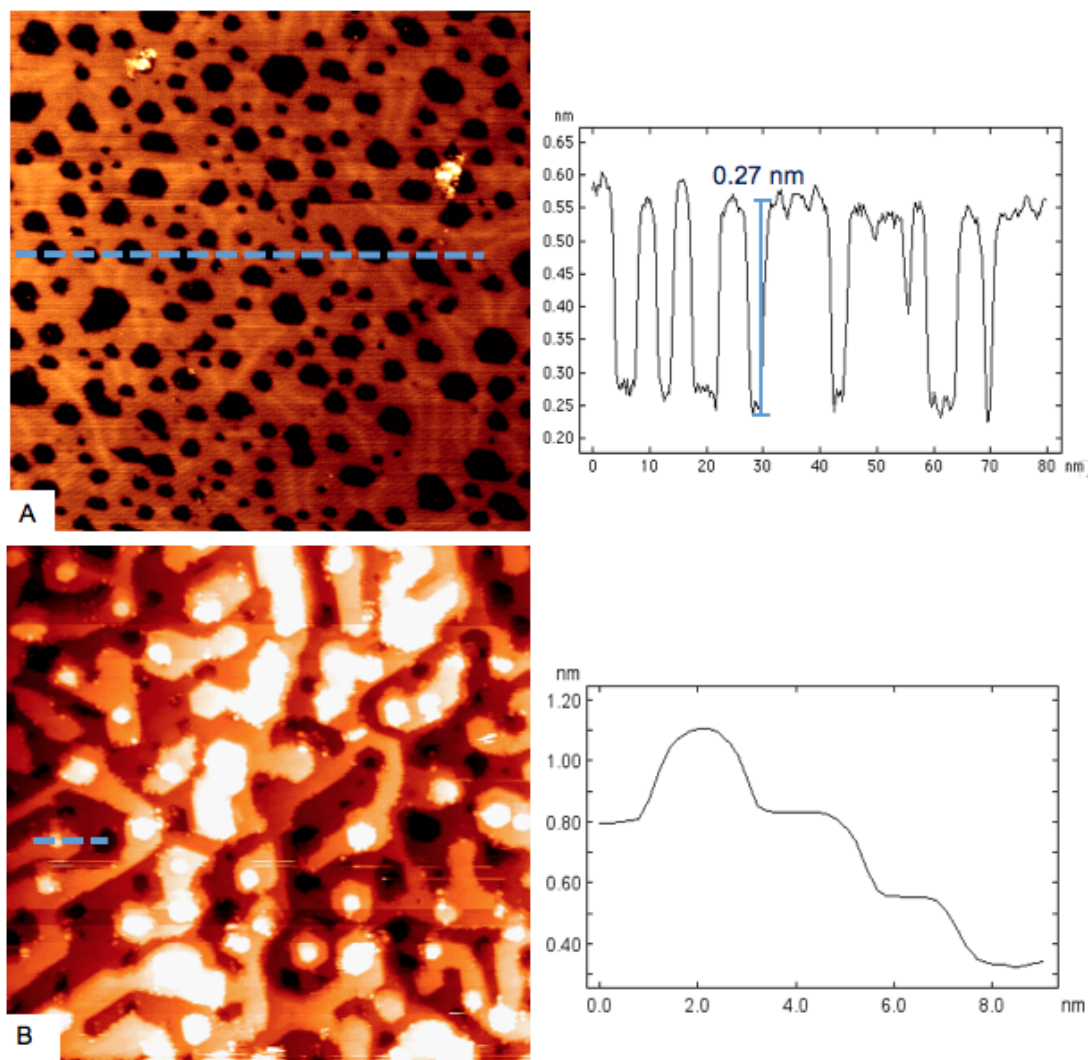


FIGURE 6.1: A) Surface after being sputtered with 700 eV beam for 10 seconds at room temperature. $88.3 \text{ nm} \times 88.3 \text{ nm}$, $V = -1.58 \text{ V}$, $I = 0.05 \text{ nA}$. B) After increasing the ion beam energy to 1200 eV, the surface layer is almost completely removed and sputtering of the third layer was observed. $72.6 \text{ nm} \times 72.6 \text{ nm}$, $V = -2.09 \text{ V}$, $I = 0.04 \text{ nA}$. On the right hand side the height profiles corresponding to the blue lines in each image are presented.

[167]. Figure 6.2, shows a histogram of the size distribution of monolayer etch pits obtained using two different beam energies.

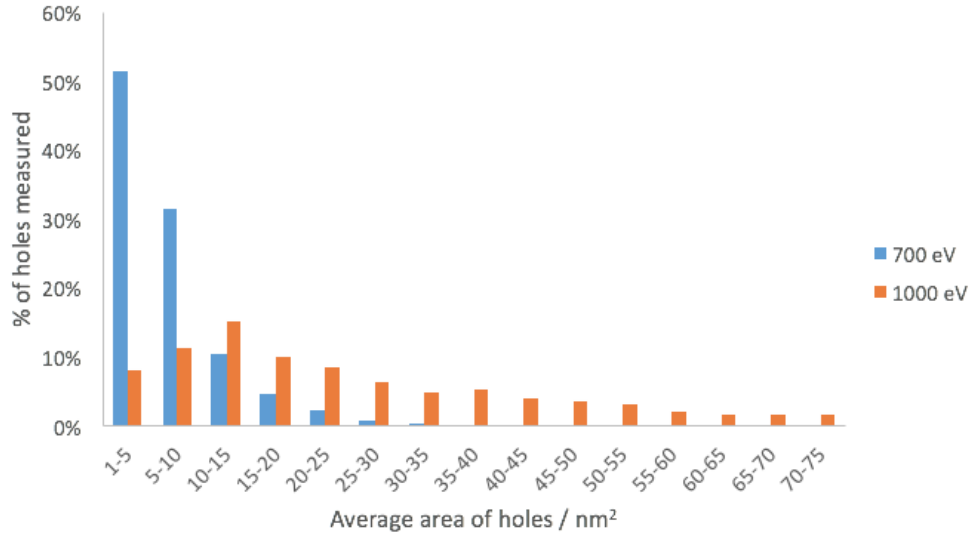


FIGURE 6.2: Histogram of pits areas at beam energies of 700 eV (blue bars) and 1000 eV (orange bars).

Based on this histogram, for a beam with energy of 700 eV (blue bars), the number of etch pits observed decreases as their average size increases. Once the energy raised to 1000 eV (orange bars) a wider range of size distribution was obtained. Also, the position of the peak has changed from 1-5 nm² to 10-15 nm² that indicate an increase in mean size of the vacancy islands too. This pattern agrees with observation of larger and more polydisperse structures at higher energies due to the coalescence of smaller pits [167].

Further increasing the sputtering energy, results in the removal of even more material from the surface; as well as formation of multi-layer pits. Figure 6.1B is an example of a surface after being bombard with Ar ion beam of 1200 eV energy. On the right hand side, graph corresponding to the blue line is presented that agrees with the sputtering of third layer at 1200 eV.

Creation of pits can also have an effect on the reconstruction patterns. Figure 6.1A, shows an example of DLs being affected by sputtering as a result of the break up in the uni-axial nature of the surface strain. During sputtering one or a few atoms are removed from the surface. This is done independently from the reconstruction pattern. As the pits join and form larger stable holes, the reconstruction pattern is modified due to changes in surface strains. In figure 6.1B, the step density have substantially increased and correspondingly reduced the average terrace width between steps. Relaxation along the steps allows the surface stress to be lifted so that reconstruction doesn't form [55].

In order to have a better comparison, the average area of the holes formed on the surface, as well as the total area removed as a function of Ar beam energy was measured and the results are presented in figure 6.3. Orange data points correspond to the surface area removed that agrees with more gold atoms being detached at higher energies as observed from scan areas. Data points presented in blue show the average area of the etch pits formed at each energy with error bars on these points being the standard deviation of average values. The results show that although initially the average value has not increased much, a wider range of structures are formed that resulted in the larger errors bars.

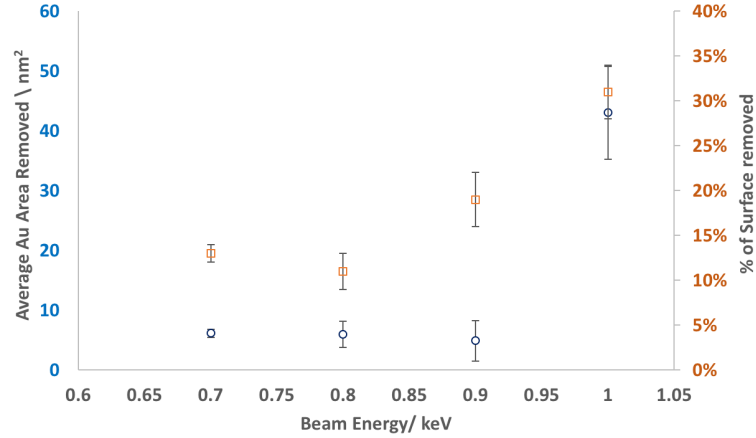


FIGURE 6.3: Percentage of area removed as well as average area of pits are presented with orange and blue respectively. As energy increases, the amount of Au sputtered from surface as well as the area of pits formed increases. Error bars obtained are based on the standard deviation of values measured from different scan areas.

In graph 6.3, 1 keV was chosen as the upper limit. Above this value, it is not possible to identify the original terraces and step edges on the surface. From the observed changes in surface morphology, it was possible to calculate the sputtering yield.

6.2.1 Sputtering Yield Calculation

The modified Bohdanský equation introduced earlier was used to estimate the sputtering yield. Based on the atomic charge and masses of the argon and gold as well as the binding energy of the Au atoms (3.8 eV [168]) the sputtering yield curve versus energy was plotted in Matlab. As mentioned earlier, the parameter “Q” in this equation is used to fit the curve to the data obtained. In order to do so, the results for a range of different sputter energies were plotted and the value of “Q” was selected as 30 to fit the curve to the data points. Figure 6.4 shows the estimate curve.

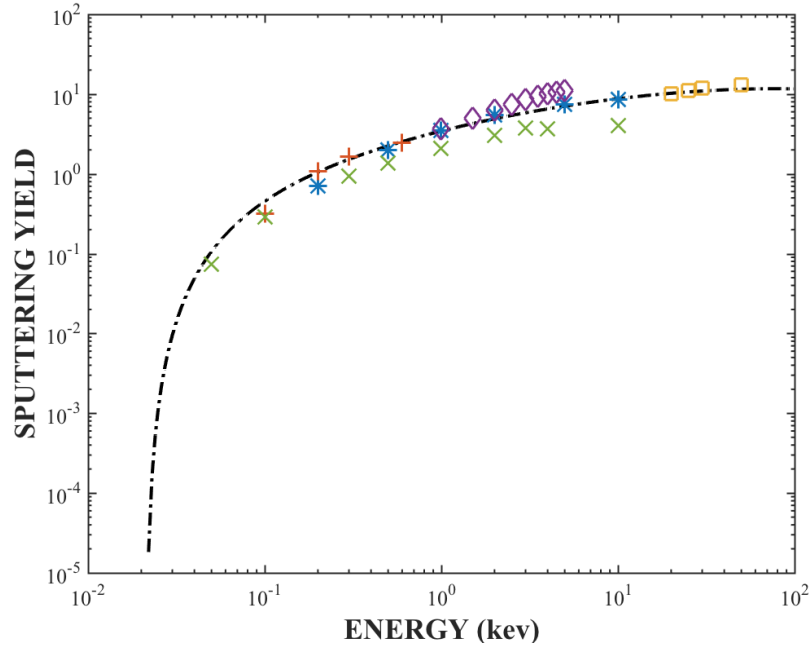


FIGURE 6.4: Different colours correspond to the data obtained from Ar ion sputtering of Au (111) at different energies by different groups. Results indicated by orange pluses are from [169], blue stars are from [170], green crosses are from [132], purple diamonds are from [171] and yellow squares are from [172].

The data points presented in this figure were reported by different groups [132, 169–172]. Once the graph was plotted sputter yield values for the energies used in this report can be estimated. Figure 6.5 shows the zoomed in section of interest where the values of the sputtering yield for the energy ranges examined is about 2.7–3.7 Au atoms per Ar ion.

The sputtering yield can also be estimated based on the sputtering parameters used. By knowing the current ($I = 10 \mu\text{A}$) and sputtering time ($t = 5 \text{ s}$), the total charge used can be calculated ($q = I.t$). Dividing this value by charge of an electron will give the total number of Ar ions incident on the surface. For a sample with size of $(1.0 \times 0.5) \text{ cm}$, the total number of gold atoms removed by each argon ion was estimated to be about 4 atoms. This value is also in agreement with results obtained from the curve. The code used for plotting figure 6.4 is presented in the appendix B.

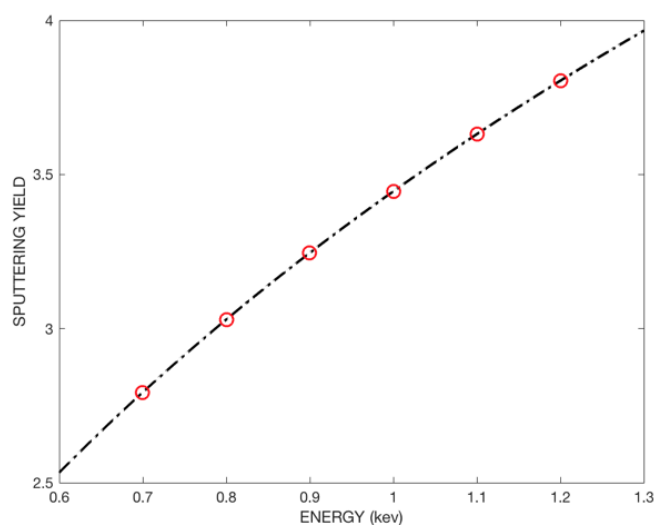


FIGURE 6.5: Sputtering yields for the energy values used in this study from the fitted curve in figure 6.4.

6.3 Sputtering of C_{60} on Au

After examining the effect of sputter damages on the Au (111) surface, the sputtering of C_{60} islands on the surface was studied. To do so, a sample was prepared by deposition of 0.4 ML of C_{60} molecules on the Au (111) surface at RT. During deposition, the evaporators temperature was set to about 410 °C with a base pressure of $\sim 3 \times 10^{-8}$ mbar. Having partial coverages of C_{60} on the surface allows the height of molecules to be measured and compared. Examples of the surface obtained, after C_{60} deposition, are shown in figure 6.6 with the close pack direction of the C_{60} islands highlighted in the image.

Once formation of islands on the surface was confirmed, the sample was placed on the manipulator and Ar sputtered for 5 second with beam energy of 1 keV. This energy was chosen to produce the damage to the surface layer of the Au as well as the fullerene molecules without completely destroying them. The total destruction of the fullerene molecules in the gas phase has been shown to require a few hundreds of keV, so at this energy slight damage to some of the molecules is expected [173]. Figure 6.6B shows a scan of the surface obtained after sputtering.

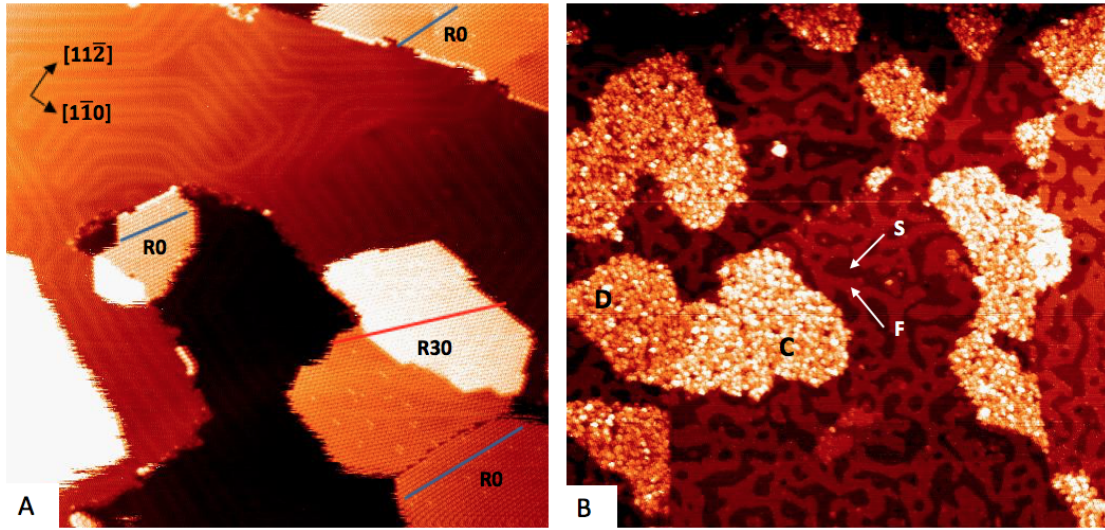


FIGURE 6.6: A) Formation of different C_{60} islands on the Au (111) surface, with their close pack directions marked. $120.62 \text{ nm} \times 120.62 \text{ nm}$, $V = -1.37 \text{ V}$, $I = 0.05 \text{ nA}$. B) Scan obtained after Ar ion sputtering of the surface with a beam energy of 1 keV for 5 seconds . In figure B, area marked as “F” shows the top layer of gold surface, “S” is the second layer, “C” and “D” are the C_{60} islands formed on the upper and the lower side of the step edge respectively. $227.62 \text{ nm} \times 227.62 \text{ nm}$, $V = -2.6 \text{ V}$, $I = 0.05 \text{ nA}$.

In this scan, the area marked as “s” represents the top Au layer while “F” indicates the second layer that has become apparent as a result of partial removal of the surface. From different scans obtained the total area removed was estimated to be about 28 % of the surface. Other areas marked in this image are “C” and “D”, which correspond to the C_{60} islands on the upper and lower sides of step edges respectively. In the observed islands, the brighter points are believed to be the broken fullerene molecules. This change in contrast is a result of the higher LDOS measured by the tip over open molecules. Apart from the electronic properties, the contrast can also be physical height difference measured over the molecules fragments on the surface.

On average each C_{60} molecule can be targeted by two ions that can interact with the molecules or pass in between them to reach the Au surface. The ions can damage molecules in two different ways: the direct nuclear collision or by changing the electronic structures of the molecules which can result in coulomb explosion.

In the present case, the most common type of fragmentation is expected to be the direct collision as the electronic mechanism is less efficient in thin films [174].

Roughening of the C_{60} island edges was another effect of sputtering. At this stage three possible scenarios can be considered. It could be a result of changes in the under layer Au or local annealing of the surface due to the energy transferred that results in molecules on edges to move away and join other islands. Finally it can be explained as trapping of the molecules between the broken C_{60} cages. After sputtering, random distribution of the damaged molecules was observed. Due to the existence of dangling bonds in these molecules, formation of stronger bonding with the Au surface or other broken cages are possible. Limitation in movement of linked fullerene cages, like C_{120} , was previously reported [175]. In this case, movement of damaged C_{60} cages on the surface is expected to be limited and any C_{60} molecules trapped between them cannot move freely either.

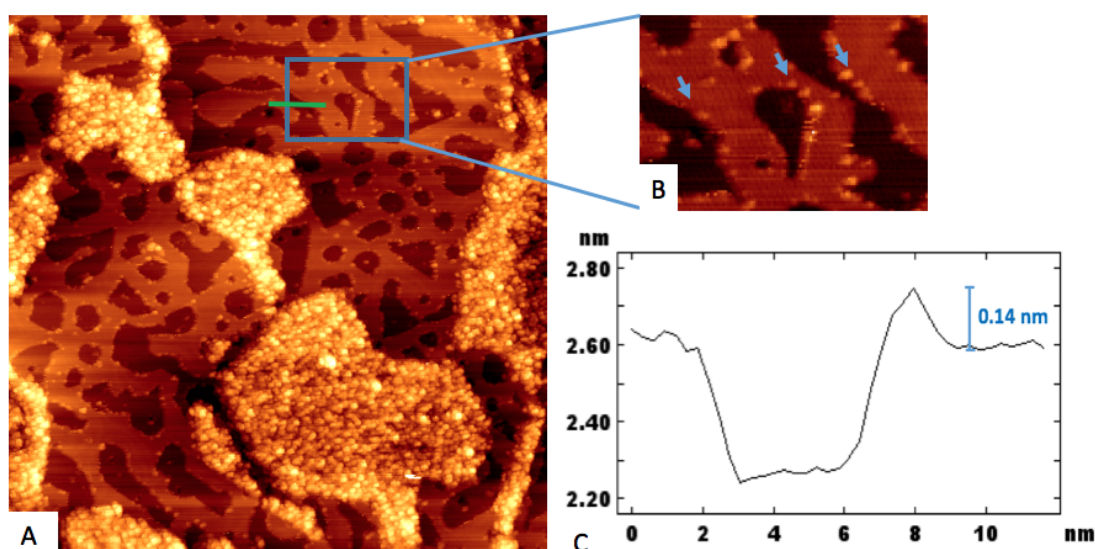


FIGURE 6.7: A) After sputtering the C_{60} /Au (111) surface, fullerene islands were roughened. $157.3 \text{ nm} \times 157.3 \text{ nm}$, $V = -2.6 \text{ V}$, $I = 0.05 \text{ nA}$. B) Carbon islands were also formed on the surface from breaking of molecules. An example of this is highlighted by blue arrows in the zoomed in section. C) Graph C shows the height profile across the green line. The height measured ($\sim 0.14 \text{ nm}$) agrees with the expected value for the diameter of the carbon atoms 0.15 nm [76]).

After sputtering, small islands and atoms have been observed on the surface and at the step edges of Au. From 6.7C, the height of these features was measured to be ~ 0.14 nm, which agrees with the value expected for the diameter of carbon atoms (0.15 Å [76]). So, it can be concluded that these islands are carbon fragments of broken C_{60} molecules. Examples of these atoms are highlighted by blue arrows in figure 6.7B.

6.3.1 Annealing Sample

In order to examine the effects of temperature on the surface, the sample was annealed in the STM stage by resistive heating using PBN plate of the holder. During preparation the resistance of the sample holder was measured to be $7.2\ \Omega$ before being inserted into the chamber. Using this value and a calibration curve of power versus temperature provided by the manufacture, the current required to reach the desired temperature was estimated. The STM allows for resistive heating to temperature of up to 750 K while scanning. In order to avoid possible damage, the sample was only annealed up to 700 K during scans. For higher temperatures, the manipulator was used for heating the sample before placing it into the STM to be scanned.

The first signs of change in the surface topography were observed at ~ 350 K where the etch pits start to join. Examples of scans at higher temperatures are shown in figure 6.8.

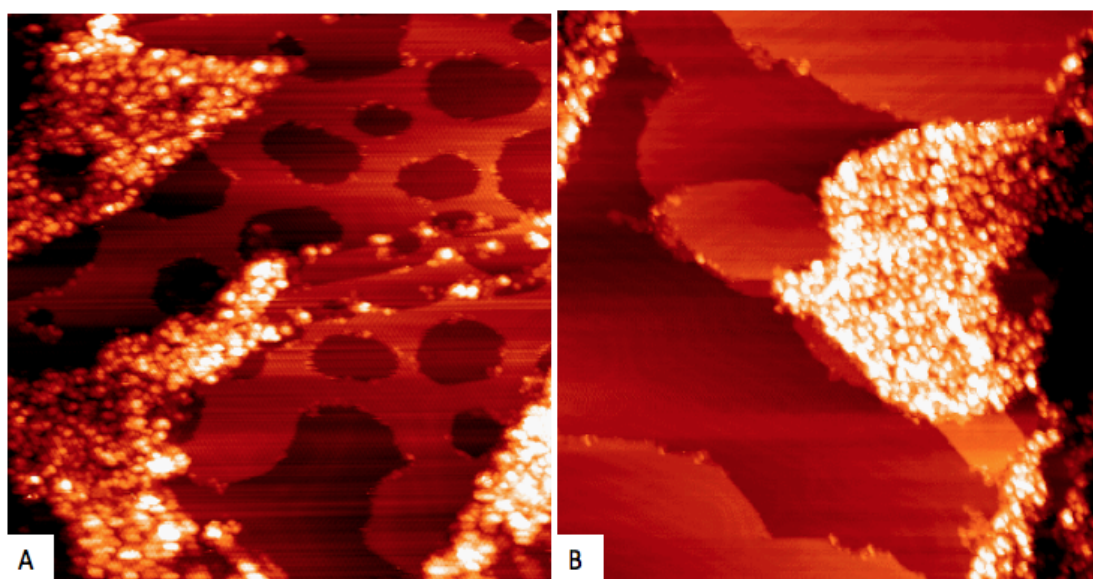


FIGURE 6.8: A) The sputtered C_{60} on Au (111) sample was annealed on STM stage at 355 K. At this temperature, etch pits in the Au surface start to merge and grow in size. $72 \text{ nm} \times 72 \text{ nm}$, $V = -2.05 \text{ V}$, $I = 0.03 \text{ nA}$. B) The temperature was then slowly increased further to 573 K. At this temperature all smaller holes on the surface have coalesced. $103 \text{ nm} \times 103 \text{ nm}$, $V = -1.28 \text{ V}$, $I = 0.05 \text{ nA}$.

Figure 6.8A shows the sample at a temperature of 355 K. The average area of the etch pits has increased ($58 \pm 28 \text{ nm}^2$) in comparison to the pits formed after sputtering the surface at room temperature ($34 \pm 29 \text{ nm}^2$). The error was calculated from the standard deviations on the measurements made. Vacancies at this temperature tend to have a more uniform size distribution as indicated by the smaller percentage error measured for each value.

A further increase in temperature provides enough energy for the etch pits to completely join and form terraces. An example of this is shown in figure 6.8B, which was obtained at 573 K. The temperature was then further increased to help the Au surface fully heal. Examples of surface areas at higher temperatures (620 K and 720 K) are shown in figure 6.9.

In figure 6.9A, the area marked with red circle shows an open section. Such areas are created due to the step edges being passivated with carbon atoms. In order

to remove these holes, higher temperature or a longer annealing time is required. In contrast, the scans reveal that the C_{60} islands have not changed much during the annealing process. However, some carbon atoms on the surface have joined to form islands. A carbon island is shown in figure 6.9A by the blue circle. Formation of carbon dendritic islands on Au (111) surface was reported by S. Nie et al [176]. However to obtain a graphene layer sample should be annealed at about 950 °C. The height of island observed in figure 6.9A was measured to be ~ 0.2 nm. This confirms that structures obtained are not graphene but are rather formed from joining of carbon fragments.

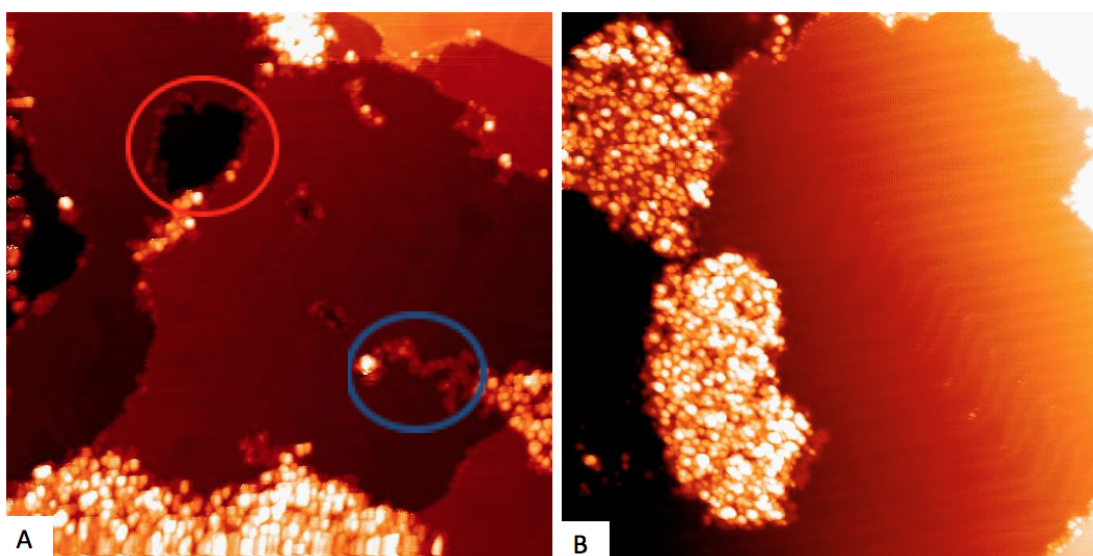


FIGURE 6.9: Scan A shows an area of the surface after being annealed to 620 K. The red circle in this image shows an uncovered section of the surface that has been passivated by carbon atoms, while blue circle shows a carbon island formed by the coalescence of C_{60} fragments. $91.04 \text{ nm} \times 91.04 \text{ nm}$, $V = -1.5 \text{ V}$, $I = 0.03 \text{ nA}$. B) Further annealing to 720 K for 15 minutes results in full recovery of the surface. $98.39 \text{ nm} \times 98.39 \text{ nm}$, $V = -1.6 \text{ V}$, $I = 0.05 \text{ nA}$.

Finally, the sample was annealed to 723 K. As this temperature is very close to the maximum value allowed for resistive heating in the STM stage (750 K); the process was done on the manipulator. After annealing the sample was left to cool down to room temperature before being placed in the STM stage for scanning. In figure 6.9B the sample was annealed to 723 K for 15 minutes which resulted

in complete recovery of the surface. However, no major changes in C_{60} islands were observed. On average, before annealing, each island was formed of 1440 C_{60} molecules; this is very close to the 1190 molecules measured for the average size of islands after annealing. It was also noted that, after annealing the sample, island edges remained rough. This agrees with formation of stronger bonds between broken molecules and trapping of undamaged ones. The arrangement of molecules doesn't show any difference too. In order to have better comparison, height of molecules was measured and compared. Discussion of these results are presented in the next section.

6.3.2 Structure of Fullerene Islands

The height of 450 molecules from different parts of the sample was measured with respect to the gold surface. Data obtained before and after annealing was compared to check the effect of temperature on the structures formed. The results are presented in figure 6.10. Based on these results, majority of molecules were measured to be about 0.7 nm - 0.8 nm tall both before and after annealing. These values are in agreement with the known height of C_{60} molecules on Au surfaces [20], indicating that most of fullerene molecules have not been damaged. However, after annealing a small reduction in the number of islands with 0.7 nm heights was detected. This can be due to the movement of molecules outside the scan area or removal of molecules from the surface as it is very close to the C_{60} desorption temperature.

As previously mentioned, the height of objects measured with STM may not correspond to their geometrical structure; it can also be due to a higher LDOS. So molecules that appear taller than normal are expected to be damaged and open cages. On the other hand, structures much smaller than the fullerene cages were also observed. Such structures can be carbon fragments formed on the surface.

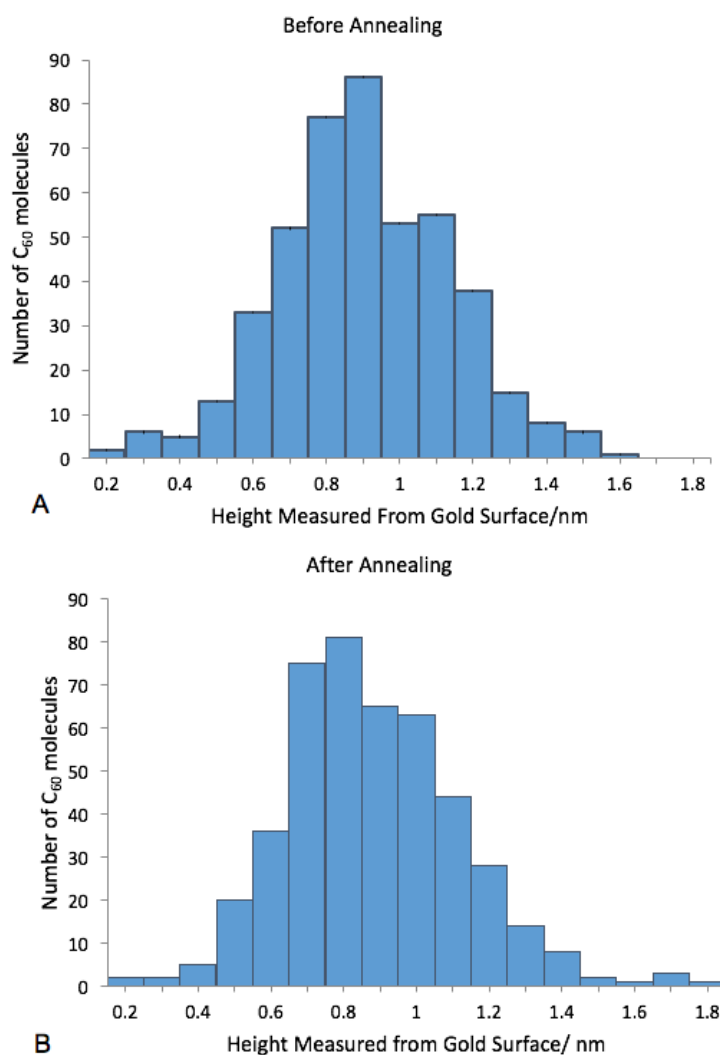


FIGURE 6.10: Height of 450 C_{60} molecules was measured before (A) and after (B) annealing the sample to 723 K.

Overall the histogram pattern has not changed during the annealing process which means no structural ordering has formed on the surface as a result of the increase in temperature. Reinkoster et al [173] have studied the fragmentation of C_{60} molecules after being bombarded with Ar ion beams at different energies using a time of flight (TOF) mass spectrometer in gas phase. The results obtained for a 1.5 keV beam are shown in figure 6.11.

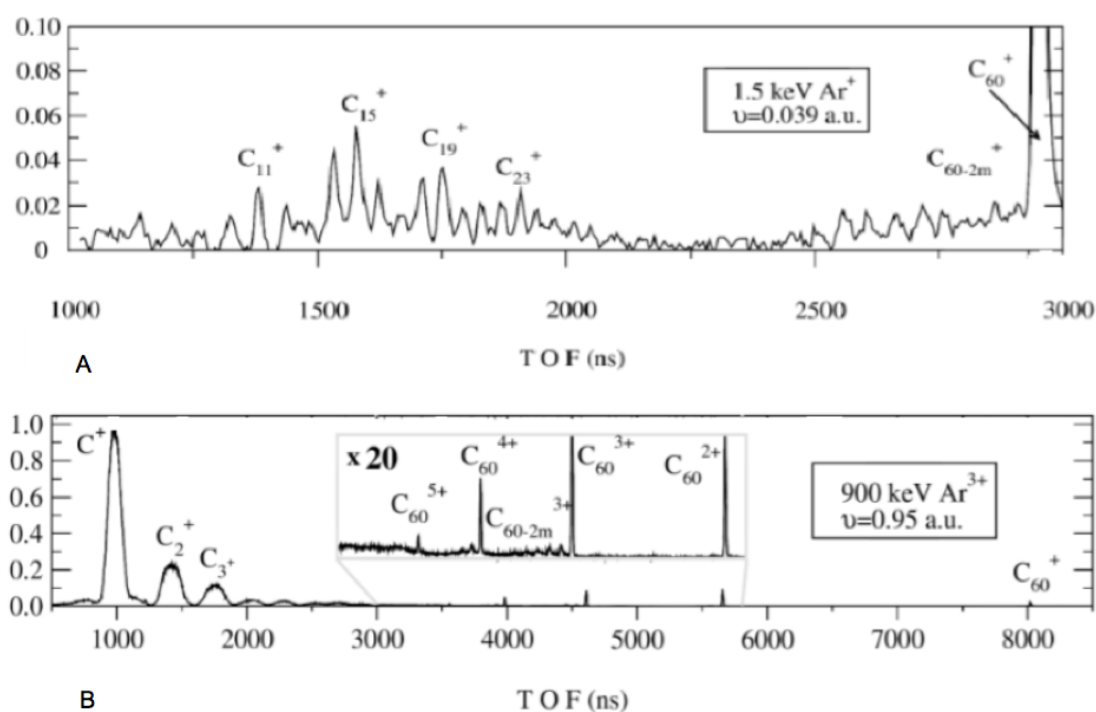


FIGURE 6.11: Time of flight (TOF) mass spectrometer data obtained at two different beam energies. A) Data obtained from the collision of the fullerene with a 1.5 keV Ar^+ beam. B) Higher beam energy of 900 keV was also used to sputter fullerene molecules [173].

In the present experiment, molecules are bonded to a surface, which can influence their fragmentation. However, based on the results presented in figure 6.11A, an Ar ion beam with 1.5 keV energy can produce a wide range of fragments. But defining what types of structures have been formed on the surface, using STM scans, is hard and requires further investigation. In order to have more uniform fragments, higher beam energies can be used. This would result in the formation of many small clusters on the surface as shown in figure 6.11B with 900 keV.

6.4 Summary

In this chapter results obtained from sputtering of Au (111) surface as well as C_{60} islands on Au (111) was studied. Ar ion beams at different energies from 700 eV to

1200 eV were used to sputter the sample for 10 seconds. For beams with relatively lower energy, wide range of hole sizes is observed on the surface. At these energies reconstruction lines are still visible on the remaining terraces but are modified due to the presence of the etch pits. As the energy was increased to 1200 eV, larger surface deformations were obtained that helped the surface to relax and remove the DLs. Sputtering at these energies resulted in uncovering areas of the third layer.

Further experiments were carried out with a sample covered by 0.4 ML coverage of C_{60} molecules. An Ar ion beam of 1000 eV energy was used to sputter this sample for 5 seconds. This ensured maximum damage to the top layer of gold while multilayer sputtering is minimised. After sputtering, about 28 % of the surface was removed with some fullerene molecules appearing brighter, due to the change in LDOS associated with broken C_{60} cages and changes in its structure. Another product of fullerene fragmentation was carbon atoms that were observed on the surface.

Based on previous studies, using low energy ion beams can result in the formation of a variety of products. However determining the exact type of molecules obtained with STM has not yet been achieved. The sample was also annealed to check the effect of temperature. As the temperature was increased, the vacancy islands started to coalesce and form larger structures. Eventually the sputter damage was annealed out and the Au surface recovered completely. However, no major changes were observed in the fullerene islands. This was confirmed by a histogram of the molecules height before and after annealing. A possible explanation can be the limited movement of broken cages that would trap any C_{60} molecules in between.

Further investigations are required to determine what molecular fragments are present after sputtering and what possible effects changes in temperature may have on their arrangements.

Chapter 7

Conclusion

Results presented in this thesis can be divided into two parts. First, a detailed study on $(C_{60})_m-(Au)_n$ magic clusters is provided. Then topographical changes of the Au (111) surface, with and without C_{60} islands, after being sputtered by an Ar ion beam is introduced. In each section samples have been investigated in UHV with an Omicron VT-STM.

Initially, the effect of different deposition parameters on the cluster size distribution was examined. Results obtained showed that Au coverage plays a major role in defining the range of structures obtained. By increasing the amount of Au available, larger clusters with wider range of sizes can be formed. For very low coverages (about 0.01 ML), an interesting phenomenon, just below room temperature (~ 270 K), was reported. At this temperature the majority of clusters (more than 60 %) formed were $(C_{60})_7$. Since these structures are not stable at room temperature it was suggested that instead of 19 Au atoms, only 7 atoms are used. This is the minimum number require to raise a C_{60} molecule. The other point noticed was the formation of such clusters mainly on bulged elbow sites. The preference of this elbow is due to the larger Au islands that form on their fcc areas in comparisons to the ones on hcp sites of pinched elbows. This slight

increase in islands size as well as being positioned on fcc areas, which has lower surface potential, makes structures at these positions more stable.

After Au, fullerene coverage was the next parameter to be studied. Variation in the density of C_{60} molecules did not show a major effect on the size range of clusters formed. Instead a change in the percentage of ring structures was observed. When the amount of fullerene molecules on the surface is not enough to cover Au islands and form magic clusters, ring structures are obtained. In this case molecules decorate step edges of islands where bonding is stronger. On the other hand, for high coverages of C_{60} molecules, a higher percentage of joined clusters is observed. For these clusters, fullerene molecules fill the gap between two neighbouring structures to form a joined cluster. Therefore, the percentage of ring and joined structures can be an indication of the Au/ C_{60} ratio being high enough to reach the stable forms.

Production of clusters with C_{70} molecules were also examined to check the effect of its rugby ball shape on the structures observed. As suggested by literature, their preferred orientation is to have the long axis perpendicular to the surface. In this case, the diameter of molecules parallel to the surface is comparable to the C_{60} . Due to their similar diameters, the same model of magic clusters can be applied to both molecules, with C_{70} molecules being taller on the Au surface compared to the C_{60} .

Finally, the effect of co-depositing Au atoms and C_{60} molecules at different temperatures was examined. Results obtained show that below 150 K no major effect was observed but once the deposition temperature is set to ~ 180 K, most of the clusters form ring structures. At this temperature Au atoms have enough energy to group together and arrange into larger islands, mainly on fcc sections of the surface. In this case, if the fullerene coverage is not increased, most of the clusters form ring structures, in contrast to LT experiments.

After studying the clusters under different conditions, controlling the position of them was the next challenge. It has been shown that by annealing the stable structures to about 350 K, it is possible to move all clusters from bulged elbows to pinched elbows with larger fcc areas. In order to have most structures on bulged elbows, the position of Au islands was successfully controlled. To achieve this, Au atoms were deposited on the surface at 110 K and then annealed for about 2 hours at 180 K. This provides enough energy for Au atoms to move from hcp areas towards fcc, with the reverse process being less likely. These atoms can then be captured by existing islands on fcc part of bulged elbows. To obtain magic clusters fullerene molecules were added to the system. Once the sample reached room temperature more than 70 % of clusters were on bulged elbows. Using this idea, the size of Au islands on different elbows can be controlled. This is done by further deposition of gold atoms on the surface after it has been annealed for 2 hours. The new atoms deposited will form islands on pinched elbows while expanding existing ones on bulged elbows. By repeating the deposition and annealing steps, the size of Au islands on bulged elbow sites can grow further while on pinched elbows they remain small.

The final study performed on magic clusters, involved further deposition of Au atoms and fullerene molecules on stable clusters at 115 K. As expected, deposition of C_{60} molecules did not have any major effect on the range of structures observed. Extra molecules that were not attached to step edges of Au islands started to move away from clusters at ~ 250 K. Once the sample reached RT no changes were observed. However, additional Au atoms deposited at LT (115 K) resulted in major changes of the clusters. At this temperature, newly added gold atoms can form islands on empty elbows or join existing stable structures. Extra atoms added to the central Au islands, can result in opening of clusters. In this case, the nearest neighbour distance of fullerene molecules increases. As a result, the ones on top of the Au islands move down to the step edges and form ring structures.

Since fullerene molecules start to diffuse (~ 180 K) at lower temperature than Au (~ 250 K), there is a probability for released molecules to be captured by newly formed Au islands and create clusters. Therefore, the major changes observed at RT was the increase in open and $(C_{60})_7-(Au)_{19}$ clusters.

The other subject that was investigated was the effect of sputtering. Sputtering is known to be one of the most effective methods of creating surface defects and templates. Here the Au (111) surface was sputtered by an Ar ion beam in different energy ranges, 700 eV to 1200 eV, for 10 seconds. Results obtained showed that, below 1000 eV, as energy increases the size of holes on the surface layer increase too. Above 1000 eV, sputtering is no longer limited to the first layer, holes on second and third layers were also observed. Using the Bohdansky sputtering yield, for the energies used, the sputtering yield was estimated to be about 4 atoms per ions. This was then followed by deposition of 0.4 ML fullerene molecules on the surface before sputtering it with an ion beam of 1000 eV energy for 5 seconds. At this energy creation of single layer vacancies on Au surfaces as well as damages to fullerene molecules were observed. These broken cages tend to appear brighter in STM scans due to higher LDOS of them. The carbon atoms removed from the fullerene cage were also observed on the step edges of the Au surface. The sample was then annealed to just below the desorption temperature of the fullerenes (~ 450 K). As a result, the gold surface recovered, while no major changes in the arrangement of the fullerene molecules and broken cages were observed. This is an indication of the stronger bindings between damaged cages with each other or the surface that cause limitation in their movements. Height measurement of molecules showed no changes or preference in the arrangement of them after annealing the surface too.

Further experimental and theoretical work can be performed based on results presented here. For magic clusters it is possible to reduce the scanning temperature to about 50 K, using liquid helium, to study their molecular structure. Electronic

properties of clusters can also be investigated using STS and theoretical investigations. Observation of clusters away from elbows in this thesis has highlighted the possibilities of having surfaces with a high coverage of clusters. This can be further investigated by producing clusters on a surface like Ag that is very compatible to the Au but does not have the reconstruction pattern.

Regarding the sputtering of fullerene molecules, identifying broken cages is the next step. This can be done using theoretical calculations. Performing experiments in an STM chamber equipped with a TOF-mass spectrometer could also help to identify products of molecules removed from the surface to analyse the molecules remained. Using a more accurate ion gun can also be helpful. By operating the ion source under a condition where each molecules only receives one ion can help to have better controle on the sample and damages produces. Long sputtering time or higher beam energy can also be used to produce graphene layers on the surface. Finally it might be interesting to deposited very low fullerene coverages on Au (111) surface at low temperature to have individual molecules on each elbow sites. By sputtering this surface it may be easier to check the effect on individual molecules.

In future the idea of creating nanostruces with only van der Waals forces can be applied to other systems. Dodecahedrane ($C_{20}H_{20}$) and carborane are two possible molecules that can replace fullerenes without forming chemical bonds. Lack of strong bindings will allow molecules to move around the existing islands and form thermodynamically stable structures. The central island can also be replaced with other metals such as Ag, or even metals with electric dipole moments. Then by controlling size of clusters the dipole moments of structures can also be controlled. Finally, the Au (111) surface can be change. The work in this thesis have shown that magic clusters can form away from the elbow sites too. Then surfaces such as Ag or graphene can replace the Au surfaces.

Appendix A

Matlab Code For The Error on Islands Area

```
%%%%%%%%%%%%%%%%%%%%%%%%%%%%%%%%%%%%%%%%%%%%%%%%%%%%%%%%%%%%%%%%%%%%%%%%%

%% This program was used to estimate the vale of error measured on Au islands
%% due to tip convolution.
%%
%% 3 set of data coverages were used

%%%%%%%%%%%%%%%%%%%%%%%%%%%%%%%%%%%%%%%%%%%%%%%%%%%%%%%%%%%%%%%%%%%%%%%%%

%% Author: Marhoo Rokni Fard, University of Birmingham

clear all
close all
clc

Data=xlsread('2.xlsx'); %Data input from excel page
c=linspace(0.1,1,6000); %Assumed range of error value

%% Experimental result for 45 s deposition
a=Data(2:131,1); %Measured areas using image-xsm
rm=sqrt(a)/pi; %Radius measured
for i=1:length(c)
    for j=1:130 %Data length
        ra(i,j)=rm(j)-c(i); %Real radius
        aa(i,j)=pi*ra(i,j).^2; %Real area
```

```

    end
    sa(i)=sum(aa(i,:)); %Sum of real area
end

%% Experimental result for 380 s deposition
a2=Data(2:297,5);%Measured areas using image-xsm from second coverage
rm2=sqrt(a2)/pi; %Radius measured 2
for i=1:1:length(c)
    for j=1:1:length(rm2) %Data length
        ra2(i,j)=rm2(j)-c(i); %Real radius 2
        aa2(i,j)=pi*ra2(i,j).^2; %Real area 2
    end
    sa2(i)=sum(aa2(i,:));
end

%% Experimental result for 190 s deposition
a3=Data(2:161,9);%Measured areas using image-xsm from third coverage
rm3=sqrt(a3)/pi; %Radius measured 3
for i=1:1:length(c)
    for j=1:1:length(rm3) %Data length
        ra3(i,j)=rm3(j)-c(i); %Real radius 3
        aa3(i,j)=pi*ra3(i,j).^2; %Real area 3
    end
    sa3(i)=sum(aa3(i,:));
end

%% C1&2

ratio=sa2./sa; % Ratio of sum of areas for two coverages (380 s/45 s)

plot(c,ratio,'linewidth',2)
xlabel('Assumed error')
ylabel('Ratio of area')

% find the right error
for i=1:1:length(ratio)
    if ratio(i)<8.45 && ratio(i)>8.43

        qq=c(i); %Find the error constant for right ratio of 0.8471
    end
end

```

```
end
end

%% C1&3

ratio2=sa3./sa; % Ratio of sum of areas for two coverages (190 s/ 45 s)
hold on
plot(c,ratio2,'linewidth',2)
xlabel('Assumed error')
ylabel('Ratio of area')

% find the right error
for i=1:length(ratio2)
if ratio2(i)<4.23 && ratio2(i)>4.21

    qq2=c(i); %find the error constant for right ratio of 0.422

end
end

%% C2&3

ratio3=sa2./sa3; % Ratio of sum of areas for two coverages (380 s/ 190 s)

plot(c,ratio3,'linewidth',2)
xlabel('Assumed error')
ylabel('Ratio of area')

% find the right error
for i=1:length(ratio3)
if ratio3(i)<2.01 && ratio3(i)>1.99

    qq3=c(i); %find the error constant for right ratio of 2

end
end
```

Appendix B

Matlab Code For Sputtering Yield

```
%%%%%%%%%%%%%%%%%%%%%%%%%%%%%%%%%%%%%%%%%%%%%%%%%%%%%%%%%%%%%%%%%%%%%%%%%

%% This program was used to fit and plot the sputtering yield of Argon on Au (111) surface.
%%
%%
%% Two method available were tested, method 1 fitted better.
%% 5 data sets has been fitted to the curve.

%%%%%%%%%%%%%%%%%%%%%%%%%%%%%%%%%%%%%%%%%%%%%%%%%%%%%%%%%%%%%%%%%%%%%%%%%

%% Author: Marhoo Rokni Fard, University of Birmingham

clearvars
close all

E_th=21.13; %sputtering thershold energy
E_0=1e-2:1:1e6; %projectile energy, unit in ev

E_TF=264323.3; %ratio of mass to charge
Q=30; %constant
eps=E_0/E_TF; %reduced energy

% Method 1: Based on Kr-C potential
Sn=(0.5.*log(1+1.2288.*(eps)))./(eps+0.1728.*sqrt(eps)+0.008*(eps).^0.1504);
```

```

%nuclear stopping cross section

Y=Q*Sn.*(1-(E_th./E_0).^(2/3)).*(1-(E_th./E_0)).^2; %sputtering yield

% Method 2: Based on Thomas Fermi nuclear stopping cross section
% Sn=(3.441*sqrt(eps).*log(eps+2.718))./(1+6355*sqrt(eps)+eps.*(6.882*sqrt(eps)-1.708));
% Y=Q*(3.441*sqrt(E_0./E_TF).*log(E_0./E_TF+2.718))./(1+6355*sqrt(E_0./E_TF)+E_0./E_TF.*
(6.882*sqrt(E_0./E_TF)-1.708)).*(1-(E_th./E_0).^(2/3)).*(1-(E_th./E_0)).^2;

% e_x0=[100,70,60,50]; %unit in ev
e_x1=[50,100,300,500,1000,2000,3000,4000,10000]; %data set 1, unit in ev
e_x2=[100,200,300,600]; %data set 2, unit in ev
e_x3=[2e4,2.5e4,3e4,5e4]; %data set 3, unit in ev
e_x4=[1e3,1.5e3,2e3,2.5e3,3e3,3.5e3,4e3,4.5e3,5e3]; %data set 4, unit in ev
e_x5=[0.2,0.5,1,2,5,10]; %data set 5, unit in ev

% e_y0=[0.3,0.11,0.09,0.03];
e_y1=[7.43e-2,2.86e-1,9.3e-1,1.38,2.1,3.03,3.72,3.68,4.03]; %Sputtering Yield 1
e_y2=[0.32,1.07,1.65,2.43]; %Sputtering Yield 2
e_y3=[10,11,12,13]; %Sputtering Yield 3
e_y4=[3.7,5,6.3,7.5,8.5,9.5,10,10.5,11]; %Sputtering Yield 4
e_y5=[0.7,2,3.5,5.5,7.5,8.5]; %Sputtering Yield 5

hold on
a = 100;
F=plot(E_0/1000,Y,'-b','LineWidth',1.5); %unit in kev, fitting
scatter(e_x5,e_y5,a,'*','LineWidth',1.5); %unit in kev
scatter(e_x2/1000,e_y2,a,'+', 'LineWidth',1.5); %unit in kev
scatter(e_x3/1000,e_y3,a,'s', 'LineWidth',1.5); %unit in kev
scatter(e_x4/1000,e_y4,a,'d','LineWidth',1.5); %unit in kev
scatter(e_x1/1000,e_y1,a,'x', 'LineWidth',1.5); %unit in kev
set(gca,'xscale','log')
set(gca,'yscale','log')

xlim([1e-2 1e2])
xlabel('ENERGY (kev)')
ylabel('SPUTTERING YIELD')
L=legend(F,'Sputtering Yield Fitting');
set(gca,'FontSize',13,'LineWidth',1,'FontName','Times New Roman')
h = get(gca, 'xlabel');
set(h, 'FontName','Times New Roman','FontWeight','bold','FontSize', 18)
h = get(gca, 'ylabel');
set(h, 'FontName','Times New Roman','FontWeight','bold','FontSize', 18)

```

```
% set(L,'Interpreter','latex','FontSize',16);
% legend boxoff
box on

figure(2)
plot(E_0/1000,Y,'-.black','LineWidth',1.5); %unit in kev, Zoom in plot
X0=[700,800,900,1000,1100,1200]; %unit in ev
eps0=X0/E_TF;
S0=(0.5.*log(1+1.2288.*(eps0)))./(eps0+0.1728.*sqrt(eps0)+0.008*(eps0).^0.1504);
Y0=Q*S0.*(1-(E_th./(X0)).^(2/3)).*(1-(E_th./X0)).^2;
hold on
scatter(X0/1000,Y0,a,'r','LineWidth',1.5); %unit in kev

xlim([0.6 1.3])
xlabel('ENERGY (kev)')
ylabel('SPUTTERING YIELD')
set(gca,'FontSize',13,'LineWidth',1,'FontName','Times New Roman')
h = get(gca, 'xlabel');
set(h, 'FontName', 'Times New Roman','FontWeight','bold','FontSize', 18)
h = get(gca, 'ylabel');
set(h, 'FontName', 'Times New Roman','FontWeight','bold','FontSize', 18)
% set(L,'Interpreter','latex','FontSize',16);
% legend boxoff
box on
```

Bibliography

- [1] C. J. Brinker, Y. Lu, A. Sellinger, and H. Fan. Evaporation-induced self-assembly: nanostructures made easy. *Advanced Materials*, 11(7):579–585, 1999.
- [2] J. V. Barth, G. Costantini, and K. Kern. Engineering atomic and molecular nanostructures at surfaces. *Nature*, 437(7059):671–679, 2005.
- [3] G. M. Whitesides, J. P. Mathias, and C. T. Seto. Molecular self-assembly and nanochemistry: a chemical strategy for the synthesis of nanostructures. Technical report, DTIC Document, 1991.
- [4] J. Weckesser, A. De Vita, J. V. Barth, C. Cai, and K. Kern. Mesoscopic correlation of supramolecular chirality in one-dimensional hydrogen-bonded assemblies. *Physical Review Letters*, 87(9):096101, 2001.
- [5] J. A. Theobald, N. S. Oxtoby, M. A. Phillips, N. R. Champness, and P. H. Beton. Controlling molecular deposition and layer structure with supramolecular surface assemblies. *Nature*, 424(6952):1029–1031, 2003.
- [6] S. Rusponi, G. Costantini, F. B. de Mongeot, C. Boragno, and U. Valbusa. Patterning a surface on the nanometric scale by ion sputtering. *Applied Physics Letters*, 75(21):3318–3320, 1999.

- [7] S. Facsko, T. Bobek, H. Kurz, T. Dekorsy, S. Kyrsta, and R. Cremer. Ion-induced formation of regular nanostructures on amorphous GaSb surfaces. *Applied Physics Letters*, 80(1):130–132, 2002.
- [8] B. Ziberi, F. Frost, Th. Höche, and B. Rauschenbach. Ripple pattern formation on silicon surfaces by low-energy ion-beam erosion: Experiment and theory. *Physical Review B*, 72(23):235310, 2005.
- [9] M. Kalff, G. Comsa, and T. Michely. Temperature dependent morphological evolution of Pt (111) by ion erosion: destabilization, phase coexistence and coarsening. *Surface science*, 486(1):103–135, 2001.
- [10] C. Wöll, S. Chiang, R. J. Wilson, and P. H. Lippel. Determination of atom positions at stacking-fault dislocations on Au (111) by scanning tunneling microscopy. *Physical Review B*, 39(11):7988, 1989.
- [11] D. L. Abernathy, D. Gibbs, G. Grübel, K. G. Huang, S. G. J. Mochrie, A. R. Sandy, and D. M. Zehner. Reconstruction of the (111) and (001) surfaces of Au and Pt: thermal behavior. *Surface Science*, 283(1-3):260–276, 1993.
- [12] A. Kühnle. Self-assembly of organic molecules at metal surfaces. *Current Opinion in Colloid & Interface Science*, 14(2):157–168, 2009.
- [13] N. J. Tao and S. M. Lindsay. Observations of the 22×3 reconstruction of Au (111) under aqueous solutions using scanning tunneling microscopy. *Journal of Applied Physics*, 70(9):5141–5143, 1991.
- [14] J. V. Barth, R. J. Behm, and G. Ertl. Mesoscopic structural transformations of the Au (111) surface induced by alkali metal adsorption. *Surface Science*, 302(3):L319–L324, 1994.
- [15] J. A. Gardener, G. A. D. Briggs, and M. R. Castell. Scanning tunneling microscopy studies of C_{60} monolayers on Au (111). *Physical Review B*, 80(23):235434, 2009.

- [16] H. Li, B. C. Tee, J. J. Cha, Y. Cui, J. W. Chung, S. Y. Lee, and Z. Bao. High-mobility field-effect transistors from large-area solution-grown aligned C_{60} single crystals. *Journal of the American Chemical Society*, 134(5):2760–2765, 2012.
- [17] Y. He, H. Y. Chen, J. Hou, and Y. Li. Indene- C_{60} bisadduct: a new acceptor for high-performance polymer solar cells. *Journal of the American Chemical Society*, 132(4):1377–1382, 2010.
- [18] B. Bhushan, B. K. Gupta, G. W. Van Cleef, C. Capp, and J. V. Coe. Fullerene (C_{60}) films for solid lubrication. *Tribology transactions*, 36(4):573–580, 1993.
- [19] Y. Yamashita, W. Takashima, and K. Kaneto. Characteristics of heterojunction diode of C_{60} /tetratetrafulvalene (ttf). *Japanese Journal of Applied Physics*, 32(7B):L1017, 1993.
- [20] E. I. Altman and R. J. Colton. Nucleation, growth, and structure of fullerene films on Au (111). *Surface Science*, 279(1-2):49–67, 1992.
- [21] E. I. Altman and R. J. Colton. The interaction of C_{60} with noble metal surfaces. *Surface Science*, 295(1-2):13–33, 1993.
- [22] J. K. Gimzewski, S. Modesti, T. David, and R. R. Schlittler. Scanning tunneling microscopy of ordered C_{60} and C_{70} layers on Au (111), Cu (111), Ag (110), and Au (110) surfaces. *Journal of Vacuum Science & Technology B: Microelectronics and Nanometer Structures Processing, Measurement, and Phenomena*, 12(3):1942–1946, 1994.
- [23] C. Rogero, J. I. Pascual, J. Gomez-Herrero, and A. M. Baro. Resolution of site-specific bonding properties of C_{60} adsorbed on Au (111). *The Journal of Chemical Physics*, 116(2):832–836, 2002.

- [24] Y. C. Xie, L. Tang, and Q. Guo. Cooperative assembly of magic number C_{60} -Au complexes. *Physical Review Letters*, 111(18):186101, 2013.
- [25] J. V. Barth. Molecular architectonic on metal surfaces. *Annual Review of Physical Chemistry*, 58:375–407, 2007.
- [26] F. Schreiber. Structure and growth of self-assembling monolayers. *Progress in Surface Science*, 65(5):151–257, 2000.
- [27] G. E. Poirier and E. D. Pylant. The self-assembly mechanism of alkanethiols on Au (111). *Science*, 272(5265):1145, 1996.
- [28] T. Yokoyama, S. Yokoyama, T. Kamikado, Y. Okuno, and S. Mashiko. Selective assembly on a surface of supramolecular aggregates with controlled size and shape. *Nature*, 413(6856):619–621, 2001.
- [29] T. Yokoyama, T. Kamikado, S. Yokoyama, and S. Mashiko. Conformation selective assembly of carboxyphenyl substituted porphyrins on Au (111). *The Journal of Chemical Physics*, 121(23):11993–11997, 2004.
- [30] S. Clair, S. Pons, A. P. Seitsonen, H. Brune, K. Kern, and J. V. Barth. Stm study of terephthalic acid self-assembly on Au (111): Hydrogen-bonded sheets on an inhomogeneous substrate. *The Journal of Physical Chemistry B*, 108(38):14585–14590, 2004.
- [31] N. Lin, D. Payer, A. Dmitriev, T. Strunskus, C. Wöll, J. V. Barth, and K. Kern. Two-dimensional adatom gas bestowing dynamic heterogeneity on surfaces. *Angewandte Chemie International Edition*, 44(10):1488–1491, 2005.
- [32] D. L. Keeling, N. S. Oxtoby, C. Wilson, M. J. Humphry, N. R. Champness, and P. H. Beton. Assembly and processing of hydrogen bond induced supramolecular nanostructures. *Nano Letters*, 3(1):9–12, 2003.

- [33] A. R. Sandy, S. G. J. Mochrie, D. M. Zehner, K. G. Huang, and D. Gibbs. Structure and phases of the Au (111) surface: X-ray-scattering measurements. *Physical Review B*, 43(6):4667, 1991.
- [34] F. C. Campbell. *Elements of metallurgy and engineering alloys*. ASM International, 2008.
- [35] K. Yagi, K. Takayanagi, K. Kobayashi, N. Osakabe, Y. Tanishiro, and G. Honjo. Surface study by an UHV electron microscope. *Surface Science*, 86:174–181, 1979.
- [36] J. C. Heyraud and J. J. Metois. Anomalous 13 422 diffraction spots from {111} flat gold crystallites:(111) surface reconstruction and moiré fringes between the surface and the bulk. *Surface Science*, 100(3):519–528, 1980.
- [37] J. Perdereau, J. P. Biberian, and G. E. Rhead. Adsorption and surface alloying of lead monolayers on (111) and (110) faces of gold. *Journal of Physics F: Metal Physics*, 4(5):798, 1974.
- [38] K. Takayanagi and K. Yagi. Monatom-high level electron microscopy of metal surfaces. *Transactions of the Japan Institute of Metals*, 24(6):337–348, 1983.
- [39] M. Mansfield and R. J. Needs. Application of the frenkel-kontorova model to surface reconstructions. *Journal of Physics: Condensed Matter*, 2(10):2361, 1990.
- [40] U. Harten, A. M. Lahee, J. P. Toennies, and Ch. Wöll. Observation of a soliton reconstruction of Au (111) by high-resolution helium-atom diffraction. *Physical Review Letters*, 54(24):2619, 1985.
- [41] M. A. Van Hove, R. J. Koestner, P. C. Stair, J. P. Biberian, L. L. Kesmodel, I. Bartoš, and G. A. Somorjai. The surface reconstructions of the (100)

- crystal faces of iridium, platinum and gold: I. experimental observations and possible structural models. *Surface Science*, 103(1):189–217, 1981.
- [42] V. M. Hallmark, S. Chiang, J. F. Rabolt, J. D. Swalen, and R. J. Wilson. Observation of atomic corrugation on Au (111) by scanning tunneling microscopy. *Physical Review Letters*, 59(25):2879, 1987.
- [43] J. V. Barth, H. Brune, G. Ertl, and R. J. Behm. Scanning tunneling microscopy observations on the reconstructed Au (111) surface: Atomic structure, long-range superstructure, rotational domains, and surface defects. *Physical Review B*, 42(15):9307, 1990.
- [44] D. D. Chambliss, R. J. Wilson, and S. Chiang. Nucleation of ordered Ni island arrays on Au (111) by surface-lattice dislocations. *Physical Review Letters*, 66(13):1721, 1991.
- [45] F. Besenbacher, J. V. Lauritsen, T. R. Linderoth, E. Lægsgaard, R. T. Vang, and S. Wendt. Atomic-scale surface science phenomena studied by scanning tunneling microscopy. *Surface Science*, 603(10):1315–1327, 2009.
- [46] R. J. Needs and M. Mansfield. Calculations of the surface stress tensor and surface energy of the (111) surfaces of iridium, platinum and gold. *Journal of Physics: Condensed Matter*, 1(41):7555, 1989.
- [47] H. Bulou and C. Goyhenex. Local strain analysis of the herringbone reconstruction of Au (111) through atomistic simulations. *Physical Review B*, 65(4):045407, 2002.
- [48] W. J. Kaiser and R. C. Jaklevic. Scanning tunneling microscopy study of metals: spectroscopy and topography. *Surface Science*, 181(1):55–68, 1987.
- [49] K. Schouteden, P. Lievens, and C. Van Haesendonck. Fourier-transform scanning tunneling microscopy investigation of the energy versus wave vector

- dispersion of electrons at the Au (111) surface. *Physical Review B*, 79(19):195409, 2009.
- [50] W. Chen, V. Madhavan, T. Jamneala, and M. F. Crommie. Scanning tunneling microscopy observation of an electronic superlattice at the surface of clean gold. *Physical Review Letters*, 80(7):1469, 1998.
- [51] D. Fujita, K. Amemiya, T. Yakabe, H. Nejoh, T. Sato, and M. Iwatsuki. Anisotropic standing-wave formation on an Au (111)-(23 \times 3) reconstructed surface. *Physical Review Letters*, 78(20):3904, 1997.
- [52] Y. Hasegawa and P. Avouris. Direct observation of standing wave formation at surface steps using scanning tunneling spectroscopy. *Physical Review Letters*, 71(7):1071, 1993.
- [53] N. Néel, J. Kröger, and R. Berndt. Fullerene nanowires on a vicinal gold surface. *Applied Physics Letters*, 88(16):163101, 2006.
- [54] V. Repain, J. M. Berroir, S. Rousset, and J. Lecoecur. Interaction between steps and reconstruction on Au (111). *Europhysics Letters*, 47(4):435, 1999.
- [55] S. Rousset, F. Pourmir, J. M. Berroir, J. Klein, J. Lecoecur, P. Hecquet, and B. Salanon. Self-organization on Au (111) vicinal surfaces and the role of surface stress. *Surface Science*, 422(1):33–41, 1999.
- [56] S. Rousset, V. Repain, G. Baudot, Y. Garreau, and J. Lecoecur. Self-ordering of Au (111) vicinal surfaces and application to nanostructure organized growth. *Journal of Physics: Condensed Matter*, 15(47):S3363, 2003.
- [57] Q. Guo, F. Yin, and R. E. Palmer. Beyond the herringbone reconstruction: magic gold fingers. *Small*, 1(1):76–79, 2005.
- [58] F. Yin, R. E. Palmer, and Q. Guo. Faceting of nanoscale fingers on the (111) surface of gold. *Surface Science*, 600(7):1504–1509, 2006.

- [59] R.Q. Hwang and M.C. Bartelt. Scanning tunneling microscopy studies of metal on metal epitaxy. *Chemical Reviews*, 97(4):1063–1082, 1997.
- [60] W. Haiss, D. Lackey, J. K. Sass, and K. H. Besocke. Atomic resolution scanning tunneling microscopy images of Au (111) surfaces in air and polar organic solvents. *The Journal of Chemical Physics*, 95(3), 1991.
- [61] R. Emch, J. Nogami, M. M. Dovek, C. A. Lang, and C. F. Quate. Characterization of gold surfaces for use as substrates in scanning tunneling microscopy studies. *Journal of Applied Physics*, 65(1):79–84, 1989.
- [62] U. Höpfner, H. Hehl, and L. Brehmer. Preparation of ordered thin gold films. *Applied Surface Science*, 152(3):259–265, 1999.
- [63] M. Pedersen, S. Helveg, A. Ruban, I. Stensgaard, E. Lægsgaard, J. K. Nørskov, and F. Besenbacher. How a gold substrate can increase the reactivity of a Pt overlayer. *Surface Science*, 426(3):395–409, 1999.
- [64] Y. Nahas, V. Repain, C. Chacon, Y. Girard, and S. Rousset. Interplay between ordered growth and intermixing of Pt on patterned Au surfaces. *Surface Science*, 604(9):829–833, 2010.
- [65] D. D. Chambliss, R. J. Wilson, and S. Chiang. Ordered nucleation of ni and au islands on Au (111) studied by scanning tunneling microscopy. *Journal of Vacuum Science & Technology B: Microelectronics and Nanometer Structures Processing, Measurement, and Phenomena*, 9(2):933–937, 1991.
- [66] B. Voigtländer, G. Meyer, and N. M. Amer. Epitaxial growth of fe on Au (111): a scanning tunneling microscopy investigation. *Surface Science*, 255(3):L529–L535, 1991.
- [67] M. M. Biener, J. Biener, R. Schalek, and C. M. Friend. Surface alloying of immiscible metals: Mo on Au (111) studied by STM. *Surface Science*, 594(1):221–230, 2005.

- [68] Z. Song, T. Cai, J. A. Rodriguez, J. Hrbek, Ally S. Y. C., and C. M. Friend. A novel growth mode of Mo on Au (111) from a Mo (CO)₆ precursor: An STM study. *The Journal of Physical Chemistry B*, 107(4):1036–1043, 2003.
- [69] J. A. Meyer, I. D. Baikie, E. Kopatzki, and R. J. Behm. Preferential island nucleation at the elbows of the Au (111) herringbone reconstruction through place exchange. *Surface Science*, 365(1):L647–L651, 1996.
- [70] W. G. Cullen and P. N. First. Island shapes and intermixing for submonolayer nickel on Au (111). *Surface Science*, 420(1):53–64, 1999.
- [71] I. Chado, C. Goyhenex, H. Bulou, and J. P. Bucher. Cluster critical size effect during growth on a heterogeneous surface. *Physical Review B*, 69(8):085413, 2004.
- [72] M. M. Dovek, C. A. Lang, J. Nogami, and C. F. Quate. Epitaxial growth of Ag on Au (111) studied by scanning tunneling microscopy. *Physical Review B*, 40(17):11973, 1989.
- [73] B. Fischer, H. Brune, J. V. Barth, A. Fricke, and K. Kern. Nucleation kinetics on inhomogeneous substrates: Al/Au (111). *Physical Review Letters*, 82(8):1732, 1999.
- [74] B. Fischer, J. V. Barth, A. Fricke, L. Nedelmann, and K. Kern. Growth and surface alloying of Al on Au (111) at room temperature. *Surface Science*, 389(1):366–374, 1997.
- [75] C. A. Lang, M. M. Dovek, J. Nogami, and C. F. Quate. Au (111) autoepitaxy studied by scanning tunneling microscopy. *Surface Science*, 224(1-3):L947–L955, 1989.
- [76] M. S. Dresselhaus, G. Dresselhaus, and P. C. Eklund. *Science of fullerenes and carbon nanotubes: their properties and applications*. Academic Press, 1996.

- [77] H. W. Kroto, J. R. Heath, S. C. O'Brien, R. F. Curl, and R. E. Smalley. C₆₀: Buckminsterfullerene. *Nature*, 318:162, 1985.
- [78] R. E. Smalley. Discovering the fullerenes. *Reviews of Modern Physics*, 69(3):723, 1997.
- [79] W. Kratschmer, L. D. Lamb, K. Fostiropoulos, and D. R. Huffman. Solid C₆₀: a new form of carbon. *Nature*, 347:27, 1990.
- [80] C. S. Yannoni, P. P. Bernier, D. S. Bethune, G. Meijer, and J. R. Salem. NMR determination of the bond lengths in C₆₀. *Journal of the American Chemical Society*, 113(8):3190–3192, 1991.
- [81] C. S. Yannoni, R. D. Johnson, G. Meijer, D. S. Bethune, and J. R. Salem. Carbon-13 NMR study of the C₆₀ cluster in the solid state: molecular motion and carbon chemical shift anisotropy. *The Journal of Physical Chemistry*, 95(1):9–10, 1991.
- [82] K. Hedberg, L. Hedberg, D. S. Bethune, C. A. Brown, H. C. Dorn, R. D. Johnson, and M. D. Vries. Bond lengths in free molecules of buckminsterfullerene, C₆₀, from gas-phase electron diffraction. *Science*, 254(5030):410, 1991.
- [83] K. Prassides, H. W. Kroto, R. Taylor, D. R. M. Walton, W. I. F. David, J. Tomkinson, R. C. Haddon, M. J. Rosseinsky, and D. W. Murphy. Fullerenes and fullerides in the solid state: neutron scattering studies. *Carbon*, 30(8):1277–1286, 1992.
- [84] W. I. F. David, R. M. Ibberson, T. J. S. Dennis, J. P. Hare, and K. Prassides. Structural phase transitions in the fullerene C₆₀. *Europhysics Letters*, 18(3):219, 1992.

- [85] T. R. Ohno, Y. Chen, S. E. Harvey, G. H. Kroll, J. H. Weaver, R. E. Haufler, and R. E. Smalley. C_{60} bonding and energy-level alignment on metal and semiconductor surfaces. *Physical Review B*, 44(24):13747, 1991.
- [86] F. J. Himpsel and T. Fauster. Probing valence states with photoemission and inverse photoemission. *Journal of Vacuum Science & Technology A*, 2(2):815–821, 1984.
- [87] L. S. Wang, J. Conceicao, C. Jin, and R. E. Smalley. Threshold photodetachment of cold C_{60} . *Chemical physics letters*, 182(1):5–11, 1991.
- [88] D. R. McKenzie, C. A. Davis, D. J. H. Cockayne, D. A. Muller, and A. M. Vassallo. The structure of the C_{70} molecule. *Nature*, 355(6361):622–624, 1992.
- [89] J. Baker, P. W. Fowler, P. Lazzeretti, M. Malagoli, and R. Zanasi. Structure and properties of C_{70} . *Chemical physics letters*, 184(1-3):182–186, 1991.
- [90] J. H. Weaver. Electronic structures of C_{60} , C_{70} and the fullerenes: Photoemission and inverse photoemission studies. *Journal of Physics and Chemistry of Solids*, 53(11):1433–1447, 1992.
- [91] C. Christides, T. John, S. Dennis, K. Prassides, R. L. Cappelletti, D. A. Neumann, and J. R. D. Copley. Rotational dynamics of solid C_{70} : A neutron-scattering study. *Physical Review B*, 49(4):2897, 1994.
- [92] K. Thirunavukkuarasu, V. C. Long, J. L. Musfeldt, F. Borondics, G. Klupp, K. Kamarás, and C. A. Kuntscher. Rotational dynamics in C_{70} : temperature-and pressure-dependent infrared studies. *The Journal of Physical Chemistry C*, 115(9):3646–3653, 2011.

- [93] M. A. Verheijen, H. Meekes, G. Meijer, P. Bennema, J. L. De Boer, S. Van Smaalen, G. Van Tendeloo, S. Amelinckx, S. Muto, and J. Van Landuyt. The structure of different phases of pure C_{70} crystals. *Chemical Physics*, 166(1-2):287–297, 1992.
- [94] M. P. Marder. *Condensed matter physics*. John Wiley & Sons, 2010.
- [95] F. OuYang, H. Xu, and T. Fan. All-carbon nanoswitch based on C_{70} molecule: A first principles study. *Journal of Applied Physics*, 102(6):4501, 2007.
- [96] S. K. Lim, M. E. Burba, and A. C. Albrecht. The stokes law radius of the C_{60} radical anion in n-hexane by time-of-flight mobility measurements. *Chemical Physics Letters*, 216(3-6):405–408, 1993.
- [97] R. J. Wilson, G. Meijer, D. S. Bethune, R. D. Johnson, D. D. Chambliss, M. S. De Vries, H. E. Hunziker, and H. R. Wendt. Imaging C_{60} clusters on a surface using a scanning tunnelling microscope. *Nature*, 348(6302):621–622, 1990.
- [98] C. T. Tzeng, W. S. Lo, J. Y. Yuh, R. Y. Chu, and K. D. Tsuei. Photoemission, near-edge X-ray-absorption spectroscopy, and low-energy electron-diffraction study of C_{60} on Au (111) surfaces. *Physical Review B*, 61(3):2263, 2000.
- [99] A. J. Britton, A. Rienzo, J. N. O’Shea, and K. Schulte. Charge transfer between the Au (111) surface and adsorbed C–60: Resonant photoemission and new core-hole decay channels. *The Journal of Chemical Physics*, 133(9):094705–094705, 2010.
- [100] A Fartash. In-plane orientational order across C_{60} (111)/Au (111) interfaces. *Thin solid films*, 323(1):296–303, 1998.

- [101] G. Schull and R. Berndt. Orientationally ordered (7×7) superstructure of C_{60} on Au (111). *Physical Review Letters*, 99(22):226105, 2007.
- [102] H. Shin, A. Schwarze, R. D. Diehl, K. Pussi, A. Colombier, É. Gaudry, J. Ledieu, G. M. McGuirk, L. N. S. Loli, V. Fournée, L. L. Wang, and R. Berndt. Structure and dynamics of C_{60} molecules on Au (111). *Physical Review B*, 89(24):245428, 2014.
- [103] L. Tang, Y. Xie, and Q. Guo. Complex orientational ordering of C_{60} molecules on Au (111). *The Journal of Chemical Physics*, 135(11):114702, 2011.
- [104] X. Q. Shi, M. A. Van Hove, and R. Q. Zhang. Adsorbate-induced reconstruction by C_{60} on close-packed metal surfaces: Mechanism for different types of reconstruction. *Physical Review B*, 85(7):075421, 2012.
- [105] J. K. Gimzewski, S. Modesti, C. Gerber, and R. R. Schlittler. Observation of a new Au (111) reconstruction at the interface of an adsorbed C_{60} overlayer. *Chemical Physics Letters*, 213(3):401–406, 1993.
- [106] T. Hashizume, K. Motai, X. D. Wang, H. Shinohara, Y. Saito, Y. Maruyama, K. Ohno, Y. Kawazoe, Y. Nishina, H. W. Pickering, Y. Kuk, and T. Sakurai. Intramolecular structures of C_{60} molecules adsorbed on the Cu (111)-(1×1) surface. *Physical Review Letters*, 71(18):2959, 1993.
- [107] K. Motai, T. Hashizume, H. Shinohara, Y. Saito, H. W. Pickering, Y. Nishina, and T. Sakurai. C_{60} grown on the Cu (111) 11 surface. *Japanese Journal of Applied Physics*, 32(3B):L450, 1993.
- [108] T. Sakurai, X. D. Wang, T. Hashizume, V. Yurov, H. Shinohara, and H. W. Pickering. Adsorption of fullerenes on Cu (111) and Ag (111) surfaces. *Applied Surface Science*, 87:405–413, 1995.

- [109] Y. Maruyama, K. Ohno, and Y. Kawazoe. Electronic structures of C_{60} and C_{70} adsorbed on the cu (111) surface and intramolecular stm images. *Physical Review B*, 52(3):2070, 1995.
- [110] J. A. Larsson, S. D. Elliott, J. C. Greer, J. Repp, G. Meyer, and R. Al-lenspach. Orientation of individual C_{60} molecules adsorbed on Cu (111): low-temperature scanning tunneling microscopy and density functional calculations. *Physical Review B*, 77(11):115434, 2008.
- [111] E. I. Altman and R. J. Colton. Determination of the orientation of C_{60} adsorbed on Au (111) and Ag (111). *Physical Review B*, 48(24):18244, 1993.
- [112] T. Sakurai, X. D. Wang, Q. K. Xue, Y. Hasegawa, T. Hashizume, and H. Shinohara. Scanning tunneling microscopy study of fullerenes. *Progress in Surface Science*, 51(4):263–408, 1996.
- [113] A. Tamai, A. P. Seitsonen, R. Fasel, Z. X. Shen, J. Osterwalder, and T. Gre-ber. Doping-induced reorientation of C_{60} molecules on Ag (111). *Physical Review B*, 72(8):085421, 2005.
- [114] H. I. Li, K. Pussi, K. J. Hanna, L. L. Wang, D. D. Johnson, H. P. Cheng, H. Shin, S. Curtarolo, W. Moritz, J. A. Smerdon, et al. Surface geometry of C_{60} on Ag (111). *Physical Review Letters*, 103(5):056101, 2009.
- [115] T. Chen, S. Howells, M. Gallagher, D. Sarid, L. D. Lamb, D. R. Huffman, and R. K. Workman. Scanning-tunneling-microscopy and spectroscopy studies of C_{70} thin films on gold substrates. *Physical Review B*, 45(24):14411, 1992.
- [116] F. Rossel, M. Pivetta, F. Patthey, E. Čavar, A. P. Seitsonen, and W. D. Schneider. Growth and characterization of fullerene nanocrystals on Na-Cl/Au (111). *Physical Review B*, 84(7):075426, 2011.

- [117] N. Katsonis, A. Marchenko, and D. Fichou. Adsorption and self-assembly of C_{70} molecules at the Au (111)/n-tetradecane interface: A scanning tunneling microscopy study. *Advanced Materials*, 16(4):309–312, 2004.
- [118] P. Wang, H. J. Zhang, Y. J. Li, C. Q. Sheng, Y. Shen, H. Y. Li, S. N. Bao, and H. N. Li. Effect of charge transfer on the geometric structure of a C_{70} monolayer on the surface of Ag (111). *Physical Review B*, 85(20):205445, 2012.
- [119] P. Wang, L. Meng, X. B. Wang, Y. J. Li, C. Q. Sheng, J. O. Wang, H. J. Qian, K. Ibrahim, and H. N. Li. Electronic states of a C_{70} monolayer on the surface of Ag (111). *Journal of Physics: Condensed Matter*, 23(39):395002, 2011.
- [120] L. L. Wang and H. P. Cheng. Density functional study of the adsorption of a C_{60} monolayer on Ag (111) and Au (111) surfaces. *Physical Review B*, 69(16):165417, 2004.
- [121] X. D. Wang, V. Y. Yurov, T. Hashizume, H. Shinohara, and T. Sakurai. Imaging of C_{70} intramolecular structures with scanning tunneling microscopy. *Physical Review B*, 49(20):14746, 1994.
- [122] A. Goldoni, C. Cepek, R. Larciprete, L. Sangaletti, S. Pagliara, L. Floreano, R. Gotter, A. Verdini, A. Morgante, Y. Luo, and M. Nyberg. C_{70} adsorbed on Cu (111): metallic character and molecular orientation. *The Journal of Chemical Physics*, 116(17):7685–7690, 2002.
- [123] T. J. S. Dennis, K. Prassides, E. Roduner, L. Cristofolini, and R. DeRenzi. Rotational dynamics of solid fullerene C_{70} monitored by positive muon spin labels. *The Journal of Physical Chemistry*, 97(33):8553–8556, 1993.

- [124] B. G. M. Vaughan, P. A. Heiney, J. E. Fischer, D. E. Luzzi, D. A. Ricketts-Foot, A. R. McGhie, and Y. W. Hui. Orientational disorder in solvent-free solid C_{70} . *Science*, 254:1350, 1991.
- [125] A. Cheng and M. L. Klein. Solid C_{70} : A molecular-dynamics study of the structure and orientational ordering. *Physical Review B*, 46(8):4958, 1992.
- [126] Y. C. Xie, M. Rokni Fard, D. Kaya, D. Bao, R. E. Palmer, S. Du, and Q. Guo. Site-specific assembly of fullerene nanorings guided by two-dimensional au clusters. *The Journal of Physical Chemistry C*, 120(20):10975–10981, 2016.
- [127] X. Torrelles, M. Pedio, C. Cepek, and R. Felici. $(2\sqrt{3} \times 2\sqrt{3})$ R 30 induced self-assembly ordering by C_{60} on a Au (111) surface: X-ray diffraction structure analysis. *Physical Review B*, 86(7):075461, 2012.
- [128] Y. Xie. *An STM study of C_{60} molecule on Au (111): close-packed single layer and magic number clusters*. PhD thesis, University of Birmingham, 2014.
- [129] R. Behrisch and W. Eckstein. *Sputtering by particle bombardment: experiments and computer calculations from threshold to MeV energies*, volume 110. Springer Science & Business Media, 2007.
- [130] J. S. Williams. Materials modification with ion beams. *Reports on Progress in Physics*, 49(5):491, 1986.
- [131] P. Williams. The sputtering process and sputtered ion emission. *Surface Science*, 90(2):588–634, 1979.
- [132] Y. Yamamura and H. Tawara. Energy dependence of ion-induced sputtering yields from monatomic solids at normal incidence. *Atomic Data and Nuclear Data Tables*, 62(2):149–253, 1996.
- [133] T. Michely, K. H. Besocke, and G. Comsa. Observation of sputtering damage on Au (111). *Surface Science*, 230(1-3):L135–L139, 1990.

- [134] B. Poelsema, K. Lenz, L. S. Brown, L. K. Verheij, and G. Comsa. Lateral distribution of ion bombardment induced defects on Pt (111) at 80 k. *Surface Science*, 162(1):1011–1016, 1985.
- [135] M. Ritter, M. Stindtman, M. Farle, and K. Baberschke. Nanostructuring of the Cu (001) surface by ion bombardment: a STM study. *Surface Science*, 348(3):243–252, 1996.
- [136] T. Michely, M. Kalff, G. Comsa, M. Strobel, and K. H. Heinig. Coarsening mechanisms in surface morphological evolution. *Journal of Physics: Condensed Matter*, 14(16):4177, 2002.
- [137] S. Rusponi, G. Costantini, C. Boragno, and U. Valbusa. Ripple wave vector rotation in anisotropic crystal sputtering. *Physical Review Letters*, 81(13):2735, 1998.
- [138] A. C. Bose and M. Yoshitake. Pattern formation induced by Ar⁺ sputtering on Au (111). *Applied surface science*, 241(1):174–178, 2005.
- [139] R. Behrisch and W. Eckstein. *Sputtering by particle bombardment: experiments and computer calculations from threshold to MeV energies*, volume 110. Springer Science & Business Media, 2007.
- [140] A. Oliva-Florio, R. A. Baragiola, M. M. Jakas, E. V. Alonso, and J. Ferrón. Noble-gas ion sputtering yield of gold and copper: Dependence on the energy and angle of incidence of the projectiles. *Physical Review B*, 35(5):2198, 1987.
- [141] J. Bohdansky. A universal relation for the sputtering yield of monatomic solids at normal ion incidence. *Nuclear Instruments and Methods in Physics Research Section B: Beam Interactions with Materials and Atoms*, 2(1-3):587–591, 1984.
- [142] C. Garcia-Rosales, W. Eckstein, and J. Roth. Revised formulae for sputtering data. *Journal of Nuclear Materials*, 218(1):8–17, 1995.

- [143] J. Bohdansky, J. Roth, and H. L. Bay. An analytical formula and important parameters for low-energy ion sputtering. *Journal of Applied Physics*, 51(5): 2861–2865, 1980.
- [144] J. A. Stroscio and W. J. Kaiser. *Scanning tunneling microscopy*, volume 27. Academic Press, 1993.
- [145] C. J. Chen. *Introduction to scanning tunneling microscopy*, volume 4. Oxford University Press on Demand, 1993.
- [146] C. Bai. *Scanning tunneling microscopy and its application*, volume 32. Springer Science & Business Media, 2000.
- [147] M. Marshall and M. R. Castell. Scanning tunnelling microscopy of epitaxial nanostructures. *Chemical Society Reviews*, 43(7):2226–2239, 2014.
- [148] Y. Kuk and P. J. Silverman. Role of tip structure in scanning tunneling microscopy. *Applied physics letters*, 48(23):1597–1599, 1986.
- [149] C. J. Chen. Origin of atomic resolution on metal surfaces in scanning tunneling microscopy. *Physical Review Letters*, 65(4):448, 1990.
- [150] D. P. Woodruff and T. A. Delchar. *Modern techniques of surface science*. Cambridge University Press, 1994.
- [151] K. Oura, V. G. Lifshits, A. Saranin, A. V. Zotov, and M. Katayama. *Surface science: an introduction*. Springer Science & Business Media, 2013.
- [152] Z. Yu, C. M. Wang, Y. Du, S. Thevuthasan, and I. Lyubinetsky. Reproducible tip fabrication and cleaning for UHV STM. *Ultramicroscopy*, 108(9):873–877, 2008.
- [153] I. Ekvall, E. Wahlström, D. Claesson, H. Olin, and E. Olsson. Preparation and characterization of electrochemically etched W tips for STM. *Measurement Science and Technology*, 10(1):11, 1999.

- [154] D. Cherns. The surface structure of (111) gold films sputtered in the high voltage electron microscope a theoretical model. *Philosophical Magazine*, 36(6):1429–1444, 1977.
- [155] G. Reiss, J. Vancea, H. Wittmann, J. Zweck, and H. Hoffmann. Scanning tunneling microscopy on rough surfaces: Tip-shape-limited resolution. *Journal of Applied Physics*, 67(3):1156–1159, 1990.
- [156] D. Keller. Reconstruction of STM and AFM images distorted by finite-size tips. *Surface Science*, 253(1-3):353–364, 1991.
- [157] T. Lin, Q. Wu, J. Liu, Z. Shi, P. N. Liu, and N. Lin. Thermodynamic versus kinetic control in self-assembly of zero-, one-, quasi-two-, and two-dimensional metal-organic coordination structures. *The Journal of chemical physics*, 142(10):101909, 2015.
- [158] S. Scheuring and J. N. Sturgis. Chromatic adaptation of photosynthetic membranes. *Science*, 309(5733):484–487, 2005.
- [159] C. Voz, J. Puigdollers, S. Cheylan, M. Fonrodona, M. Stella, J. Andreu, and R. Alcubilla. Photodiodes based on fullerene semiconductor. *Thin Solid Films*, 515(19):7675–7678, 2007.
- [160] M. Böhrringer, K. Morgenstern, W. Schneider, R. Berndt, F. Mauri, A. De Vita, and R. Car. Two-dimensional self-assembly of supramolecular clusters and chains. *Physical Review Letters*, 83(2):324, 1999.
- [161] L. Tang, X. Zhang, Q. Guo, Y. N Wu, L. L. Wang, and H. P. Cheng. Two bonding configurations for individually adsorbed C₆₀ molecules on Au (111). *Physical Review B*, 82(12):125414, 2010.
- [162] S. Neretina, R. A. Hughes, K. D. Gilroy, and M. Hajfathalian. Noble metal nanostructure synthesis at the liquid–substrate interface: New structures,

- new insights, and new possibilities. *Accounts of Chemical Research*, 49(10):2243–2250, 2016.
- [163] D. Fink, P. Szimkoviak, J. Kastner, L. Palmetshofer, L. T. Chadderton, L. Wang, and H. Kuzmany. Ion beam radiation damage of thin fullerene films. *Nuclear Instruments and Methods in Physics Research Section B: Beam Interactions with Materials and Atoms*, 108(1-2):114–124, 1996.
- [164] Y. Zhu, T. Yi, B. Zheng, and L. Cao. The interaction of C₆₀ fullerene and carbon nanotube with Ar ion beam. *Applied Surface Science*, 137(1):83–90, 1999.
- [165] T. J. Colla, R. Aderjan, R. Kissel, and H. M. Urbassek. Sputtering of Au (111) induced by 16-keV Au cluster bombardment: Spikes, craters, late emission, and fluctuations. *Physical Review B*, 62(12):8487, 2000.
- [166] H. Coufal, H. F. Winters, H. L. Bay, and W. Eckstein. Energy transfer from noble-gas ions to surfaces: Collisions with carbon, silicon, copper, silver, and gold in the range 100–4000 eV. *Physical Review B*, 44(10):4747, 1991.
- [167] C. A. Lang, C. F. Quate, and J. Nogami. Initial stages of sputtering on Au (111) as seen by scanning tunneling microscopy. *Applied physics letters*, 59(14):1696–1698, 1991.
- [168] M. T. Robinson. Binding energy effects in cascade evolution and sputtering. *Nuclear Instruments and Methods in Physics Research Section B: Beam Interactions with Materials and Atoms*, 115(1):549–553, 1996.
- [169] C. Yan and Q. Y. Zhang. Study on low-energy sputtering near the threshold energy by molecular dynamics simulations. *AIP Advances*, 2(3):032107, 2012.
- [170] *Useful Information and Facts about the Practice of Sputtering*. Specs Manual, 2017.

- [171] M. T. Robinson and A. L. Southern. Sputtering experiments with 1-to 5-keV Ar⁺ ions. ii. monocrystalline targets of Al, Cu, and Au. *Journal of Applied Physics*, 38(7):2969–2973, 1967.
- [172] T. M. Nenadović, Z. B. Fotirić, and T. S. Dimitrijević. Sputtering of gold bombarded by 20–50 keV A⁺ and Xe⁺ ions. *Surface Science*, 33(3):607–616, 1972.
- [173] A. Reinköster, B. Siegmann, U. Werner, B. A. Huber, and H. O. Lutz. Multi-fragmentation of C₆₀ after collisions with Ar⁺ ions. *Journal of Physics B: Atomic, Molecular and Optical Physics*, 35(24):4989, 2002.
- [174] S. Ghosh, D. K. Avasthi, A. Tripathi, S. K. Srivastava, S. N. Rao, T. Som, V. K. Mittal, F. Grüner, and W. Assmann. Studies of electronic sputtering of fullerene under swift heavy ion impact. *Nuclear Instruments and Methods in Physics Research Section B: Beam Interactions with Materials and Atoms*, 190(1):169–172, 2002.
- [175] M. Matsumoto, J. Inukai, E. Tsutsumi, S. Yoshimoto, K. Itaya, O. Ito, K. Fujiwara, M. Murata, Y. Murata, and K. Komatsu. Adlayers of C₆₀-C₆₀ and C₆₀-C₇₀ fullerene dimers formed on Au (111) in benzene solutions studied by STM and LEED. *Langmuir*, 20(4):1245–1250, 2004.
- [176] S. Nie, N. C. Bartelt, J. M. Wofford, O. D. Dubon, K. F. McCarty, and K. Thürmer. Scanning tunneling microscopy study of graphene on Au (111): Growth mechanisms and substrate interactions. *Physical Review B*, 85(20):205406, 2012.